



**TECHNISCHE  
UNIVERSITÄT  
DRESDEN**

---

Fakultät Umweltwissenschaften

---

## **Thema der Dissertation**

Road Condition Mapping by Integration of Laser Scanning,  
RGB Imaging and Spectrometry

Dissertation zur Erlangung des akademischen Grades  
Doktoringenieur (Dr.-Ing)

vorgelegt von

*Miraliakbari, Alvand M.Sc.*

geboren am 04.05.1980  
in Teheran

Gutachter:

Herr Prof. Dr. sc. techn. habil. Hans-Gerd Maas  
Technische Universität Dresden

Herr Prof. Dr.-Ing. Michael Hahn  
Hochschule für Technik Stuttgart

Herr Prof. Dr.-Ing. habil. Norbert Haala  
Universität Stuttgart

Verteidigung: Dresden, 16.08.2017

## **Erklärung des Promovenden**

Die Übereinstimmung dieses Exemplars mit dem Original der Dissertation zum Thema:

**“Road Condition Mapping by Integration of Laser Scanning, RGB Imaging and Spectrometry”**

wird hiermit bestätigt.

Dresden, 01.10.2017

Alvand Miraliakbari

## Abstract

Roads are important infrastructure and are primary means of transportation. Control and maintenance of roads are substantial as the pavement surface deforms and deteriorates due to heavy load and influences of weather. Acquiring detailed information about the pavement condition is a prerequisite for proper planning of road pavement maintenance and rehabilitation. Many companies detect and localize the road pavement distresses manually, either by on-site inspection or by digitizing laser data and imagery captured by mobile mapping. The automation of road condition mapping using laser data and colour images is a challenge. Beyond that, the mapping of material properties of the road pavement surface with spectrometers has not yet been investigated.

This study aims at automatic mapping of road surface condition including distress and material properties by integrating laser scanning, RGB imaging and spectrometry. All recorded data are georeferenced by means of GNSS/ INS. Methods are developed for pavement distress detection that cope with a variety of different weather and asphalt conditions. Further objective is to analyse and map the material properties of the pavement surface using spectrometry data.

No standard test data sets are available for benchmarking developments on road condition mapping. Therefore, all data have been recorded with a mobile mapping van which is set up for the purpose of this research. The concept for detecting and localizing the four main pavement distresses, i.e. ruts, potholes, cracks and patches is the following: ruts and potholes are detected using laser scanning data, cracks and patches using RGB images. For each of these pavement distresses, two or more methods are developed, implemented, compared to each other and evaluated to identify the most successful method. With respect to the material characteristics, spectrometer data of road sections are classified to indicate pavement quality. As a spectrometer registers almost a reflectivity curve in VIS, NIR and SWIR wavelength, indication of aging can be derived. After detection and localization of the pavement distresses and pavement quality classes, the road condition map is generated by overlaying all distresses and quality classes.

As a preparatory step for rut and pothole detection, the road surface is extracted from mobile laser scanning data based on a height jump criterion. For the investigation on rut detection, all scanlines are processed. With an approach based on iterative 1D polynomial fitting, ruts are successfully detected. For streets with the width of 6 m to 10 m, a 6<sup>th</sup> order polynomial is found to be most suitable. By 1D cross-correlation, the centre of the rut is localized. An alternative method using local curvature shows a high sensitivity to the shape and width of a rut and is less successful. For pothole detection, the approach based on polynomial fitting generalized to two dimensions. As an alternative, a procedure using geodesic morphological reconstruction is investigated. Bivariate polynomial fitting encounters problems with overshoot at the boundary of the regions. The detection is very successful using

geodesic morphology. For the detection of pavement cracks, three methods using rotation invariant kernels are investigated. Line Filter, High-pass Filter and Modified Local Binary Pattern kernels are implemented. A conceptual aspect of the procedure is to achieve a high degree of completeness. The most successful variant is the Line Filter for which the highest degree of completeness of 81.2 % is achieved. Two texture measures, the gradient magnitude and the local standard deviation are employed to detect pavement patches. As patches may differ with respect to homogeneity and may not always have a dark border with the intact pavement surface, the method using the local standard deviation is more suitable for detecting the patches. Linear discriminant analysis is utilized for asphalt pavement quality analysis and classification. Road pavement sections of ca. 4 m length are classified into two classes, namely: “Good” and “Bad” with the overall accuracy of 77.6 %.

The experimental investigations show that the developed methods for automatic distress detection are very successful. By 1D polynomial fitting on laser scanlines, ruts are detected. In addition to ruts also pavement depressions like shoving can be revealed. The extraction of potholes is less demanding. As potholes appear relatively rare in the road networks of a city, the road segments which are affected by potholes are selected interactively. While crack detection by Line Filter works very well, the patch detection is more challenging as patches sometimes look very similar to the intact surface. The spectral classification of pavement sections contributes to road condition mapping as it gives hints on aging of the road pavement.



## Kurzfassung

Straßen bilden die primären Transportwege für Personen und Güter und sind damit ein wichtiger Bestandteil der Infrastruktur. Der Aufwand für Instandhaltung und Wartung der Straßen ist erheblich, da sich die Fahrbahnoberfläche verformt und durch starke Belastung und Wettereinflüsse verschlechtert. Die Erfassung detaillierter Informationen über den Fahrbahnzustand ist Voraussetzung für eine sachgemäße Planung der Fahrbahnsanierung und -rehabilitation. Viele Unternehmen detektieren und lokalisieren die Fahrbahnschäden manuell entweder durch Vor-Ort-Inspektion oder durch Digitalisierung von Laserdaten und Bildern aus mobiler Datenerfassung. Eine Automatisierung der Straßenkartierung mit Laserdaten und Farbbildern steht noch in den Anfängen. Zudem werden bisher noch nicht die Alterungszustände der Asphaltdecke mit Hilfe der Spektrometrie bewertet.

Diese Studie zielt auf den automatischen Prozess der Straßenzustandskartierung einschließlich der Straßenschäden und der Materialeigenschaften durch Integration von Laserscanning, RGB-Bilderfassung und Spektrometrie ab. Alle aufgezeichneten Daten werden mit GNSS / INS georeferenziert. Es werden Methoden für die Erkennung von Straßenschäden entwickelt, die sich an unterschiedliche Datenquellen bei unterschiedlichem Wetter- und Asphaltzustand anpassen können. Ein weiteres Ziel ist es, die Materialeigenschaften der Fahrbahnoberfläche mittels Spektrometrie-Daten zu analysieren und abzubilden.

Derzeit gibt es keine standardisierten Testdatensätze für die Evaluierung von Verfahren zur Straßenzustandsbeschreibung. Deswegen wurden alle Daten, die in dieser Studie Verwendung finden, mit einem eigens für diesen Forschungszweck konfigurierten Messfahrzeug aufgezeichnet. Das Konzept für die Detektion und Lokalisierung der wichtigsten vier Arten von Straßenschäden, nämlich Spurrillen, Schlaglöcher, Risse und Flickstellen ist das folgende: Spurrillen und Schlaglöcher werden aus Laserdaten extrahiert, Risse und Flickstellen aus RGB- Bildern. Für jede dieser Straßenschäden werden mindestens zwei Methoden entwickelt, implementiert, miteinander verglichen und evaluiert um festzustellen, welche Methode die erfolgreichste ist. Im Hinblick auf die Materialeigenschaften werden Spektrometriedaten der Straßenabschnitte klassifiziert, um die Qualität des Straßenbelages zu bewerten. Da ein Spektrometer nahezu eine kontinuierliche Reflektivitätskurve im VIS-, NIR- und SWIR-Wellenlängenbereich aufzeichnet, können Merkmale der Asphaltalterung abgeleitet werden. Nach der Detektion und Lokalisierung der Straßenschäden und der Qualitätsklasse des Straßenbelages wird der übergreifende Straßenzustand mit Hilfe von Durchschlagsregeln als Kombination aller Zustandswerte und Qualitätsklassen ermittelt.

In einem vorbereitenden Schritt für die Spurrillen- und Schlaglocherkennung wird die Straßenoberfläche aus mobilen Laserscanning-Daten basierend auf einem Höhengrundsprung-Kriterium extrahiert. Für die Untersuchung zur Spurrillen-Erkennung werden alle Scanlinien verarbeitet. Mit

einem Ansatz, der auf iterativer 1D-Polynomannpassung basiert, werden Spurrillen erfolgreich erkannt. Für eine Straßenbreite von 8-10m erweist sich ein Polynom sechsten Grades als am besten geeignet. Durch 1D-Kreuzkorrelation wird die Mitte der Spurrille erkannt. Eine alternative Methode, die die lokale Krümmung des Querprofils benutzt, erweist sich als empfindlich gegenüber Form und Breite einer Spurrille und ist weniger erfolgreich. Zur Schlaglocherkennung wird der Ansatz, der auf Polynomannpassung basiert, auf zwei Dimensionen verallgemeinert. Als Alternative wird eine Methode untersucht, die auf der Geodätischen Morphologischen Rekonstruktion beruht. Bivariate Polynomannpassung führt zu Überschwingen an den Rändern der Regionen. Die Detektion mit Hilfe der Geodätischen Morphologischen Rekonstruktion ist dagegen sehr erfolgreich. Zur Risserkennung werden drei Methoden untersucht, die rotationsinvariante Kerne verwenden. Linienfilter, Hochpassfilter und Lokale Binäre Muster werden implementiert. Ein Ziel des Konzeptes zur Risserkennung ist es, eine hohe Vollständigkeit zu erreichen. Die erfolgreichste Variante ist das Linienfilter, für das mit 81,2 % der höchste Grad an Vollständigkeit erzielt werden konnte. Zwei Texturmaße, nämlich der Betrag des Grauwert-Gradienten und die lokale Standardabweichung werden verwendet, um Flickstellen zu entdecken. Da Flickstellen hinsichtlich der Homogenität variieren können und nicht immer eine dunkle Grenze mit dem intakten Straßenbelag aufweisen, ist diejenige Methode, welche die lokale Standardabweichung benutzt, besser zur Erkennung von Flickstellen geeignet. Lineare Diskriminanzanalyse wird zur Analyse der Asphaltqualität und zur Klassifikation benutzt. Straßenabschnitte von ca. 4m Länge werden zwei Klassen („Gut“ und „Schlecht“) mit einer gesamten Accuracy von 77,6 % zugeordnet.

Die experimentellen Untersuchungen zeigen, dass die entwickelten Methoden für die automatische Entdeckung von Straßenschäden sehr erfolgreich sind. Durch 1D Polynomannpassung an Laser-Scanlinien werden Spurrillen entdeckt. Zusätzlich zu Spurrillen werden auch Unebenheiten des Straßenbelages wie Aufschiebungen detektiert. Die Extraktion von Schlaglöchern ist weniger anspruchsvoll. Da Schlaglöcher relativ selten in den Straßennetzen von Städten auftreten, werden die Straßenabschnitte mit Schlaglöchern interaktiv ausgewählt. Während die Rissdetektion mit Linienfiltern sehr gut funktioniert, ist die Erkennung von Flickstellen eine größere Herausforderung, da Flickstellen manchmal der intakten Straßenoberfläche sehr ähnlich sehen. Die spektrale Klassifizierung der Straßenabschnitte trägt zur Straßenzustandsbewertung bei, indem sie Hinweise auf den Alterungszustand des Straßenbelages liefert.



## **Acknowledgment**

I would like to express my sincere gratitude to my supervisor Prof. Dr.-Ing. habil. Hans-Gerd Maas, for giving me the opportunity to write my dissertation. His endless encouragement, excellent guidance and scientific advice during my dissertation are highly appreciated.

I would like to thank Prof. Dr.-Ing. Michael Hahn, my next supervisor and the leader of the project RoadInspect. I am very grateful for his guidance on my research and my career. His scientific advice and helpful support during my dissertation are highly acknowledged.

I would like to acknowledge my next supervisor Prof. Dr.-Ing. habil. Norbert Haala. His scientific hints and helpful comments on the dissertation are highly appreciated.

Greatly appreciated are the helpful discussions with my senior colleague Dr.-Ing. habil. Johannes Engels. His scientific advice before and during my study had a great impact on my dissertation.

I would like to thank Federal Ministry of Education and Research for funding the project RoadInspect during my dissertation. I would like to thank Stuttgart University of Applied Sciences (Hochschule für Technik Stuttgart) for the convenient working situation during my research. My special thanks go to my colleagues Sokunthet Sok M.Sc. and M.Eng. Marius Ziegler for their teamwork during the project RoadInspect.

I would like to appreciate collaborations and helps of staff members at the Faculty of Environmental Sciences and Institute of Photogrammetry and Remote Sensing in TU Dresden. My special thanks go to Dr.-Ing. Patrick Westfeld, Dipl.-Ing. Christian Mulsow, Dr.-Ing. Danilo Schneider and Ms. Doris Salomon.

*To:*

*Mahvash and Aryandekht*

## Table of Contents

Abstract .....	i
Kurzfassung .....	iii
Acknowledgment .....	vi
Abbreviations .....	xii
1. Introduction .....	1
1.1. Background .....	1
1.2. Motivation .....	2
1.3. Road condition features (pavement distresses) .....	3
1.4. Problem statement and key questions .....	4
1.5. Objective and novel contribution of the dissertation .....	5
1.6. Structure of the dissertation .....	5
2. Related studies in road condition survey: data capture and processing .....	7
2.1. Mobile mapping systems for data acquisition from pavement surface .....	7
2.2. Laser scanning data .....	9
2.2.1. Road boundary/ surface extraction .....	10
2.2.2. Rut detection .....	11
2.2.3. Pothole detection .....	12
2.3. RGB images .....	13
2.3.1. Crack detection .....	13
2.3.2. Patch detection .....	15
2.4. Spectrometry data .....	16
2.5. Other related techniques for monitoring asphalt pavements condition .....	19
2.5.1. Ground Penetrating Radar (GPR) .....	19
2.5.2. Thermal imaging .....	20
3. Mobile mapping technology for multi-sensor based road condition mapping .....	21
3.1. System design .....	21
3.2. Laser scanning system .....	21
3.3. RGB camera imaging .....	22
3.4. Infra-red (IR) Spectrometry .....	22
3.4.1. Polytec spectrometer .....	22
3.4.2. Hand-held (Spectral Evolution) spectrometer .....	25
3.5. Geo-referencing, synchronization of the measurement devices with GNSS/INS .....	26
3.6. Study area and datasets .....	27
4. Concept of road distress detection and deterioration analysis .....	29

4.1.	Introduction .....	29
4.2.	Road surface and boundary extraction .....	30
4.2.1.	Principle of height jump detection.....	31
4.2.2.	Region growing .....	33
4.2.3.	Road boundary extraction.....	33
4.3.	Rut detection.....	34
4.3.1.	Rut detection using 1D polynomial fitting on the scanlines.....	34
4.3.2.	Rut detection using 1D cross-correlation .....	36
4.3.3.	Rut detection using curvature.....	37
4.4.	Pothole detection .....	38
4.4.1.	Pothole detection using geodesic morphological reconstruction.....	38
4.4.2.	Pothole detection using 2D polynomial fitting (curve fitting).....	40
4.5.	Crack detection.....	42
4.5.1.	Primary filtering for image smoothing .....	42
4.5.2.	Line filtering.....	44
4.5.3.	High-pass filtering.....	47
4.5.4.	Modified Local Binary Pattern (MLBP) .....	48
4.5.5.	Post-processing of the potential crack regions .....	50
4.5.6.	Feature fusion implementation .....	50
4.6.	Patch detection .....	51
4.6.1.	Patch detection using geodesic morphological reconstruction.....	51
4.6.2.	Patch detection using texture measures (gradient magnitude and local STD) .....	53
4.7.	Asphalt pavement quality analysis using spectrometry.....	57
4.7.1.	Spectral feature analysis .....	57
4.7.2.	Linear discriminant analysis (LDA).....	57
4.8.	Integration of road distresses and spectrometry classification outcomes.....	59
5.	Laser scanning data processing, results and discussion .....	60
5.1.	Road surface and boundary extraction .....	60
5.1.1.	Comparison of one- and four- neighbourhood regions growing .....	60
5.1.2.	Comparison of HDB and HB outcomes .....	62
5.1.3.	Comparing the results using different thresholds .....	64
5.1.4.	Accuracy assessment of the road surface extraction .....	65
5.1.5.	Road boundary extraction.....	66
5.2.	Rut detection.....	68
5.2.1.	Rut detection using polynomial fitting on the scanlines.....	68
5.2.2.	Rut and potential rut detection using 1D cross-correlation .....	76

5.2.3.	Rut detection using curvature .....	79
5.3.	Pothole detection .....	80
5.3.1.	Pothole detection using geodesic image reconstruction .....	81
5.3.2.	Pothole detection using 2D polynomial fitting on the laser scanning data.....	82
6.	Camera data processing, results and discussion .....	85
6.1.	Crack detection.....	85
6.1.1.	Crack detection using LF.....	86
6.1.2.	Crack detection using HPF .....	89
6.1.3.	Crack detection using MLBP .....	91
6.1.4.	Post-processing of crack detection results.....	92
6.1.5.	Comparison of crack detection using LF, HPF and MLBP.....	95
6.1.6.	Fusion of the crack detection results .....	98
6.2.	Patch detection .....	99
6.2.1.	Patch detection using geodesic morphological reconstruction.....	99
6.2.2.	Patch detection using texture measures (gradient magnitude and local STD) .....	100
7.	Spectrometry data processing, results and discussion .....	102
7.1.	Spectral feature analysis.....	102
7.2.	LDA results for separability analysis .....	104
7.2.1.	LDA result of hand-held spectrometer .....	105
7.2.2.	LDA result of mobile active spectrometer (Polytec).....	110
7.3.	Asphalt pavement classification using spectral signatures.....	111
8.	Integration of road distresses and spectrometry classification outcomes.....	114
9.	Conclusions and recommendations .....	117
9.1.	Study conclusions.....	117
9.2.	Recommendations .....	118
	References and bibliography .....	121



Parts of this dissertation including some figures have been published in the following proceedings:

Miraliakbari, A., Sok, S., Ouma, Y., Hahn, M. (2016):

**Comparative Evaluation of Kernel-Based Techniques for Pavement Crack Detection in Asphalt Road Images**, *Int. Arch. Photogramm. Remote Sens. Spatial Inf. Sci.*, *XLI-B1*, 689-694, doi:10.5194/isprs-archives-XLI-B1-689-2016, Prague – Czech Republic.

Miraliakbari, A., Hahn, M., and Sok, S. (2015):

**Automatic Extraction of Road Surface and Curbstone Edges from Mobile Laser Scanning Data**. *The International Archives of the Photogrammetry, Remote Sensing and Spatial Information Sciences*, *XL-4/W5*, 119-124, doi:10.5194/isprsarchives-XL-4-W5-119-2015, Tokyo – Japan.

Miraliakbari A, Hahn M (2014):

**Road Crack Detection in Images Recorded by a Mobile Mapping System**. In: *Proc. of Applied Geoinformatics for Society and Environment 2014 - Continuing Geospatial Education*, Stuttgart University of Applied Sciences, Stuttgart – Germany.

Miraliakbari, A., Hahn, M., Maas, H.-G. (2014):

**Development of a Multi-sensor System for Road Condition Mapping**. *The International Archives of the Photogrammetry, Remote Sensing and Spatial Information Sciences*, *Volume XL-1*, pp. 265 – 272, 2014. doi:10.5194/isprsarchives-XL-1-265-2014, Denver - USA.

## Abbreviations

ASTM: American Society for Testing and Materials

DCT: Discrete Cosine Transform

CRF: Conditional Random Field

FGSV: Forschungsgesellschaft für Straßen- und Verkehrswesen

FOV: Field of View

FN: False Negative

FP: False Positive

GIS: Geographic Information System

GLCM: Gray-Level Co-occurrence Matrix

GNSS: Global Navigation Satellite System

GPR: Ground Penetrated Radar

GPS: Global Positioning System

GVF: Gradient Vector Flow

HB: Histogram-Based

HDB: Height Distance-Based

HPF: High-pass Filter

IMU: Inertial Measurement Unit

INS: Inertial Navigation System

IR: Infra-red

LBP: Local Binary Pattern

LCMS: Laser Crack Measurement System

LF: Line Filter

LOD: Level of Detail

LRMS: Laser Rut Measurement System

MEMS: Micro-Electro-Mechanical System

MDNMS: Multiple Directional Non-Minimum Suppression

MLBP: Modified Local Binary Pattern

NIR: Near Infra-red

PCI: Pavement Condition Index

RANSAC: Random Sample Consensus

R&D: Research and Development

SI: structure Index

SF: Spectral Features

SMA: Sub Miniature version A

STD: Standard Deviation

SVM: Support Vector Machine

SWIR: Short Wave Infra-red

TN: True Negative

TOF: Time of Flight

TP: True Positive

UV: Ultraviolet

VIS NIR: Visible Near Infra-red



# 1. Introduction

This study presents a novel contribution for road condition mapping by means of the acquisition and automatic processing of three different data sources captured by: laser scanning, imaging and spectrometry. Combining the processing results from these captured data leads to the transition from so far predominantly manual to automated procedures in the field of road inspection.

## 1.1. Background

Roads, in general, are long and narrow infrastructures with a flat surface which facilitate transportation, travelling and communication by connecting one place to another (Oliveira, 2013). The road networks are able to relate two cities of a country (domestic road networks) or two countries of a continent (international road networks). Linguistically, “path” and “Pad” initially come from ground beaten by feet. The word “way” with the Sanskrit root (vah) indicates the concept of motion and travelling. Historically the first pathways which connected the surroundings were made by animals pushing away the bushes and pounding the ground with their feet. Already 10,000 B.C. roads were used by mankind (Lay, 1992). The existence of road is important in many aspects. Roads have become entirely the significant infrastructure for business, economy, transportation, medical care, sports, tourism, hobbies, etc. Generating a variety of the roads (different road classes) leads to the necessity of a high qualified transportation management system. With an increasing number of vehicles, the traffic becomes debatable (ERF, 2015) and it is important to investigate its negative effects on the pavement surface. Weather also plays an important role for the healthiness of pavement surfaces. Rain, snow and sudden change of the weather temperature force several distresses on the road pavement surfaces. Control and maintenance of roads are substantial for the municipalities and need to be expertly considered in an organized manner. For centuries roads have been constructed without geomatics. Recently, geomatics is utilized for quality control, continuous reporting and monitoring of the pavement changes which is accomplished with the help of laser scanners and profilers, ground penetration radar (GPR) and digital cameras, etc. That avoids expensive future restitutions and fixings. Road condition mapping concentrates on the maintenance and the rehabilitation rather than construction. Therefore, in contrast to the road construction which deals with the entire road surface, road inspection considers mapping of the deterioration and distresses of the upper road layer. Hence, the equipment used for road condition mapping should consider the uppermost layer of the road. Despite present modern technology in surveying engineering, one of the common ways of road inspection is based on human inspection which is still ongoing in many developing and developed countries. Human inspection in the field is time consuming and lacks repeatability. The longer the field work lasts the observation quality decreases. On the other hand the manual inspection is ‘prone to subjectivity’ (Oliveira, 2013). It happens that two inspectors might have different ideas about the quality of the same road section which they have inspected. Contrary to the traditional road inspection, the automatic option gains advantages such as time, cost efficiency and repeatability. For the automatic variant, two general steps are introduced, namely: data acquisition and processing. The more important concern of this dissertation is the automatic road surface data processing; however, the data acquisition is also addressed in detail.

Several researches have been carried out for road condition mapping. In this dissertation, relevant studies about the pavement condition and distress mapping by means of laser scanning, imaging and

## 1. Introduction

hyperspectral remote sensing are reviewed intensively. Other systems are not taken into account in this dissertation such as GPR (Casas, et al., 2000), geographic information system-based (GIS-based) and thermal-based solutions. Some vehicle-based platforms are available which carry the GPR system (The Mara Nord Project, 2012). GIS-based solutions are a combination of visual inspection and mobile GIS-based reporting. Thermal infrared-based road condition mapping focuses mostly on moisture ingress. The moisture ingress might damage the road structure. It is likely to find the water ingress using thermal infra-red imagery. If the water enters the road structure, it changes the procedure of heating up and cooling down the road layers. Therefore, road sections including water are often visible in the thermal images (FLIR, 2016).

### 1.2. Motivation

Accurate information about the pavement condition is important for the overall management of transportation infrastructure (Herold, et al., 2003). This information, presented as either maps or databases, helps decreasing the costs of maintenance and rehabilitation of the road pavement surface. The public road networks get deteriorated in many municipalities as essential investments are delayed or withdrawn. Mapping and localizing the exact position of pavement failures are crucial prerequisites for maintenance management.

In general, pavements disfigure and deteriorate as a result of the physical and chemical changes of the road surfaces. Manifest asphalt distresses like longitudinal and transverse unevenness, ruts, potholes, shoving, various kinds of cracks and unlevelled patches, etc., (FGSV, 2001), (ASTM-D6433, 2008) (Shahin, 2005) are significant geometrical perturbations of the smooth road surface. Several researches have focused on the physical failure and deteriorations of the uppermost road layer. Aside from the evident asphalt failure, surface roughness is broadly considered as an important surface condition parameter (FGSV, 2001). The investigations on the asphalt distresses take mostly advantage from accurate surveys, especially by laser scanners, laser profilers and digital cameras. Blatant pavement failures can be monitored and investigated by cameras (Blades & Kearney, 2004). The laser scanner provides 3D information of the pavement surface. A few companies are engaged in road condition mapping and evaluation. They have concentrated on some of above mentioned pavement failures. These companies capture mostly a large amount of data (point clouds and image data) related to the road networks. So far automation and data processing are not advanced. Therefore, operators must sit in front of the computer and detect manually the distresses such as cracks and ruts from the captured mobile data. Fully automatic pavement distress detection and evaluation of road condition is an unsolved challenge.

One aspect of visual inspection is the impression people take from aging of the asphalt. More specific access to the road degradation is addressed by (Herold, et al., 2004). They proposed spectrometer and hyperspectral remote sensing for road deterioration analysis. For road condition mapping, airborne hyperspectral remote sensing captures image data with a ground resolution which mostly does not fulfil the requirements of road condition mapping. For instance if the airborne hyperspectral data has ground resolution of more than half of the lane width, e.g. 2 m to 4 m, the pavement information is the mixture of the features such as vegetation, road marks, curb lines and shadows coming from the neighbouring trees. The alternative is to use spectrometer in order to map and analyse asphalt deterioration.

A spectrometer is a sensor which registers the radiation reflected from the surface. As this sensor samples the reflectivity curve as a function of the wavelength in the near and short wavelength infrared (SWIR), some indications of the aging can be derived (Herold, et al., 2004).

In a traditional way of data acquisition for road condition mapping, apart from GIS tools as keeping and monitoring the captured data, most of the physical failures are recorded and measured by visual inspection and measurement techniques employing rulers, tape rules, rods and slats. Therefore, most of the current standards report about the criteria of road condition evaluation based on the traditional data acquisition. In this case the absence of high-end automated data recording and processing system is obvious. Fully automatic data recording and processing which follow the standards of road condition mapping are desirable and require:

- Conceptual approach for multi-sensor integration and data capture
- Mobile mapping sensors (camera and laser scanner)
- Navigation sensor for geo-referencing captured data
- Tools for raw data processing
- Fundamental understanding of pavement distresses

### **1.3. Road condition features (pavement distresses)**

There are several pavement distresses which are indicated for understanding the degree of severity of road pavements. DIN-Norm, working packages of Research Society for Roads and Transport (FGSV) and American Society for Testing and Materials (ASTM) are some of German and US standards for road pavement condition mapping and evaluation. According to these standards, several pavement distresses are introduced and described. In this dissertation, measurement and analysis of the pavement distresses are limited to the following elements, namely: rut, pothole, crack and patch.

#### **Rut**

Rut is a depression of the pavement surface in the driving direction. Although in some cases uplifting of the sides of a rut can happen, the manifestation of a rut is observable after raining. A rut is mostly generated by interactive or lateral movement of vehicles. The severity of the rut is decided by the mean depth of the rut. Calculation of depth of the rut is based on laying a straight edge across the rut. After measuring its depth, the measurement must be done continuously along the length of the rut in order to get the mean depth in mm (ASTM-D6433, 2008). Due to the variety of the standards, the severity degree of a rut differs from one country to another.

#### **Pothole**

Pothole is bowl-shaped distress in the surface of the pavement which is small and less than 750 mm (ASTM-D6433, 2008) or 900 mm (Shahin, 2005) in diameter. There are sharp edges and vertical sides near the top of the potholes. Free moisture collection inside the hole usually accelerates the growth of the pothole. Potholes are generated when the traffic loads impair the small fragments of the pavement surface (Shahin, 2005), (ASTM-D6433, 2008).

#### **Crack**

Pavement crack in general is a narrow space between components (mostly aggregates) of the pavement which is visible on the uppermost road layer.

## 1. Introduction

Pavement cracking might appear as individual lines or a connected network. Cracks allow water to enter into the road pavement surface. In the freezing period, the infiltrated water destroys the uppermost pavement surface layer (Maerschalk & Oertelt, 2014). According to the Cornell local Roads Program (Orr, 2006), asphalt pavement cracks generally categorized into: fatigue (alligator), longitudinal, transverse, block, slippage, reflective and edge.

### **Patch**

Patch is a certain area of the road surface which is replaced with a new paving material in order to repair the pavement. Regardless of how well the patch is performing, it is considered as a failure on the pavement surface because the patch and its neighbouring area do not act the same as the intact pavement section (ASTM-D6433, 2008).

## **1.4. Problem statement and key questions**

### **Pavement surface distress detection**

Cracks, patches, ruts, potholes, etc. are common pavement surface distresses which are to be detected and analysed for road condition assessment. Accurate data capture and proper raw data processing (e.g. geo-referencing, outlier removal, etc.) are essential steps for pavement surface distresses detection. Data capture and raw data processing are mostly done by commercial companies, however the automatic detection and integration of road pavement distresses appears to be a remaining unsolved problem. Researchers have tested some sensors for capturing information from the pavement surface. Inspired by the experimental investigations of the researchers such as (Huang, et al., 2009), (Laurent, et al., 1997), (Gavilán, et al., 2011), (Oliveira & Correia, 2014) the most proper sensors for collection of 2D and 3D information from a road surface are cameras and laser scanners (and profilers), respectively. Researchers have proposed detection methods for mostly one or two of the above mentioned distresses. The challenge is to develop a comprehensive approach for automatic detection of several pavement distresses. This is to be done by testing and analysing different detection methods and selecting the most robust one for detection and integration of the distresses.

Any kind of pavement surface distress can appear on the road with individual shape, length, width and depth and may even change with weather conditions. It is hardly possible to find two samples of the same pavement distress which have equal dimensions. The question is: Which approach can mostly detect every sample of a distress?

### **Material characteristics analysis**

So far no innovative idea is followed in order to analyse the material characteristics of the pavement surface. The low resolution of airborne hyperspectral data is insufficient to indicate and evaluate the material characteristics of the pavement surface. Using such coarse resolution hyperspectral data will cause following problems: Mixture of asphalt radiation with neighbouring materials; the neighbouring object materials such as curbstones, pedestrian area manhole covers have mostly different characteristics from the asphalt pavement. If the ground resolution is coarse, the spectrum related to this area will represent the mixture of asphalt and the neighbouring materials. Another difficulty is obstacles. Using the remote sensing data, it is not possible to get rid of obstructions such as cars, cranes, etc. Equally or even more important is the crown of the trees standing on the sidewalks of the



narrow streets. On the other hand, it is impossible to have image data from the roads which are under the tunnels. One of the other difficulties is shadow. Crown of the trees and building facades profiles can cause shadow on the street which might degrade the nature of the spectrums which is irradiated from the asphalt road surface. In this case, the spectrum will be contaminated by the occurrence of the shadow.

Can mobile spectrometry be an alternative for judgement of the road material characteristics? If yes, how can it contribute to the mapping of the road conditions?

### **1.5. Objective and novel contribution of the dissertation**

The objective of this dissertation is to develop an approach for road condition mapping by integration of laser scanning, RGB imaging and spectrometry. The methods which are developed for detecting cracks, patches, ruts and potholes shall be able to cope with variety of data sources in different weather and asphalt conditions. A framework is developed to connect all detected distresses and the result of asphalt quality analysis for assessment of overall road condition in each road segment. The novelty of the research is that it:

- a) proposes methods of road condition feature detection which are adaptable with different kinds of asphalt pavement surface and weather condition.
- b) integrates laser scanner, camera and spectrometer for road inspection.
- c) contributes to the road condition mapping. With respect to the human inspection in the field and manual procedure (e.g. digitizing) at the computer, the progress through automation is obvious.
- d) points to a concept of integrating of detected distresses with the classification result of pavement surface material for overall road condition mapping.

### **1.6. Structure of the dissertation**

At the end of the introduction, an outline of the main content of the dissertation is given: the second chapter focuses on the related studies and previous researches based on road condition mapping using laser scanning, imaging and spectrometry data. Chapter 3 covers mobile mapping technology for multi-sensor based road condition mapping. This chapter points out system configuration, data capturing principles and data integration.

Chapter 4 is the main section of this dissertation. It includes an outline of the proposed concept for road condition mapping by integration of laser scanning, RGB imaging and spectrometry. The concept is proposed and discussed in section 4.1. In the following sections, mostly two or more of the methods which have been implemented for road surface distress detection are described. Section 4.2 describes

## 1. Introduction

variants for road surface and boundary extraction using laser scanning data which is a preparatory step for rut and pothole detection. Laser scanning profiles and interpolated regular grids are used for rut and pothole detection. Section 4.3 covers the rut detection methods. In this section, 1D polynomial fitting on the laser scanning profile, 1D cross-correlation and curvature estimation are utilized for the rut detection. Pothole detection approaches are covered in section 4.4 using geodesic morphological reconstruction and 2D polynomial fitting on the laser scanning data. RGB images are the input data for cracks and patch detection. Section 4.5 is dedicated to a detailed description of crack detection methods including pre- processing, post-processing and fusion steps. Implementation of three kernel-based crack detection approaches is described in this section. The implemented methods for patch detection are described in section 4.6. In this section, gradient magnitude and local standard deviation (STD) are two main criteria used for the patch detection. Section 4.7 points out the asphalt pavement quality analysis using spectrometry data. The objective of using spectrometry data is to classify the pavement sections into two classes, namely: “Good” and “Bad” classes.

Chapter 5, 6 and 7 describe the results of each data source. They explain experimental investigations and results of the laser scanning, image and spectrometry data processing for road condition mapping. Integration of road pavement distresses is reported in chapter 8. Conclusion and prospect are addressed in detail in the final chapter.

## 2. Related studies in road condition survey: data capture and processing

The demand for digital data acquisition for the surveying purposes is increasing. By increasing traffic volume, pavements need to be mapped and evaluated to guarantee road safety and optimal use of public budget. Therefore, there is a growing need for the development of automated techniques which can capture pavement surface and analyse road distresses. Several research institutes, consulting companies including research and development (R&D) or the commercial ones have been focusing on the new approaches of road surface condition mapping. This chapter presents the state of the art of data acquisition and processing for road surface condition mapping. Related researches about the road condition feature detection and evaluation are discussed in this chapter.

### 2.1. Mobile mapping systems for data acquisition from pavement surface

Several commercial companies deal with the mobile mapping data captures for road condition mapping. Some of the road condition mapping systems are described in Table 1. The main strengths and limitations of these systems are briefly mentioned.

Company name	System	Strength	Limitations
Vectragermany Lehman + Partner	I.R.I.S	Accurate GNSS/INS system, High-resolution camera, proper mounting of laser scanner for road surface data capture	
	S.T.I.E.R	Accurate GNSS/INS system, High-resolution camera, proper mounting of laser scanner for road surface data capture	Laser scanner's profile width is 4 m on the road surface
TÜV Rheinland Schniering	ARGUS®	Short exposure time of 1/50,000 sec for aligned cameras	Large lateral measurement intervals (10 cm) for the laser distance sensors
	ARGUS®-AGIL	Small size of the vehicle van, possibility to map bike way condition	No INS is included in the navigation system
	ARGUS®-PROFI (Profilometer)	Highway temperature measurement	Distress measurement is mainly limited to longitudinal unevenness

## 2. Related studies in road condition survey: data capture and processing

Pavemetrics	LRIS	1.0 mm transverse resolution, operation capability at day or night	4m width of scanning coverage
	LCMS2	1.0 mm transverse resolution, 0.25 mm vertical accuracy	
	LRMS	Operation capability at day and night, 1 mm vertical accuracy	Profile width is 4m on the road surface, the system is only capable to detect ruts

Table 1. Some exemplary road condition mapping systems (LEHMANN and PARTNER GmbH, 2016), (TÜV Rheinland Schniering GMBH, 2017), (Pavemetrics, 2017)

Apart from all prior solution companies which concentrate on hardware solution and data acquisitions, several companies focus on object extraction from mobile mapping data. OrbitGT is one of those companies which offers solutions for mobile mapping data management and feature extraction. The software package of this company enables extraction and measurement of urban objects such as building facades, pedestrian zones, road surfaces, road distresses, etc. The software package facilitates manual object extraction such as window frames of the facades, poles, traffic lights, curbstones, etc. It provides the users with many useful viewing options such as top, side and even panorama view. Point cloud colourization by means of the geo-referenced RGB images is an additional option of the provided tools. Measurement of position, distances and areas is supported by the package (Orbitgt, 2016).

Several researches have been carried out to implement and test multi sensor platforms for road condition mapping. A system prototype proposed by (Kertész, et al., 2008) is composed of a van vehicle on which the navigation system (GPS/INS unit), an RGB camera and a laser projector are mounted. They claim that by detection of the projected laser line in the image, small abnormalities on the pavement surface can be detected. By introducing the known geometric relationship between the line of the laser projector and the images taken from camera, the profile of the height in space is reconstructed. This reconstruction leads to the recognition of the height changes along the track. From the theoretical point of view, their method is appropriate however, in practice, there should be several tests to prove the stability of the prototype system. The quality of height measurement highly depends on the resolution of the image data and it is necessary to use a high resolution camera. On the other hand, sudden jumps of the vehicle due to the severe pavement distresses, vibration of the motor and existence of the huge undulation on the pavement surface misdirect the projected laser line and damage the height profile.

(Yu, et al., 2007) report about 3D reconstruction of road surfaces using an integrated multi-sensor approach. Figure 1 shows their prototype system which is composed of laser scanner, video camera, GPS and IMU. The laser scanning system is SICK LMS 200. For the navigation purpose, they employ Leica GPS System 500 and Xsens MT9 IMU. They utilize a Sony DCR-TRV730 Digital Camcorder video camera to accomplish imaging. They report about the positioning accuracy of 2cm at sampling frequency of 10 Hz delivered by the differential GPS system. They state that the utilized laser scanner is relatively noisy because by scanning of indoor concrete surface, the RMS of 8000 profiles amounts to 0.6 cm (Yu, 2005). The workflow of reconstruction of 3D pavement surface model contains: acquisition of the data, segmentation and registration of laser scanner profiles and 3D pavement surface reconstruction.



Figure 1. The prototype of mobile mapping system composed of laser scanner (bottom inset) and video camera, and GPS/IMU (top inset) (Yu, et al., 2007)

A drawback of the prototype system is the GPS/INS system. In their prototype, the IMU system was a low cost Micro-Electro-Mechanical System (MEMS) device employed with a high-end GPS system. Although their GPS system has high positional accuracy, facing difficulty in satellite observation (which is quite common in the urban area) causes problems for geo-referencing of the raw laser scanning point clouds. Relying on the low cost IMUs for geo-referencing when there is no GPS signal available is not recommended.

The next sections follow primarily main mapping sensors used in this study. Related researches are discussed with respect to laser scanning data in section 2.2, to RGB images in section 2.3, to spectrometry data in section 2.4 and to other data like GPR and thermal images in section 2.5.

## 2.2. Laser scanning data

Land vehicle based mobile laser scanning provides 3D information of the road surface and its distresses. The captured point cloud represents the geometry of the surface explicitly is therefore utilized to detect pavement distresses such as ruts and potholes.

## 2. Related studies in road condition survey: data capture and processing

### 2.2.1. Road boundary/ surface extraction

Road extraction is a vast field of research. Aerial images, laser scanning data and high-resolution satellite images are the typical data sources for road extraction. Generation and updating of the road maps are the main reasons of such developments. However, the resolution of these data sources is limited and not many details of a road surface are visible in these data. Mobile laser scanning overcomes this limitation. The extraction of road surface data from mobile laser scanning is a preparatory step for many road monitoring projects. For that, the road surface must be separated from other features such as sidewalks, trees and cars.

(Vosselman & Liang, 2009) investigate curbstone detection using airborne laser scanning point clouds. Potential curbstone positions which are the locations of ‘height jumps’ are detected in their research. The line topology is reconstructed and the gaps between the road boundary outlines are bridged. Curbstone detection using airborne laser scanning data is successful if there is a sufficient height difference between the road surface and the sidewalks. However, there might be always a chance to face shallow curbstones especially in front of the park houses and at the bikeway junctions with the road. In this case, there is no guarantee that shallow curbstones will be detected using airborne data.

(Siegemund, et al., 2010) examine curbstone reconstruction using conditional random field (CRF). CRF is a graph-based approach used for two sets of variables which are at the neighbourhood (Lafferty, et al., 2001), here road surface and sidewalk. They use CRF to label road surface and sidewalks and estimate the curbstone parameters using sigmoidal function. Using stereo matching techniques, they generate dense 3D point cloud from images and use it as input data. The images are taken from the cameras mounted behind the windshield of the vehicle. The images cover areas with pavement surface, curbstones and sidewalks. Their approach reconstructs the curbstones which are fitted to the straight-line or higher order polynomials; however, the minimum height of the detected curbstones is limited to 4 cm. Problematic might be the position of the camera. The windshield may contaminate radiometric characteristic and distort geometric property of captured data with the consequence of a downgraded point cloud quality.

(Gallo, et al., 2008) investigate curbstone detection using the “Canesta” camera which is a time-of-flight (TOF) camera. Their plane-based approach works with a version of Random Sample Consensus (RANSAC) called CC-RANSAC. While the ordinary RANSAC considers all inliers, the alternative version takes only the largest associated components of inliers into account. They argue that the proposed method does not let RANSAC fail if shallow curbstones appear in the search area. They regard their approach as cost-effective because of the fewer number of required iterations.

(El-Halawany, et al., 2011) work on curb line detection using mobile laser scanning data. In the first step, the ground regions (such as pavement surface, curb lines and pedestrian area) are separated from non-ground regions. They assume that the angle between surface normal and horizontal plane is approximately  $90^\circ$  and consider the direction of the surface normal for the separation of ground regions i.e. pavement surface, curbstones and sidewalks. Their detection consists of 3D and 2D approaches. In 3D approach, they isolate the curb using elevation gradient within the local neighbourhood, direction of surface normal and eigenvalues. They consider explicit thresholds for each of those parameters to separate the curb line from road surface and sidewalks. The 2D approach is carried out using rasterized height data. Canny edge detection method is used to detect the curb edges. They state that the precision and recall of 2D approach are 97% and 94%, respectively while 3D approach performs precision of 83% and recall of 78% for the same study area. The comparison

between two methods shows that the 2D approach is more reliable, however, the study is limited to a small region and it is not guaranteed if the proposed 2D approach is able to detect low curbstones.

### 2.2.2. Rut detection

Researches in automatic rut detection are focused on laser triangulation and laser scanning data. There are a number of rut detection systems based on the principle of laser triangulation. Two well-known systems are Laser Rut Measurement System (LRMS) developed by (Laurent & Hebert, 2002) and TxDOT VRUT developed by (Huang, et al., 2009). Both developments have led to commercially available systems.

The principle of laser triangulation is the following: A laser line is projected on the pavement surface. The reflected laser line is captured by a camera. By simultaneous imaging and laser profiling, there will be a 'triangulation relationship between the image pixel shift and the real height of the target'. By triangulation, each point of the laser line is converted into a 'vertical height measurement' and transferred into an array of surface height data (Huang, et al., 2009).

The concept of rut measurement in LRMS and TxDOT VRUT systems goes back to (Laurent, et al., 1997) publication. The algorithm is based on fitting straight-line segments on the top of the profiles so that the largest deviation of the profile from the line segment defines the rut depth.

(Laurent, et al., 1997) propose an automatic technique for rut detection from laser scanning data. They approximate the road profiles using 'iterative end points fit' according to (Ramer, 1972), (Douglas & Peucker, 1973). At first, they fit a straight-line through the endpoints of a laser scanning profile. They detect a point  $P$  of the profile which has the maximum distance from the initial straight-line. They break the straight-line into two new lines which start from  $P$  to the endpoints. They iterate the process until the maximum distance from the straight-lines and the points on the profile is less than a predefined threshold. Moreover, they search for the 'rut support points'. These are points on the road profile that 'see each other'. 'Seeing each other' means that if a straight-line passes through these points, the line will not intersect the road profile. The rut depth is finally determined by calculating the maximum distance between the line which passes through the rut support points and the line segments on the road profiles. This idea will be picked up again in section 4.3.1, where a 1D polynomial fitting is proposed as an approximation through 'rut support points'. Regarding to their road profile approximation, the threshold must be very low (e.g. less than 0.5 cm) to get all ruts and even potential ruts. This low threshold makes the line segmentation process more sensitive.

(Laurent & Hebert, 2002) report their transverse profiling system called LRMS. Using this system, they compare automatic and manual rut measurement. They state that over 100 m pavement segment, the mean bias is less than 1 mm. (Laurent, et al., 2012) developed LRMS further and call the new system called Laser Crack Measurement System (LCMS). The LCMS has the capability of detecting cracks and ruts. It consists of two 3D laser profilers. These laser profilers enable measurement of transverse profiles with 1 mm resolution. They generate range image data in 2.5 D space from these profilers.

(Huang, et al., 2009) publish their research report about 'a Rut Measurement System Based on continuous transverse profiles From a 3-D System'. They develop a system called TxDOT VRUT which works based upon the laser triangulation 3D principles. The system component used in their research is quite sensitive against the vibrations and sudden bumps during driving. If there is any pavement distress below the test vehicle tires, the vehicle jump can cause misdirection of projected laser lines.

## 2. Related studies in road condition survey: data capture and processing

### 2.2.3. Pothole detection

According to (Koch & Brilakis, 2011) research on pothole detection can be categorized into 3D reconstruction-based, vibration-based and vision-based variants. (Kim & Ryu, 2014) introduce subclasses for 3D reconstruction-based and vision-based approaches. Based on their classification, the 3D reconstruction-based approaches include 3D laser scanning-based, stereo vision-based and Kinect-based methods. They classify the vision-based approaches into image-based and video-based variants.

(Koch & Brilakis, 2011) investigate asphalt pavement pothole detection using a stream of images. They employ a fish-eye camera with the ability of tilting downward in order to capture image sequences of the pavement surface. They make use of three visual characteristics of the potholes namely: a. depending on the sun direction, a pothole has shadow (shade) area which appears darker compared to the surrounding region, b. Pothole has mostly elliptical shape, c. It has coarser texture compared to the texture of surrounding pavement (intact) region. They first segment images into defect and non-defect areas. Based on a triangle algorithm (Zhu & Brilakis, 2010) they employ a histogram shape-based thresholding. The threshold indicates the defect and non-defect regions. Afterwards they approximate the potential pothole region using geometric properties of the injured region. The small objects and the linear shape regions are removed. They approximate the elliptical shape of the pothole using the detected shade. Skeleton-based algorithm is utilized to shrink the shade region. The branching points of the shade skeleton are recognized and connected to construct the major route of the shade area. Moreover, the ellipse is approximated using major path elliptic algorithm (Fitzgibbon, et al., 1999). Furthermore, they extract the texture inside the injured region and compare it with the regions which are in the vicinity of the potential pothole area (intact asphalt). If the texture inside the potential pothole area is coarser than the one belonging to the non-defect area, this potential area is considered as pothole region. However, the sun elevation angle might be very high that causes minor shadow. On the other hand, the pothole can be old so that the texture criterion may not be applicable.

(Zhang, et al., 2014) implement an algorithm for pothole detection using stereo vision. They use the disparity map to detect potholes. The disparity map was transferred to the world coordinate system and then potholes were extracted using surface fitting. For surface fitting, they use 'low computational bi-square weighted robust least-squares method' (Golub & Von Matt, 1991) (Ai, et al., 2013). First, they fit the surface using normal least squares. Afterwards, they minimise and normalize the residuals, compute the bi-square weights and check the convergence criterion for fitting. After fitting the curve on the pavement surface, the points belonging to the pothole region is identified using a certain threshold on the Euclidean distance between the points of the road and fitted surface. Similar approach is proposed by (Chan, et al., 2014).

(Moazzam, et al., 2013) investigate pothole detection by means of the Microsoft Kinect Sensor. In their study, the Kinect images are taken at 0.8 m to 0.9 m above the road pavement surface. Using local minimum, they localize the pothole pixels in the depth image. They calculate the pothole area and the depth of the potholes. Using trapezoidal rule, they compute the pothole volume. The sensor which has been used is adequate for the test phase and might not be proper for commercial applications. In another related research, Mobile Kinect-based pothole detection is reported by (Joubert, et al., 2011). The point cloud of the scene containing the pothole is generated by Kinect. Pothole edge is determined by estimating the plane of the pavement scene using RANSAC and points



located below the surface are identified as potential pothole points. They identify the pothole edges using contour detection.

(Yu & Salari, 2011) report about the road surface pothole detection using laser imaging. After data capturing, they divide the image scene into sub-images where each sub-image (tile) consists of  $40 \times 40$  pixels with ground resolution of 2 inches to decrease the computational complexity compared to pixel-based computation. They determine the shape of the pothole by detecting the deformation of the laser lines. The deformation detection is carried out using template matching. A straight-line is introduced as predefined template frame and compared with each tile of the input data. If the template does not match with the tile, the tile will be identified as deformation. Furthermore, a three-layer feedforward neural network for pothole severity classification is employed.

Vibration-based pothole detection methods by means of accelerometer are reported by (Rode, 2007), (Silva, et al., 2008), (Mednis, et al., 2001) and (Kim & Ryu, 2014). The pavement distresses such as ruts and potholes make impacting forces on the test vehicle. The accelerometer mounted in the vehicle records the vehicle responses to the forces. Sudden jumps identify the location of the pavement distresses. These methods need small storage and are adequate for real-time processing (Kim & Ryu, 2014) (Koch & Brilakis, 2011). However, they may highly depend on the location of the vehicles and decrease the chance of fully pothole detection. (Koch & Brilakis, 2011) criticize the vibration-based pothole detection: They report that (Eriksson, et al., 2008) realized this method ends up with false results, for instance, bridge expansion joints might be wrongly detected as potholes. On the other hand, if the lane centre has a pothole, the chance of hitting the car wheel on that area is almost zero. Last but not least, potholes are dangerous obstacles and their detection by means of the direct contact with vehicle has risk of accident.

## **2.3. RGB images**

### **2.3.1. Crack detection**

Crack detection can be found in many applications from industry to medicine and surveillance detection. One of the major focuses on pavement distress detection is pavement surface crack detection and many researches have been carried out to detect pavement cracks predominantly but not exclusively in images.

(Gavilán, et al., 2011) assume that cracks shown up in the pavement images are linear elements which are darker than the neighbouring objects. They are somewhat continuous with a dominant orientation (Lee, et al., 2007). (Gavilán, et al., 2011) mention that these assumptions lead to implementation of several crack detection methods: an initial implemented approach is based on the assumption that images contain only crack and non-crack pixels and can be represented as a bimodal histogram. Hence, by applying a threshold (Otsu, 1979), the pavement image can be classified into crack and non-crack classes. However, depending on the threshold value, using this method ends up having either a lot of noises in the binary data or omitting the crack pixels. (Gavilán, et al., 2011) reported that threshold-based methods have been improved using morphological operations. They mentioned that transform-based approaches such as Wavelet are employed for crack detection purposes. Several approaches are used for crack detection based on classifier ensembles. Using these approaches, the pavement image is split into certain number of cells and the detection method tries to determine crack

## 2. Related studies in road condition survey: data capture and processing

cells. Further developments are based on Neural-network, support vector machine (SVM) and the supervised learning and k-nearest-neighbours. (Gavilán, et al., 2011) declared that the disadvantage of using these methods is that the user needs to provide high amount of training data in order to perform a good classification result.

(Oliveira & Correia, 2014) develop an image processing toolbox (CrackIT) for crack detection. Their software consists of pre-processing, crack detection, crack characterization and evaluation. In the pre-processing part, after smoothing the image and separating the white lane lines from the scene, the image is scanned vertically and horizontally in order to find the image blocks which are which have sudden intensity changes and potentially presenting the crack positions. For crack detection, they propose two methods which are called block-based and pixel-based methods. The first method consists of automatic training data selection, extraction of stochastic features which are mean and STD of the intensity of the pixels within each block, feature normalization and labelling the blocks which can be shown as crack or non-crack (Oliveira, 2013). In the pixel-based method, initially the images are segmented based on automatic histogram thresholding. Furthermore, crack candidates are introduced and grouped by a connected components algorithm if they fulfil following geometric requirements: a) if they fit an ellipse on the component, the eccentricity of the ellipse must be more than 70%, b) the width of the component must be equal or greater than 2 mm and (iii) the major axis of fitted ellipse must be larger than 25 pixels. Then linkage between the components is applied and the cracks are identified (Oliveira, 2013).

(Gavilán, et al., 2011) detect the pavement cracks by means of a seed-based method. Their procedure steps are as follow: pre-processing, non-crack feature detection, road surface classification and road distress detection. In pre-processing step, noise reduction and contrast enhancement are carried out. The main idea of non-crack detection step is to eliminate the elements which might be misidentified as crack regions such as sealed cracks, road marks and joints. They employ a basic (non-adaptive) threshold for the non-crack filtering process. Furthermore, road classification is applied using a multi-class SVM (Chang & Lin, 2016) to optimize the crack detection algorithm. They classify the pavement surface dataset into 7 asphalt and 3 concrete surfaces. Lastly, their crack detection approach consists of seed-based approaches (Sun & Vallotton, 2006) (Yamaguchi & Hashimoto, 2006). These methods has two common steps; initially, local minima of a grey scale image, which seem to be cracks, are selected as seed points, secondly, routes between the seed points are attained using path growing techniques. Multiple directional Non-Minimum Suppression (MDNMS) for detection of linear features is considered to achieve the seeds together with a symmetry check (Sun & Vallotton, 2006). According to (Sun & Vallotton, 2006) and (Gavilán, et al., 2011), Non-Minimum Suppression is a process of labelling all pixels which their intensity is not minimal as zero within a local neighbourhood. They define local neighbourhood as multiple directional linear windows with the angular increment of 45°.

(Subirats, et al., 2004) investigate the role of wavelet transform in crack detection of pavement surface images. The problem of the crack detection is that it is hard to detect the cracks via edge detection methods. They employ wavelet transform to detect the cracks using initially a laboratory dataset which has ideal condition to detect the cracks. It means there is no shadow as obstacle on the surface of the test field to influence the detection results. The ‘Symlet5’ is the wavelet family used in their research. They claim that the proper wavelet family is mother wavelet symlet5 and suitable for the noisy images. Since cracks can appear in both longitudinal and traversal directions, the drawback of using 1D wavelet transform is that cracks which are in one direction can be distinguished. (Subirats, et al., 2006) propose to use 2D continuous wavelet transform- based method for crack detection and test Mexican hat function as mother wavelet.

(Mancini, et al., 2013) detect pavement cracks from mobile images, applying Gradient Vector Flow (GVF) snake. Snakes (Kass, et al., 1988) or active contours are widely employed to localize boundaries of objects (Xu & Prince, 1997). (Mancini, et al., 2013) state that in the segmentation cannot be solved by snake algorithms, ‘since which have some problem with the model initialization and the non-convergence to concave boundaries.’ Therefore, (Mancini, et al., 2013) introduce a modified version of the snake algorithm called Snake GVF proposed by (Xu & Prince, 1997). (Mancini, et al., 2013) make use of the gradient of the scene (in  $x$  and  $y$  direction) to generate the edge-map of crack regions. Furthermore, GVF force field is computed on the edge-map result and the snake model from GVF force field is finally generated. The final results end up with detected crack edges which is wider than the original (ground truth) crack.

Several other image-based crack detection methods are proposed and investigated. (Maas, 2012) presents the Fly-fisher algorithm which is based on the edge detection using gradient operators. Other researchers use different methods such as SVM presented by (Marques, 2012) and local binary pattern (LBP) which is proposed by (Hu & Zhao, 2010).

The input data for crack detection not restricted to the imagery data. (Pavemetrics, 2017) use the range image captured by the 3D laser profiler for crack detection. The intrinsic assumption of the approach is that cracks are deeper than its neighbourhood. The depth resolution of the laser data is high enough (0.5 mm) to differentiate the cracks from non-crack regions (Laurent, et al., 2013).

### 2.3.2. Patch detection

(Radopoulou & Brilakis, 2015) investigate patch detection for pavement evaluation. They employ a video camera to capture the pavement surface. They split their methodology into two steps namely: image pre-processing and patch detection. The goal of the pre-processing step is to reduce unnecessary image information and enhance the image data for patch detection. For that, they convert the image into the grey scale, remove image noise by median filtering and improve the image contrast. In patch detection step, they search for objects with closed contours, because they claim that the patches are represented by a closed contour. They extract objects with closed contours and associated them with potential patch regions. The patch detection step is continued by studying the texture characteristics of the potential detected patches. Finally they use STD to obtain the patch regions.

(Hadjidemetriou, et al., 2016) examine automatic pavement patch detection using SVM classification. Their proposed process consists of two steps namely: SVM training and testing. The RGB images are converted into grey scale matrices to reduce the unnecessary computation time. Furthermore, they divide the matrix into the tiles (blocks) with  $20 \times 20$  cell-size. They construct SVM feature vector and therefore trained the SVM by means of information taken from the tiles of the images. The feature vector is generated using local intensity histogram of the tiles, and two texture descriptors namely: Discrete Cosine Transform (DCT) and Gray-Level Co-occurrence Matrix (GLCM). The same routine is accomplished for SVM testing and classification of the test blocks to divide the images into patch and non-patch regions.

## 2.4. Spectrometry data

Description and explanations in this section follow closely the publications in (Herold & Roberts, 2005b) and (Heiden, et al., 2007). Aging of the asphalt degrades the pavement quality. This deterioration changes the material characteristics of the pavement surface. As the material characteristics of components of environment can be analysed by spectral signatures of remote sensing data, (Herold, et al., 2004) propose to use spectrometers for the analysis of pavement surface quality.

(Herold & Roberts, 2005a) investigate road condition using hyperspectral remote sensing. They employ two hyperspectral data sources namely: AVIRIS and Hyperspectir with 4 m and 0.5 m ground resolution, respectively. They state that the newly paved asphalt roads are influenced by hydrocarbon absorptions. Furthermore, they conclude that the asphalt pavement aging proceeds with 'gradual transition from hydrocarbon to mineral absorption characteristics.' Moreover, the general brightness of the spectral signature increases. One of their major outcomes is analysis of crack behaviour in the spectral results. They find out that the existence of crack portions on the road reduces brightness and increases representation of the hydrocarbon features in the hyperspectral data. This is due to the visibility of the organic materials of asphalt mix which are located in the lower pavement surface and gain visibility during cracking. Furthermore, the analysis of Hyperspectir data with pavement condition index (PCI) is carried out. The relationship between these two metrics is consistent for the good quality roads but declines for the road represented in a bad condition. As cracks are one of the strongest pavement distress features, they represent a conflict between the cracking results represented in PCI (negative values) and remote sensing signals (positive values). Although the ground resolution of Hyperspectir data is relatively high, it can still affect the final result of pavement condition. The reason is the mixture of different materials (e.g. aged pavement surface and fresh asphalt located in the thick cracks) represented in the spectral signatures.

(Herold & Roberts, 2005b) report about the spectral analysis of the aged and deteriorated pavement surfaces. They investigate the material properties of the asphalt road surface and their changes with respect to deterioration. They report about the components of the asphalt pavement surface which consist of aggregates (stones called by them as 'rocky components') and 'asphalt mix (hot mix or bitumen)'. The mineral characteristics of the aggregates depend on the geological area of the material extraction which can vary from one region to another. They state that the most common components of the aggregates are composed of  $\text{SiO}_2$ , CaO and MgO (Robl, et al., 1991). Asphalt mix as a complex material also varies in composition based on the source of raw oil and the process of refining. They mention that asphalt (bitumen) is a mixture of hydrocarbons consisting 50 to 1000 atoms of carbon plus sufficient oxygen, hydrogen, sulfur and nitrogen to provide the molecule with the polar nature. The chemical fundamentals of asphalt (bitumen) including their percentage are in this fashion: 'carbon (80%\_87%), hydrogen (9%\_11%), oxygen (2%\_8%), nitrogen (0%\_1%), sulfur (0.5%\_1%), and some trace metals' (Asphalt Institute, 1989) , (Cloutis, 1989). Figure 2 illustrates characteristics of the spectral reflectance of asphalt pavement surface based on its aging and damages. The spectral signatures are provided by ADS field spectrometer. Diagrams shows different road pavement conditions: A, asphalt aging and erosion; B, structural road damages (cracks); C, structural road damages (ravelling); D, pavement maintenance'. Diagram A shows the pure asphalt without any damage of the pavement surface. The pavement age, PCI and structure index (SI) are depicted together with pavement picture of each related spectral signature. The test area used in this diagram has been sealed with asphalt mix and generally the spectral reflectance is low which indicates the 'hydrocarbon constituents' rules the absorption conditions. The reflectance amounts to the minimum value near 350 nm and this value grows toward greater wavelengths. The main reason of such strong absorption is

because the hydrocarbon components perform electronic transitions which are originated from ‘excitation of bonding electrons’ in the ultraviolet (UV) and visible wavelength ranges. The strength of absorption decreases by increasing the wavelength values (Cloutis, 1989). They report that there are some clear ‘organic absorption’ features in SWIR wavelength range. ‘ Fundamental absorption bands include an aromatic C—H stretch, symmetric and asymmetric stretches and bends of CH<sub>3</sub> and CH<sub>2</sub> radicals, the carbonyl– carboxyl C—O stretch and aromatic carbon stretch, and numerous combinations and overtones‘ (Cloutis, 1989). Some absorption is represented near 1700 nm. Moreover, beyond 2200 nm there is a huge absorption located in ca. 2300 nm regions. Diagram B illustrates asphalt pavement surface cracking. The existence of cracks reduces the brightness in overall respective spectral signature. They mention that the cracking surfaces contain more hydrocarbon features in the 1700 nm and 2300 nm wavelength domains. The reason is the visibility of the lower layer of pavement surface which is full of fresh asphalt mix. Diagram C shows the aged asphalt pavement surface which is eroded and deteriorated. They state that with erosion of the bitumen, the pavement surface is less viscous and more likely to damage (e.g. having crack). The properties of SWIR hydrocarbon absorption near 1700 nm and 2300 nm disappear and are taken over by mineral absorptions. In Diagram D, spectrum I illustrates the area which is full of sealed cracks. Crack sealing prohibit extension and growing of the cracking area and does not let water penetrates into the lower layer of the pavement surface. The sealed cracks perform low reflectance of ca. 5%. Nevertheless some minor hydrocarbon absorption is shown by the spectral signature (Herold, et al., 2004). Spectrum J shows a clip of the pavement surface covered by fresh patch. The material used in patches is the same as in the new asphalt. Therefore, for this region, it is more probable to have similar spectral behaviour like in new asphalt spectrum.

## 2. Related studies in road condition survey: data capture and processing

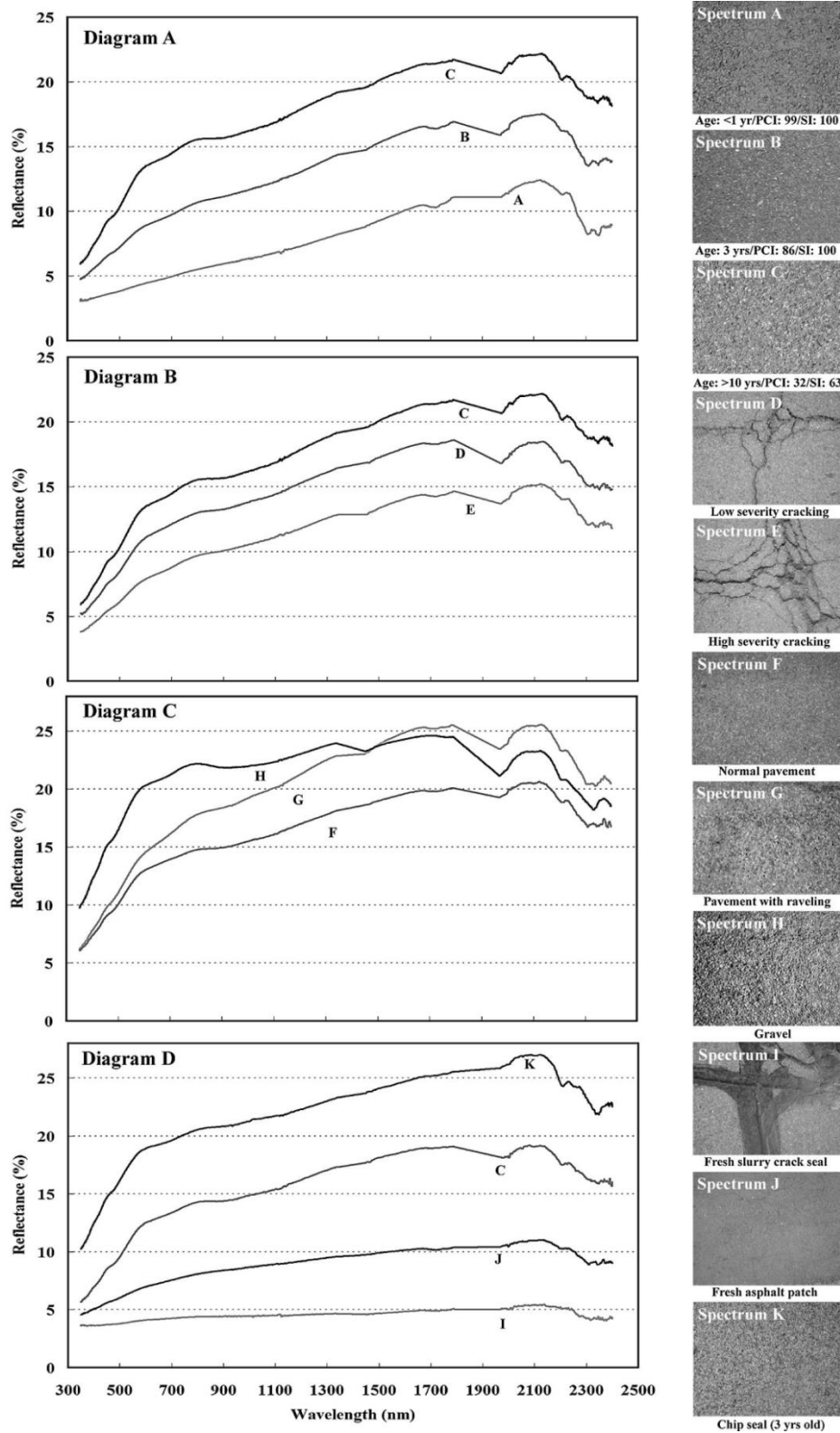


Figure 2. Characteristics of the spectral reflectance of asphalt pavement surface based on aging, diagrams with different road pavement conditions: 'A, asphalt aging and erosion; B, structural road damages (cracks); C, structural road damages (raveling); D, pavement maintenance' (Herold & Roberts, 2005b)

## 2.5. Other related techniques for monitoring asphalt pavements condition

(Heiden, et al., 2007) determine robust spectral features (SF) for identification of urban surface materials. They use SF for the automation of material identification in hyperspectral remote sensing data. They mention that because of the high variability of the spectral characteristics in the urban area, it is necessary to have spectral analysis derived from field measurement. The goal of their study is to develop a way which grants ‘the image-based derivation of material-specific spectral features that are robust against within-class variability and spectral overlap between classes of interest’. These features enable the automatic identification of endmembers in hyperspectral remote sensing. The study area is in Potsdam and Dresden in Germany with variety of urban structures. The hyperspectral data are collected in the different seasonal and annual by German Aerospace Center (DLR) using HyMap sensor. This sensor has captured the images data within 128 and 126 bands and covered visible near infra-red (VIS NIR) SWIR (I+II) ranges. Due to the low resolution of the HyMap data, the field spectrometry is essential. The spectral resolution performed by ASD field spectrometer is 3nm for the VIS and NIR and 10 nm for the SWIR range. They propose two steps for optimal determination of spectral features (SF). First for each individual material, the SF are represented. These SF perform the optimal recognition of the material and segregation of different substances. Adapting feature functions enable appropriate SF representation. In the second step, the reputability analysis is performed to examine the robustness of the selected SF. In order to test the consistency of the SF, the grey values are the second indication which compare the results derived from the SFs. Contrary to the SF which is applicable for the a certain wavelength range, the grey value is focused on only one band. In their study, following spectral features have been proposed: ‘1) absorption band, 2) reflectance peak, 3) increase and decrease of reflectance, 4) brightness and 5) continuity of a spectral curve’. The absorption band is the specific wavelength in which the lowest reflection occurs in a certain domain. Moreover, for spectral separation, they take some quantitative analysis into account. They mention that the regular quantitative techniques of the spectral data such as transformed divergence, Jeffries-Matusita and Bhattacharyya have two drawbacks: first it is not possible to have a quantitative interpretation of the computed values for an enhanced classification, secondly, these quantitative solutions are limited to only two classes. Inspired by these spectral features, in this dissertation, line slope as an empirical linear feature (described in section 4.7.1 and tested in section 7.1) is selected to inspect the training spectral signatures.

### **2.5. Other related techniques for monitoring asphalt pavements condition**

With ground penetration radar (GPR) and thermal imaging, two more sensors for monitoring asphalt pavement condition are only briefly addressed in the following. They will not be further considered in this research.

#### **2.5.1. Ground Penetrating Radar (GPR)**

GPR is a non-destructive and electro-magnetic solution which is employed for road inspection for more than a decade. It has several advantages like ‘high rate acquisition, quasi-continuous measurements’ which can monitor the road sublayers. However, still proper algorithms for significant road condition mapping are missing (Mahmoudzadeh, et al., 2013). (Mahmoudzadeh, et al., 2013) evaluate the full-wave radar model proposed by (Lambot, et al., 2004) to build up ‘underlying’

## 2. Related studies in road condition survey: data capture and processing

sublayers of road pavements. They employ two GPR systems namely: ‘stepped frequency and impulse GPR’. They made use of ‘farfield’ antennas and reported that the results of both GPR systems are similar. (Rial, et al., 2006) report about their experiences of integration of GPR and GPS, for road inspection. They employ a RAMAC GPR together with a GPS system (RTK XT SiRF Xtrax), and a video camera to capture the images along the test drive. Through GPS, the GPR recording and the video camera are geo-referenced. (Li, et al., 2016) investigate the automatic pothole detection using GPR and images. As GPR is very sensitive against the material changes, the pothole positions can be recognized by GPR. They illustrate the GPR signal patterns in different road conditions. They show that the GPR signal amplitude changes in pothole regions due to the material difference including air and soil in the pothole area compared to the neighbouring intact asphalt surface.

### 2.5.2. Thermal imaging

Moisture ingress might damage the road structure. It is possible to find the water ingress using mobile thermal infra-red imagery. If the water enters the road structure, it shall change the heating up/ cooling down procedure of the road layers. The road sections containing water certainly gain visibility in the thermal images. Identification of such areas in the geo-referenced thermal images simplifies time prediction of road rehabilitation (FLIR, 2016). Figure 3 shows two road sections with dissimilar pavement quality.

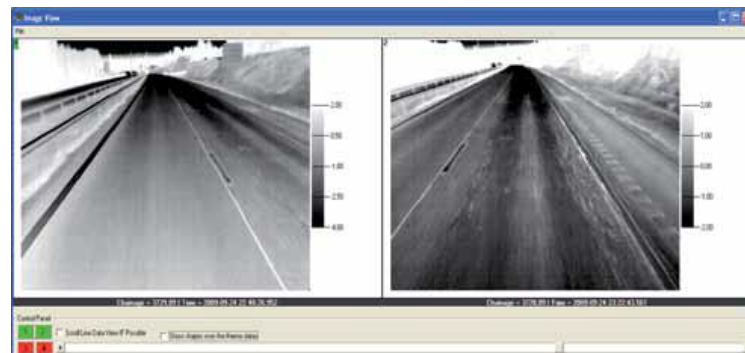


Figure 3. High quality pavement (left), poor quality pavement (right) shown in the thermal images (FLIR, 2016)

The left picture in Figure 3 shows a homogeneous thermal texture on the road while the right one indicates evidence of cracks and water which entered into the asphalt (FLIR, 2016). Taking advantage of thermal infra-red imagery is promising for road inspection.



### 3. Mobile mapping technology for multi-sensor based road condition mapping

#### 3.1. System design

In the experimental investigation of this dissertation, the following instruments are used for capturing road surfaces: laser scanner, RGB camera, spectrometer and GNSS/INS navigation system. The setup of the instruments is shown in Figure 4. The laser scanner, the RGB camera and the spectrometer can be synchronized with the GNSS/INS navigation system to geo-reference all three sensors simultaneously.

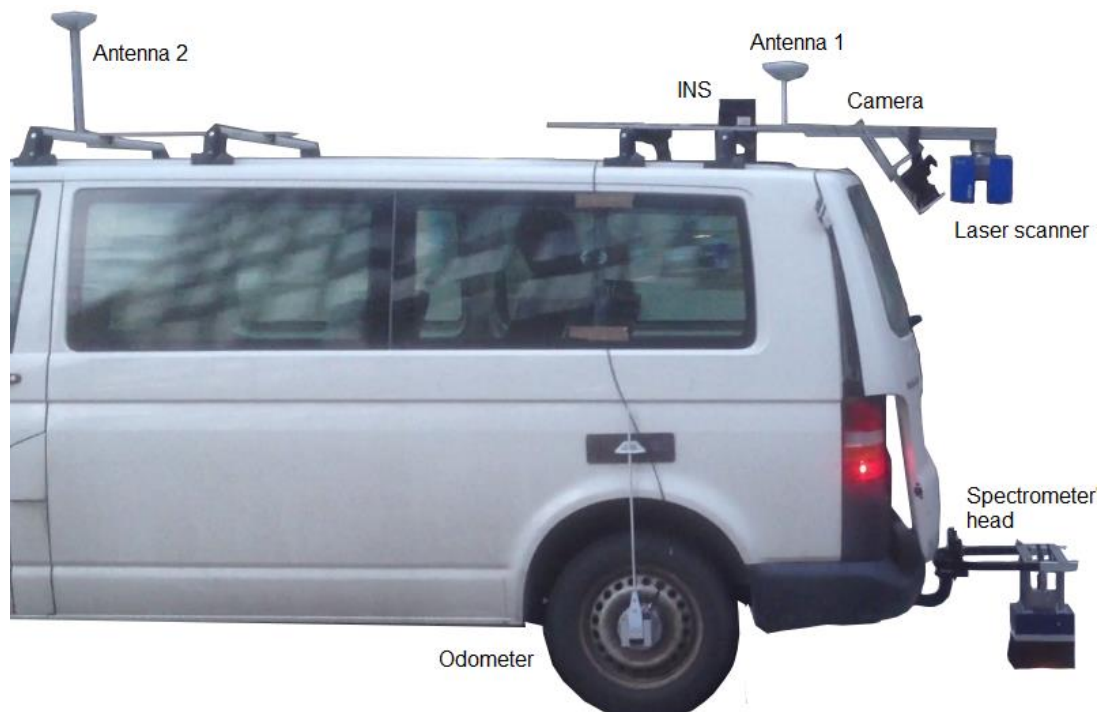


Figure 4. Setup of the mobile mapping system composed of laser scanner, RGB camera, spectrometer and GPS/INS system

#### 3.2. Laser scanning system

Two series of FARO laser scanners (Focus3D X 130 HDR, FARO Focus 3D X330) are used in this dissertation. The most used laser scanner is FARO Focus 3D X330 which is a light weight device (5.2 kg). The measuring principle of these laser scanners is based on phase-shift. According to (Faro, 2016), the range of Focus3D X 330 is from 0.6 m to 330 m, the measurement rate amounts up to 976 k measurements per second with ranging error of  $\pm 2$  mm. With a combination of two rotating elements, the terrestrial laser scanner is able to capture a 3D scene. The scanner motor rotates horizontally and the mirror motor rotates vertically. The vertical rotation is suitable for mobile

### 3. Mobile mapping technology for multi-sensor based road condition mapping

mapping. By connecting a “Helical adapter” at the bottom of the laser scanner, the horizontal rotation is locked and the laser scanner performs only vertical rotation. The vertical field of view of this laser scanner is 300° (Faro, 2013). Therefore, with the mounting arrangement shown in Figure 4, the profile above the laser scanner within 60° field of view will not be measured. While driving the car, the scanner captures the road surface line by line perpendicular to the driving direction. With this mounting arrangement, the laser scanner records points on the pavement surface with the highest resolution. With a driving speed of not more than 30 km/h, the distance between the laser scanning profiles is less than 9 cm (Miraliakbari, et al., 2014).

#### **3.3. RGB camera imaging**

The utilized camera is a Canon 5D Mark II which is a digital single-lens reflex with 21 megapixels. Using this camera, up to 3.9 frames per second can be recorded continuously. The large sensor size of  $36 \times 24 \text{ mm}^2$  ( $5616 \times 3744 \text{ px}$ ) records high resolution pictures (dpreview, 2016). The lens of the camera with focal length of 35 mm causes field of view (FOV) of 54.43° and 37.84° in horizontal and vertical directions. The mounting arrangement of the camera in oblique view (ca. 30°) (Miraliakbari, et al., 2014) (Miraliakbari & Hahn, 2014) enables bigger area coverage and prevents unnecessary recording at the back door of the vehicle van as shown in Figure 4. The arrangement is a compromise. Ideal would be vertically mounted high frequency camera which would require a cantilever arm. In experiments, the Canon 5D Mark II recorded images every 0.65 sec with the highest resolution ( $5616 \times 3744 \text{ px}$ ). The recording is controlled by a C++ program. The recording has two modes: time-based and distance-based recording. In time-based recording, the shooting time interval is constant for the whole track. In distance-based mode, the distance between two camera positions is defined. Hence, the latter avoids redundant image data acquisition especially when the vehicle is stationary. The images are stored in the memory card of the camera and are copied afterwards. As described in (Miraliakbari, et al., 2014) and (Miraliakbari & Hahn, 2014), for synchronization purposes, a camera output signal generated by the camera hot-shoe is transferred to GNSS/INS unit. This signal must be amplified to achieve the minimum voltage quantity which is required for GNSS/INS synchronization by the Applanix POS LV 420 system.

#### **3.4. Infra-red (IR) Spectrometry**

Spectrometry is a method or even a group of methods with many applications in physics and chemistry. In this study, the focus is on IR spectrometry. Spectrometry in IR domain deals with the radiation reflected from the materials and separates the radiation into the IR spectra. The spectra recorded by the spectrometers can cover visible, NIR and SWIR ranges depending on the spectrometer.

##### **3.4.1. Polytec spectrometer**

For the experiments, Polytec spectrometers are used. The Polytec spectrometers are composed of three different parts, namely: spectrometer box (Figure 5), sensor head (Figure 7) and fibre optic cable. The spectrometer box holds the Polychromator (Figure 6) known as the heart of the spectrometer (Polytec,

2013b). The connection between the spectrometer and the sensor head is conceivable via fibre optic cable. Fibre optic cables own larger bandwidth compared to the normal metal cables. The data transfer with these cables is securer than with the metal cables and the data can be digitally transmitted by the fibre cables which can be compatible for the computer (Webopedia, 2013).

Polytec spectrometer generates a light via light source which is located inside the spectrometer head. Materials behave differently against the incoming light. If an incoming light hits the surface of the material and reflects, the value of reflectance (or absorption) in some specific bands provides a reasonable interpretation about the material property (Polytec, 2011a).



Figure 5. Spectrometer box containing polychromator (Polytec, 2011a)

The incoming light is coupled into the polychromator by means of Sub Miniature version A (SMA) fibre optic connector (Polytec, 2011a). The SMA is a fibre optic connector developed by Amphenol Fiber Optic Products (Timbercon, 2013). The light passes through the entrance slit and is delivered to the achromatic lens. At the transmission grating, the light will be fractionalized into the spectral particles. Last but not least, the rear lens system creates an image on the detector (Polytec, 2011a).

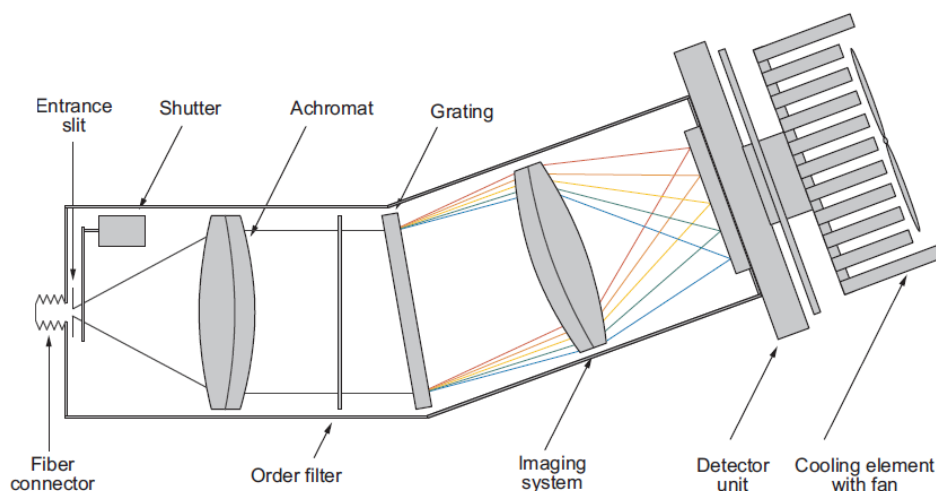


Figure 6. Polychromator (Polytec, 2011a)

### 3. Mobile mapping technology for multi-sensor based road condition mapping

As shown in Figure 6, the detector which is at the end of the polychromator, is a linear configuration of the pixels (diodes), charged with the light at the different wavelengths. Depending on the spectral resolution defined in the spectrometer, each pixel belongs to the special wavelength and the incoming light with a certain wavelength will be read out by the corresponding pixel. A high-pass filter prevents the incoming spectrum from higher diffractions orders. Dark spectrum: because of the thermal electrons, some blatant dark signals will be generated even though there might be no incoming radiation. The dark signal belongs to each individual pixel which is slightly different from each other. It is highly recommended by the manufacturer to always repeatedly update the dark spectrum in each application (Polytec, 2011a).

Table 2 characterized various spectrometers with respect to their wavelength ranges, pixels and resolutions.

Model	Range	Pixel	Resolution
PSS 1050	550-1050 nm	512	<3.6 nm or <5.4 nm
PSS 1720	850-1650 nm	256	<6.4 nm or <9.5 nm
PSS 2120	1100-2100 nm	256	<7.9 nm or <11.9 nm
PSS 2220	1200-2200 nm	256	<7.9 nm or <11.9 nm
PSS 2221	1253-2259 nm	256	<7.9 nm or <11.9 nm
PSS 2520	1300-2500 nm	256	<9.5 nm or <14.2 nm

Table 2. Characterization of different spectrometer models offered by Polytec company (Polytec, 2013a), the PSS 2221 used in this research is a subversion of PSS 2220 and added for completeness

As shown in the table, apart from PSS 1050 which records the reflectivity values in the VIS NIR range, the rest of the spectrometers have 256 pixels (diodes) in their polychromators. They record the reflectivity values in the NIR and SWIR ranges. The resolution of each pixel varies from 3.6 nm to 14.2 nm depending on the type of the spectrometer. As discussed in section 2.4, the most suitable spectrometer is the one which records the reflectivity values beyond 2000 nm. Therefore, PSS 2520 is the best option to be used but due to the technical problems of this spectrometer, PSS 2221 was selected which covers to 2259 nm. As mentioned in (Miraliakbari, et al., 2014), this spectrometer includes 256 adjacent channels within the wavelength range of 1253 nm to 2259 nm. With the width of 1006 nm and the number of 256 pixels, the sampling distance amounts to ca. 4 nm. With the spectral resolution of 8 nm to 12 nm, the neighboring bands overlap significantly. The reflectivity is derived as the fraction of the registered and the emitted intensity.

The spectrometer head is an optional measurement accessory connected to the fibre optic cable. The lightening is enforced by a '20W tungsten-halogen light source' (Polytec, 2013c) which is integrated into the cover of spectrometer head. Using this self-illumination makes field operation independent from the sunlight. Moreover an internal reference panel is integrated in the spectrometer's head. This internal referencing is automatically executed for the white balance of the spectrometer (Polytec, 2011b). The spectrometry head used in this study is called 'Conveyor belt sensor head' The proposed operation distance between of the sensor head to the material surface (measurement target) is between ca. 10.0 to 60.0 cm, (Polytec, 2011b).



Figure 7. Spectrometer head, 'Conveyor belt sensor head' (Polytec, 2011b)

### Mobile spectrometry

For mobile spectrometry, the spectrometer head is mounted at the backside of the vehicle van with the help of a bicycle carrier, shown in Figure 4 and Figure 8, in order to keep the distance between the pavement surface and the sensor to appropriately 30 cm to 50 cm. A set of soft bristles (Figure 8) was constructed in order to insulate the spectrometer head from external illumination sources. Thus, the spectrometer only registers the light which is emitted by the tungsten-halogen light source. Contrary to the hyperspectral cameras, the spectrometer records data on the spot. Hence, the recording will be carried out only along the longitudinal profiles (Miraliakbari, et al., 2014). The spectrometer head is connected to the spectrometer box via the fibre optic cable. This cable is very tender so it is covered by a thick elastic barrel during driving.



Figure 8. Spectrometer head front view

### 3.4.2. Hand-held (Spectral Evolution) spectrometer

Apart from mobile spectrometry, several other measurements are carried out using the handheld PSR+ 3500 Spectroradiometer (Spectral Evolution, 2012). The reason of these additional measurements is to investigate an extended spectral range of 350 nm to 2500 nm which is covered by this spectrometer.

### 3. Mobile mapping technology for multi-sensor based road condition mapping



Figure 9. Hand-held 'PSR+ 3500 Spectroradiometer' (Spectral Evolution PSR+ 3500, 2012)

Some of the specifications of PSR+ 3500 Spectroradiometer are as follows. According to (Spectral Evolution PSR+ 3500, 2012) the system cooling of PSR+ 3500 has been upgraded 'with the new unibody anodized aluminium chassis with integral heat dispersion channels.' The spectral resolution of these spectrometers varies depending on the wavelength domain: 3 nm at 700 nm, 8 nm at 1500 nm and 6 nm at 2100 nm. There are two illumination possibilities for this spectrometer: first using self-illumination by contact probe and secondly using sunlight. For self-illumination, a direct contact to the surface material is necessary to avoid external illumination sources.

#### **3.5. Geo-referencing, synchronization of the measurement devices with GNSS/INS**

The GNSS/INS system used in the experimental investigation is the Applanix position and orientation system POS LV 420 (Applanix, 2015). An essential part of system integration is the synchronization between GNSS/INS system and other sensors. The synchronization serves for the geo-referencing of data captured by laser scanning, RGB imaging and spectrometry. The connection between the laser scanner and the GNSS/INS system is applied by the digital I/O connector and test box of the FARO laser scanner. The FARO laser scanner generates the TTL output signal in every scanning rotation. The laser scanner sends the output pulse to the GNSS/INS unit. The position and orientation parameters for each scanning rotation are used for further point cloud geo-referencing. Similar is the synchronization for the RGB camera and the spectrometer and the generated output pulses are sent to the navigation device. For simplification, it is assumed that the spots measured by the spectrometer are exactly below the spectrometer position at the road surface. Few degrees of deviation of the spectrometer from the vertical direction will not lead to a large horizontal displacement at the 30 cm measurement distance. After geo-referencing the spectrometry data, the spectral spots can be visualized on the images. Moreover, it is possible to overlay the RGB images together with the position of the spectral spots on the geo-referenced mobile laser scanning data.

Mobile mapping systems with camera(s), laser scanner(s), navigation units and a vehicle are commercially available and mature. Nevertheless, for this research, the mobile mapping system is assembled using the mentioned sensors only. This allows to flexibly set up the system or replace components if necessary.

### 3.6. Study area and datasets

The laser scanning test dataset is used to separate the pavement surface from its neighbourhood and to detect the ruts. It covers ca. 1.5 km network of streets which are in the vicinity of University of Applied Sciences Stuttgart. The study area (datasets A and B in Table 3) is composed of small and main streets including bikeways, pedestrian area, parking places and low-height curbstones (Miraliakbari, et al., 2015). Due to the limited number of potholes in this dataset, extra test drives have been carried out to select pothole regions.

Dataset	Average of longitudinal point distance [m]	Average of transverse point distance [m]
A	0.05	0.0025
B	0.04	0.004

Table 3. Average of longitudinal and transverse point distance of the dataset (Miraliakbari, et al., 2015)

For pavement crack and path detection, several images are taken from streets of Stuttgart and Ludwigsburg in Germany with a variety of different road distresses such as cracks and patches. These images are geo-referenced either using position and orientation information of the captured images received from GNSS/INS data or by ortho-image generation by employing PhotoScan (Agisoft PhotoScan, 2016) software. During the test drives, position and orientation of the camera (X, Y, Z, roll, pitch and yaw) at the time of each exposure is available due to the synchronization between GNSS/INS system and camera. These position and orientation values, are used for geo-referencing the photos. The offset ( $\Delta X$ ,  $\Delta Y$  and  $\Delta Z$ ) between the centre of camera and the GNSS/INS unit is measured and considered to obtain the coordinate of camera projection centre. The images are transformed to the planar surface based on projective geometry and a stream of geocoded rectified images can therefore be represented as a mosaic.

A more precise way to generate an ortho-rectified mosaic is to employ PhotoScan software. Image matching, bundle adjustment of an image block, dense point cloud and ortho-image generation can be carried out with or without using the position and orientation parameters of the image. Well identifiable points are selected from the mobile laser scanning point clouds, and used as ground control points. Figure 10 shows a mosaic of a stream of RGB images generated by PhotoScan.

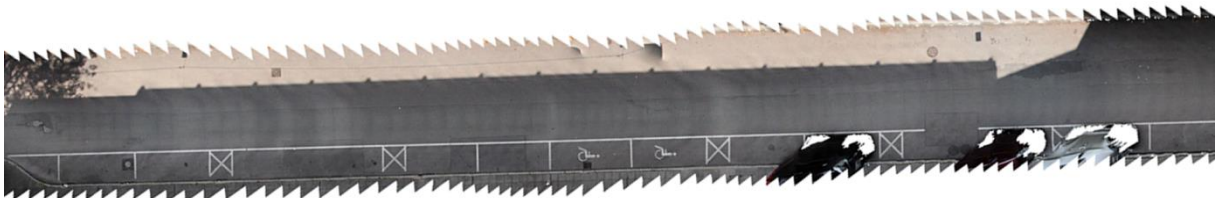


Figure 10. Mosaic of a stream of RGB images generated by PhotoScan

For the experimental investigations of the material properties of the road surface, three spectrometers are utilized, namely: Polytec (section 3.4.1), FieldSpec 4 Standard-Res Spectroradiometer ASD (Asdi, 2017) (with minor usage) and Spectral Evolution (section 3.4.2) spectrometers. Due to the restricted



### 3. Mobile mapping technology for multi-sensor based road condition mapping

wavelength range of the Polytec (1253 nm to 2259), two other spectrometers are additionally used. Apart from several training data collection, ca. 14300 spectrometry spots as evaluation data are recorded from the pavement surfaces located in the vicinity of Stuttgart University of Applied Sciences. Polytec spectrometer is used for this evaluation data collection.



## 4. Concept of road distress detection and deterioration analysis

### 4.1. Introduction

In this chapter, the concept and novel contributions of the dissertation for road condition mapping are presented. The data captured by laser scanner, RGB camera and spectrometer are utilized for distress detection and asphalt quality investigation. Laser scanning data are employed to detect ruts and potholes. Cracks and patches are extracted using RGB images. Investigations on pavement material property are carried out using spectrometry data. This leads to the concept of road condition mapping shown in Figure 11. Each task is solved with data captured by one of the instruments. The RGB images are furthermore used to visualize the pavement surface and to contribute to the evaluation of the results of spectrometric analysis. A preliminary version of the conceptual approach for road condition mapping is presented in (Miraliakbari, et al., 2014).

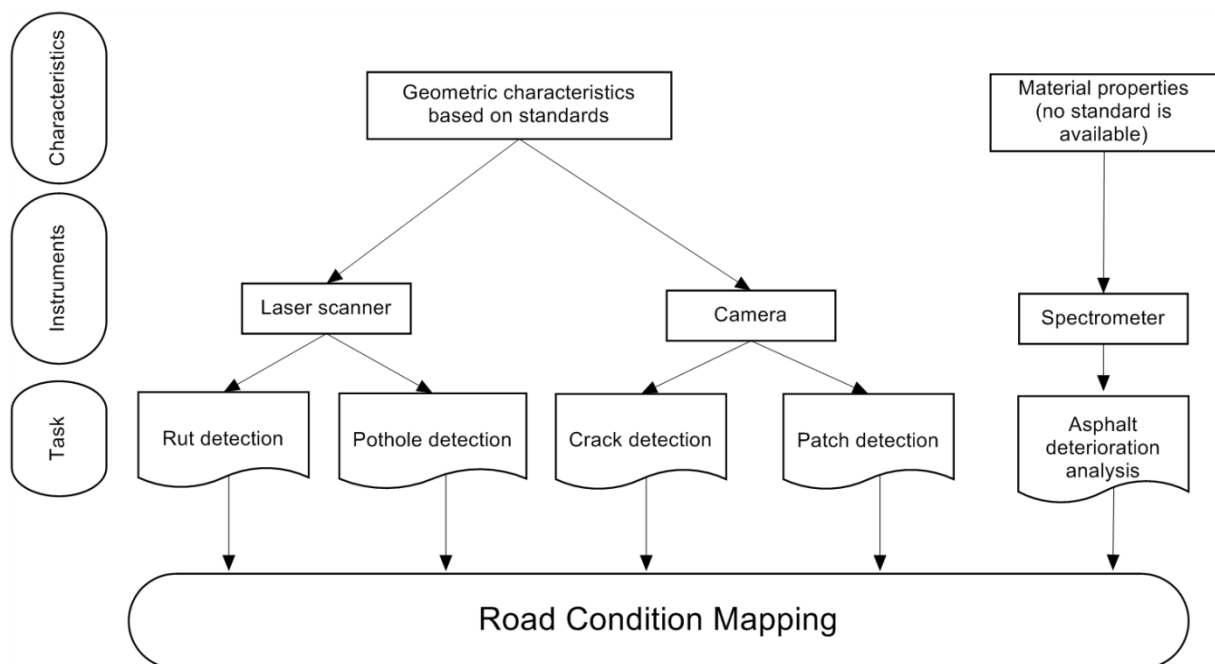


Figure 11. Concept of the road condition mapping, modified from (Miraliakbari, et al., 2014)

### 4.2. Road surface and boundary extraction

The extraction of the road surface is the preparatory step for rut and pothole detection. Inputs to the extraction process are the point clouds of road corridors that include the road surface in detail. Road surface extraction separates the pavement surface from the neighbouring objects such as curbstones, pedestrian area and building facades. ‘Height jump’ and ‘slope change’ at the boundary of pavement surface and curbstones are two common criteria for pavement surface extraction. Generally, the height of a curbstone varies from 100 mm to 200 mm (Wikipedia, 2017). Along public roads, there are frequently exceptions like those, for instance, shown in Figure 12. The lowered curbstone on the left side of the road segment eases the entrance into a car park. The height of this curbstone is ca. 3 cm (Miraliakbari, et al., 2015).

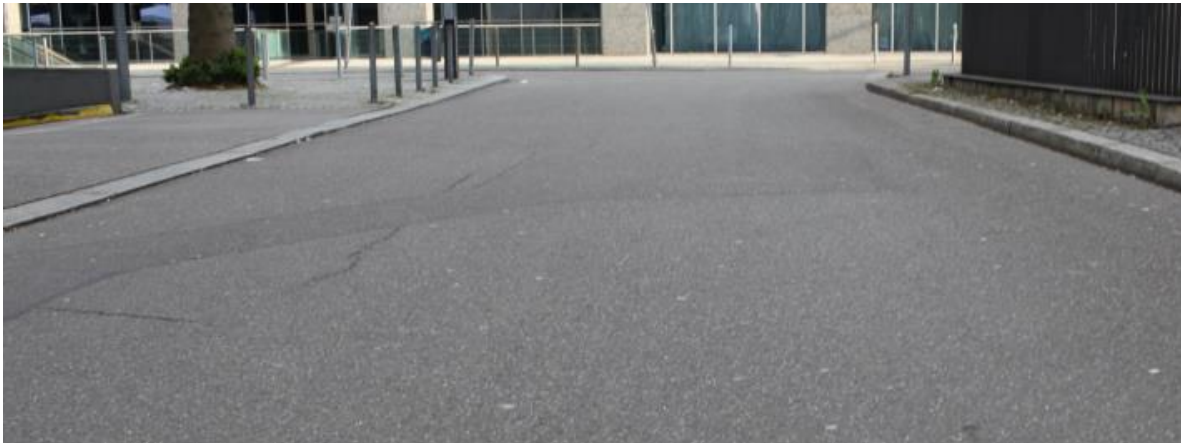


Figure 12. An example of a low curbstone on the left side of the photographed road (Miraliakbari, et al., 2015)

For the development of an automatic procedure for extracting the road surface from geo-referenced mobile laser scanning data, it is assumed that the street floor is smooth and bounded by curbstones. Based on the assumption that the height jumps coincide with the border of the pavement surface (i.e. curbstone edges) two variants are suggested, namely: height difference-based (HDB) and histogram-based (HB) height jump detection. By region growing applied to the irregular point cloud, the road surface is extracted. For processing, the recorded point cloud is divided into equidistant segments e.g. 2 m along the trajectory. The height jump serves as stop criterion for the region growing. The curbstone edges are extracted using splines in order to define the boundaries of the road (Miraliakbari, et al., 2015).

The height jump criterion might not always lead to the road border. For instance, junctions of bikeways and roads mostly have a smooth transition. Similar is the situation in front of the park places and garages. In these cases, bikeways and sidewalks might be wrongly detected as road pavement surface, because the region growing stops only at height jumps. Obstacles on the road such as car wheels lead to incorrect detection of road boundaries. To eliminate these errors, the detected height jumps caused by objects on the road must be filtered out (Miraliakbari, et al., 2015).

### 4.2.1. Principle of height jump detection

For calculating local features of the point cloud, a 2D horizontal grid is used to divide the point cloud into cells. A cell is defined by a vertical cylinder or cuboid and is related to each grid point. Local features are defined by functions which consider the vertical point distribution. Two variants are evaluated to identify if the neighbourhood contains a height jump. They are discussed as follows (Miraliakbari, et al., 2015):

#### Height difference-based (HDB)

The target function of this variant considers the maximum height difference of all points of a cell defined by a vertical cylinder. A cell is considered as road surface boundary if the difference between the maximum and minimum height exceed a certain threshold. Figure 13 illustrates the HDB criterion. The target function is:

$$f(h) = \max(h) - \min(h) \quad (1)$$

where,  $h$  denotes the heights of all laser scanning points located in the cylinder (Miraliakbari, et al., 2015).

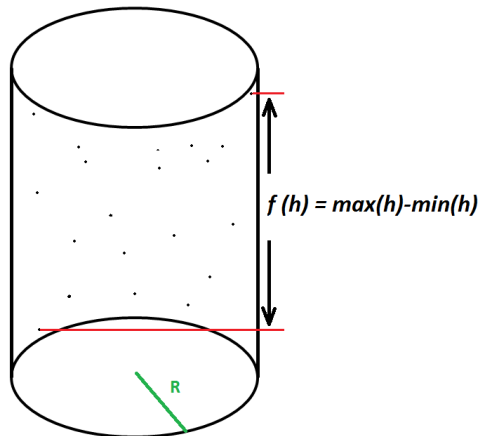


Figure 13. Sketch of the HDB variant

#### Histogram-based (HB)

In this variant, voxels are used instead of the cylinders for defining the cell. In HB variant, the height of the cuboid represents the minimum curbstone height (threshold). The point distance on the road surface is not equal along and across the driving direction. Therefore, the width and the length of a voxel may adapt to the distance interval of the point cloud along longitudinal and transverse directions. For the HB variant the following algorithm is implemented (Miraliakbari, et al., 2015):

#### 4. Concept of road distress detection and deterioration analysis

- A. Use the equidistant road segments
- B. Voxelize the road segments into cells: The lengths of voxel edges are empirically set to, for example:  $dx_v = 10$  cm,  $dy_v = 5$  cm,  $dz_v = 2$  cm
- C. Label the voxel by considering empty voxels as zero and filled (containing laser points) voxels as one
- D. Sum the binary values of the voxels for each cell. This feature characterizes the cell.

Steps C and D are repeated for all cells of a road segment which results in a feature image.

- E. Classify the feature image into three classes as follows:

Class zero: if the feature value is zero

Class one: if the feature value is exactly one

Class two: if the feature value is more than one (potential curbstone pixels)

In this variant the region growing, which is explained in the next section, will be terminated if a cell belongs to “Class zero” and will be continued if a cell belongs to “Class one”. For cells belonging to “Class two”: a) if there is no empty voxels between the filled voxels the region growing will be terminated, b) if one or more than one empty voxel are located between the filled voxels, the region growing continues. This constraint lets the point clouds below the car doors to be extracted as road surface and allows separating, in particular, car bumpers or car doors from curbstones. Figure 14 illustrates the HB variant. In this example, one of the four voxels is an empty voxel. The corresponding cell belongs to ‘Class two’ but the explained constraint avoids associating the cell with the curbstone position (Miraliakbari, et al., 2015).

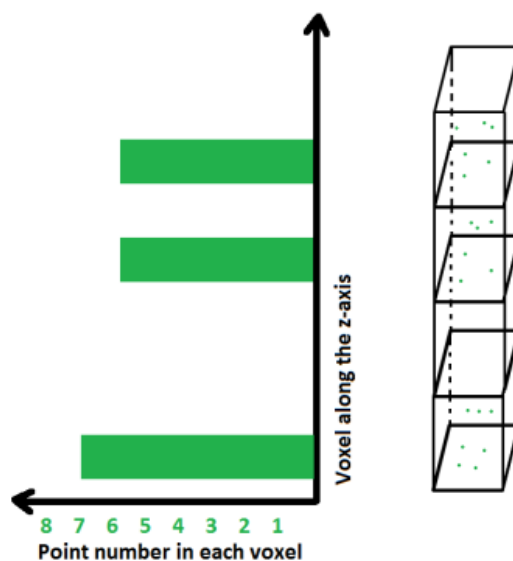


Figure 14. Sketch of HB variant illustrates a cell with four voxels that are placed on top of each other (Miraliakbari, et al., 2015)

### 4.2.2. Region growing

The horizontal coordinates of the laser scanner trajectory are used to define the location of seed points. Region growing starts from the seed points which are in the vicinity this location on the road surface. Region growing in two dimensions uses a four-neighbourhood, in one dimension a one-neighbourhood (Miraliakbari, et al., 2015):

#### Four-neighbourhood

This region growing proceeds in four sides (left, right, top and bottom) of the seed points (Figure 15 left) and continues as long as the criteria of both HDB and HB variants are applicable.

#### One-neighbourhood

One-neighbourhood region growing proceeds only in one direction which is perpendicular to the laser scanner trajectory (Figure 15 right). This region growing is faster and not susceptible to a weakness of four-neighbourhood region growing, where a sidewalk will be detected wrongly as street floor if there is a low curbstone in the segment.

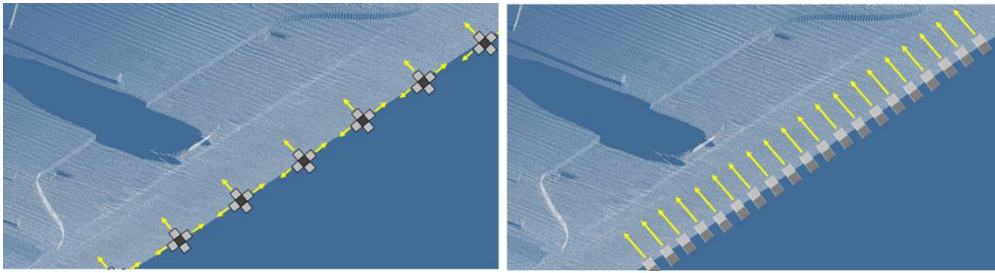


Figure 15. Schematic representation of four-neighbourhood (left), one-neighbourhood (right) region growing

### 4.2.3. Road boundary extraction

Road boundary extraction is a secondary result of road pavement surface extraction. Potential road boundaries are the boundaries of extracted road surface. Due to the existence of obstacles such as parked cars, possible termination of region growing inside the road (gaps) and overshoot regions the potential road boundary cells may not always locate at the curbstones and can include outliers (Miraliakbari, et al., 2015). In order to remove the outliers, the geometric properties of area and roundness are used. Roundness is defined as:

$$Roundness = \frac{4\pi A}{P^2} \quad (2)$$

where  $A$  is the area and  $P$  is the perimeter of the potential road boundary region. The road boundary regions have a larger area and a lower roundness than the outliers (e.g. car wheels) therefore, non-crack regions are eliminated if  $A < A_{min}$  and  $Roundness > Roundness_{min}$ .

#### 4. Concept of road distress detection and deterioration analysis

Obstacles such as cars and low curbstones decrease the chance of complete road border extraction because they cause gap in the potential road boundaries. Hence, after filtering the potential road boundary regions, it is essential to fill the gaps by connecting detected curbstone edges using spline fitting (Miraliakbari, et al., 2015).

### 4.3. Rut detection

Three methods are proposed for rut detection based on: 1D polynomial fitting, 1D cross-correlation and curvature estimation. In the experimental investigations, the three methods are compared to identify the most successful one.

#### 4.3.1. Rut detection using 1D polynomial fitting on the scanlines

The idea of (Laurent, et al., 1997) to approximate the road profile by a polygon and determine the rut depth by analysing the distance between road profile and the polygon (see section 2.2.2) is developed further using polynomial fitting. The middle of rut has lower height compared to the intact asphalt surface located in the vicinity of the rutting area. This geometric property is used to detect the ruts by means of polynomial fitting.

A 1D polynomial is fitted on the profile of each laser scanner line in an iterative process so that at the end of the process, all laser scanning points are below the polynomial except rut support segments which are connected to the polynomial. The result of polynomial approximation resembles to some extent the traditional way of rut detection. In traditional rut depth measurement, a long straight edge is laid along the road cross section where the rutting appears. The largest rut depth is mostly middle of the arc (Miraliakbari, et al., 2014).

In a first step, the scanlines are separated from each other and interpolated with a constant point distance interval. The distance interval is calculated based on the average point distance of the whole laser scanning profile of the road surface. The following iterative algorithm is proposed for a polynomial fitting on the scanline profile with the goal that the polynomial approximates the profile from above:

A) Approximate the scanline profile by a polynomial using least squares adjustment

As an example, a 1D polynomial of 3<sup>rd</sup> order is used. By taking all points of a scan line into account, this leads to:

$$z = a_0 + a_1x + a_2x^2 + a_3x^3 \quad (3)$$

$$\begin{bmatrix} z_1 \\ z_2 \\ \cdot \\ \cdot \\ \cdot \\ z_n \end{bmatrix} = \begin{bmatrix} 1 & x_1 & x_1^2 & x_1^3 \\ 1 & x_2 & x_2^2 & x_2^3 \\ & & \cdot & \\ & & \cdot & \\ & & \cdot & \\ 1 & x_n & x_n^2 & x_n^3 \end{bmatrix} \begin{bmatrix} a_0 \\ a_1 \\ a_2 \\ a_3 \end{bmatrix} \quad (4)$$

Here  $n$  is the number of points of the scanline interpolated at locations  $x_i$ ,  $a_i$  denotes a polynomial coefficient and  $z_i$  represents the height value at the  $i^{th}$  point. The coefficients are estimated using linear least squares adjustment:

$$\hat{a} = (A^T A)^{-1} A^T Z \quad (5)$$

where  $\hat{a}$  denotes the estimated coefficients,  $A$  is the design matrix and  $Z$  represents the vector of the scanline heights.

- B) Subtract the scanline heights from the corresponding heights of the approximating polynomial. The subtraction result contains both negative and positive height values.
- C) Generate a new scanline in such a way that for each location  $x_i$ , the greater height of either the original scanline or the approximating polynomial is selected.

That means, parts of the original scanline which are higher than the approximating polynomial are retained and parts which are located below are replaced by the approximating polynomial.

- D) Iterate the steps B and C (Figure 16) until the number of scanline points above the approximating polynomial is less than a certain threshold e.g. 1% of  $n$ .

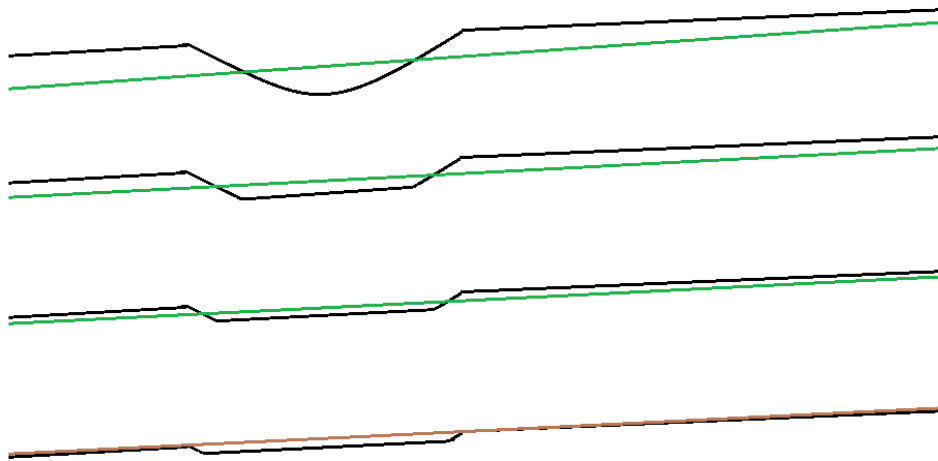


Figure 16. Schematic diagram of the iterative polynomial fitting on the laser scanning profile containing a rut

The processing result obtained for a scanline profile of 6.2 m width is shown in Figure 17. It was found that high order polynomials approximate the top of the scanline very well. Together with the huge number of scanline points step C) of the algorithm ensures that the result is not affected by the typical artefacts of a high order polynomial.

#### 4. Concept of road distress detection and deterioration analysis

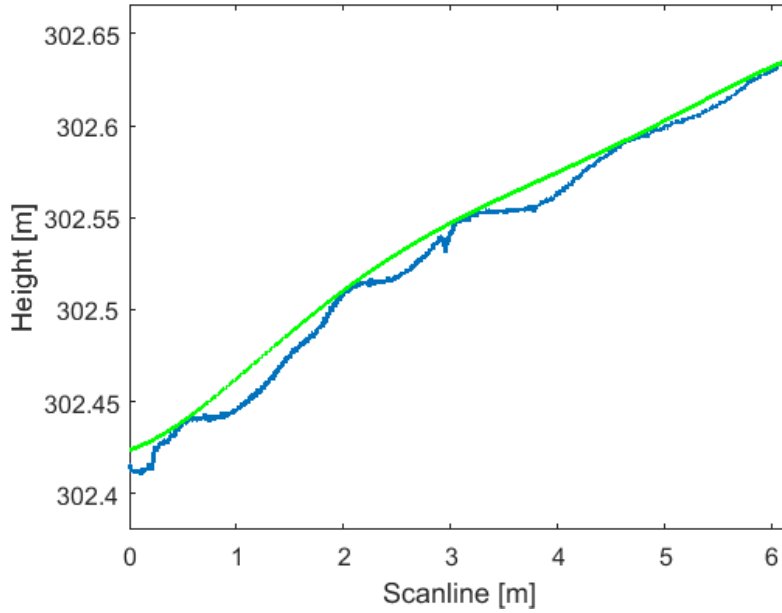


Figure 17. 6<sup>th</sup> order polynomial (green) fitted on top of the scanline profile (blue)

#### 4.3.2. Rut detection using 1D cross-correlation

Arc-shaped segments along the laser scanning profiles indicate ruts if they have sufficient depth. Segments with low depth may evolve to ruts in future. Such segments are categorized as potential ruts. For the detection of ruts 1D cross-correlation can be applied for each scanline. The correlation is carried out using a template which represents an idealized rut shape (Miraliakbari, et al., 2014). The template matching can be performed either on original profiles or on the difference between the original profile and the fitted polynomial. As described in (Miraliakbari, et al., 2014), according to (Leese, et al., 1971) or (Barnea & Silverman, 1972) the normalized correlation coefficient  $P(x)$  is calculated as follows:

$$P(x) = \frac{\sum_{i=-N/2}^{N/2} (f(x+i) - \bar{f}(x))(H(i) - \bar{H})}{(\sum_{i=-N/2}^{N/2} (f(x+i) - \bar{f}(x))^2 \sum_{i=-N/2}^{N/2} (H(i) - \bar{H})^2)^{1/2}} \quad (6)$$

where  $\bar{f}(x) = \sum_{i=-N/2}^{N/2} f(x+i)$  denotes the mean height of the  $N+1$  laser scanning points centred at  $x$  and  $\bar{H} = \sum_{i=-N/2}^{N/2} H(i)$  is the template mean height value. Correlation along the scanline leads to several local maxima which indicate possible potential rut locations and centre of the existing ruts. If the value of a local maximum is higher than a certain threshold, the location of this peak determines the actual rut position (mostly middle of the rut) within the profile of the scanline. The template is defined as a concave half ellipse with two adjacent horizontal line segments. The width of the template must resemble the typical width of ruts on roads. Because of normalization in Eq. (6), the height of the template is of minor importance.



Figure 18 represents the 1D cross-correlation of the template along the profile of height difference between the scanline and fitted polynomial of 6th order shown in Figure 17. The red curve represents the cross-correlation result overlaid on the profile.

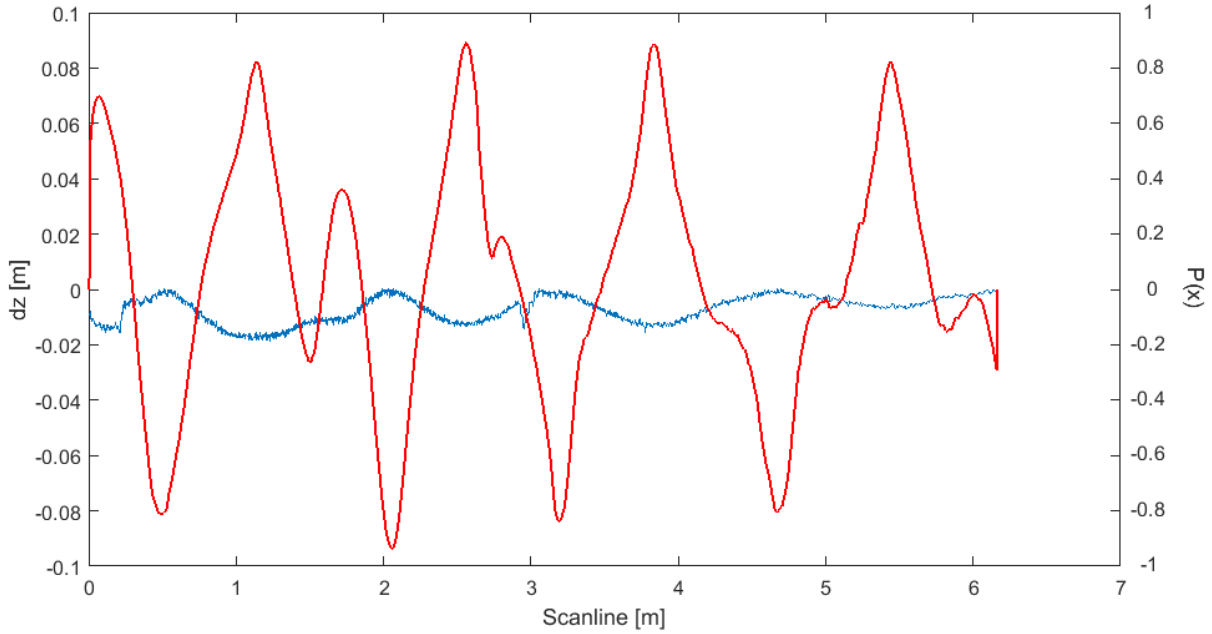


Figure 18. Exemplary graphic representation of a 1D cross-correlation (red curve) of the template along the residual profile (blue curve)

### 4.3.3. Rut detection using curvature

Calculation of local curvature is another method to localize the rut locations. The formula of curvature is as follows:

$$k = \frac{Z''}{(1 + Z'^2)^{3/2}} \quad (7)$$

where  $k$  is the curvature, and  $Z''$  and  $Z'$  are the first and second derivative of height with respect to the distance. Because the decimal value of the denominator amounts a small number,  $k$  is approximated as:  $k \approx Z''$ . For the calculation of curvature, every scanline is taken into account separately. With the assumption that scanline is parallel to the X-axis, the general formula of a parabola is as follows:

$$Z = aX^2 + bX + c \quad (8)$$

$$\begin{bmatrix} Z_1 \\ Z_2 \\ \cdot \\ \cdot \\ Z_n \end{bmatrix} = \begin{bmatrix} X_1^2 & X_1 1 \\ X_2^2 & X_2 1 \\ \cdot & \cdot \\ \cdot & \cdot \\ X_n^2 & X_n 1 \end{bmatrix} \begin{bmatrix} a \\ b \\ c \end{bmatrix} \quad (9)$$

#### 4. Concept of road distress detection and deterioration analysis

Here  $n$  is the number of points of the parabola on the scanline interpolated at locations  $x_i$ ,  $a$ ,  $b$  and  $c$  denote parabola coefficients and  $Z_i$  represents the height value at the  $i^{th}$  point. The coefficients are estimated using linear least squares adjustment:

$$\hat{a} = (A^T A)^{-1} A^T Z \quad (10)$$

and  $k$  is estimated respectively:

$$k \approx Z'' = 2a \quad (11)$$

As ruts have more curvature compared to the intact flat asphalt surface, after estimating curvature for each point on the scanline, threshold is used to localize the rut locations. This threshold is based on the cross section of the rut which has a certain depth, ( $Z_0$ ) and width ( $X_0$ ) and displays a parabola  $Z = (4Z_0/X_0^2)X^2$ . According to Eq. ( 11 ) the corresponding threshold is shown as follows:

$$k_{thresh} = 8Z_0/X_0^2 \quad (12)$$

### 4.4. Pothole detection

Potholes can be detected either using images or by laser scanning data. In this dissertation pothole detection is carried out by analysing the laser scanning point cloud. Two methods are employed for pothole detection namely: geodesic image reconstruction and polynomial fitting. This procedure of pothole detection is sketched in the master thesis of (Negussie, 2015).

#### 4.4.1. Pothole detection using geodesic morphological reconstruction

Morphological reconstruction obtained by iterating grey scale geodesic dilations was first proposed by (Vincent, 1993). He mentioned that ‘Morphological reconstruction is part of a set of image operators often referred to as geodesic.’ It has been used for laser data processing by (Arefi, 2009).

Grey scale geodesic distance-based morphological reconstruction particularly deals with two input images: mask  $I$  (original image) and marker  $J$  which has the same size of the mask and its grey values are those of mask plus or minus a certain offset  $g_{off}$  (Vincent, 1993) & (Arefi, 2009). The reconstruction is carried out by geodesic dilation or erosion. For applying morphological reconstruction by geodesic dilation, the marker can be defined by subtracting the offset from the mask ( $J = I - g_{off}$ ). In geodesic dilation, the marker image is dilated by an ‘elementary isotropic structuring elements’. The dilated marker will remain under the mask. This step of reconstruction is called elementary geodesic dilation (Vincent, 1993). The formula of the geodesic dilation of size one is given by:

$$\delta_I^{(1)} = (J \oplus B) \wedge I \quad (13)$$

where  $I$  and  $J$  denote mask and marker,  $\wedge$  ‘stands for piecewise minimum between the dilated marker and the mask image’  $J \oplus B$  is the dilation of marker by the elementary isotropic structuring element  $B$  (Serra, 1982), (Serra, 1988). The formula denotes that the geodesic dilation of size one is the new image reconstructed by computing the dilation of  $J$  by  $B$  and furthermore, selecting the minimum between the dilation result and  $I$  at each point of the mask (Arefi, 2009). By iterating the geodesic dilation process, the result is a grey scale geodesic dilation of size  $n \geq 0$  given by (Vincent, 1993):

$$\delta_I^{(n)}(J) = \underbrace{\delta_I^{(1)} \circ \delta_I^{(1)} \circ \delta_I^{(1)} \dots \delta_I^{(1)}}_{n \text{ times}}(J) \quad (14)$$

In order to limit the influence of the boundary of an image on the reconstruction result, (Arefi, 2009) suggested to link the grey value of the mask with the marker in the boundary pixels.

(Negussie, 2015) investigated pothole detection using geodesic morphological reconstruction. For pothole detection using geodesic morphological reconstruction, first the road section which contains the pothole is interpolated into a height raster. As in this study geodesic dilation is utilized, complement of the height raster is considered as mask (Figure 19 right) so that the cross section of the pothole region performs a convex shape (blue curve in Figure 20 (a)). The marker is generated by subtracting  $g_{\text{off}}$  from the mask (red curve in Figure 20 (b)). The green curve illustrated in subfigure (b) shows the reconstruction result. The outcome of  $dz = z_{\text{mask}} - z_{\text{reconstruction}}$  is illustrated in subfigure c. By applying a certain threshold to this black curve, e.g. 0.5 cm, pothole region will be extracted.

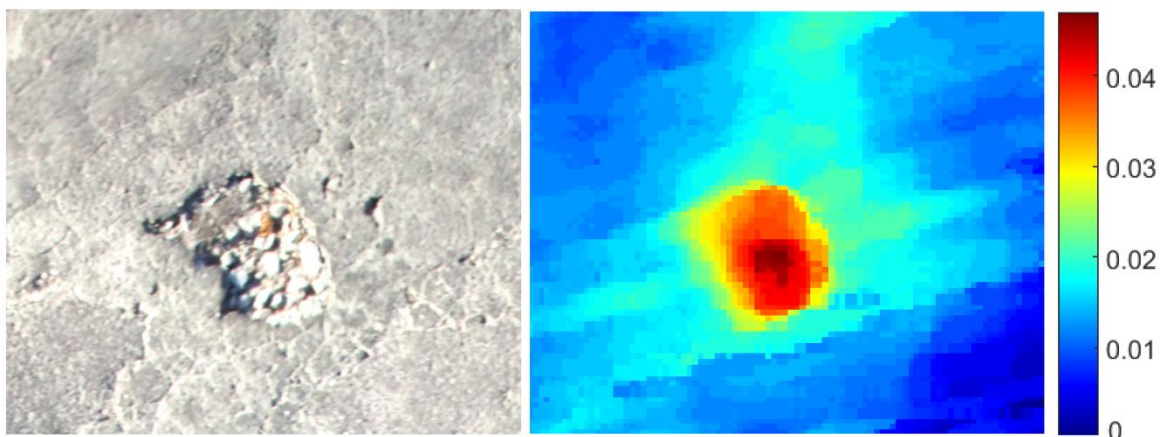


Figure 19. Ortho-photo of a pothole (left), complement of the corresponding height raster (right)

#### 4. Concept of road distress detection and deterioration analysis

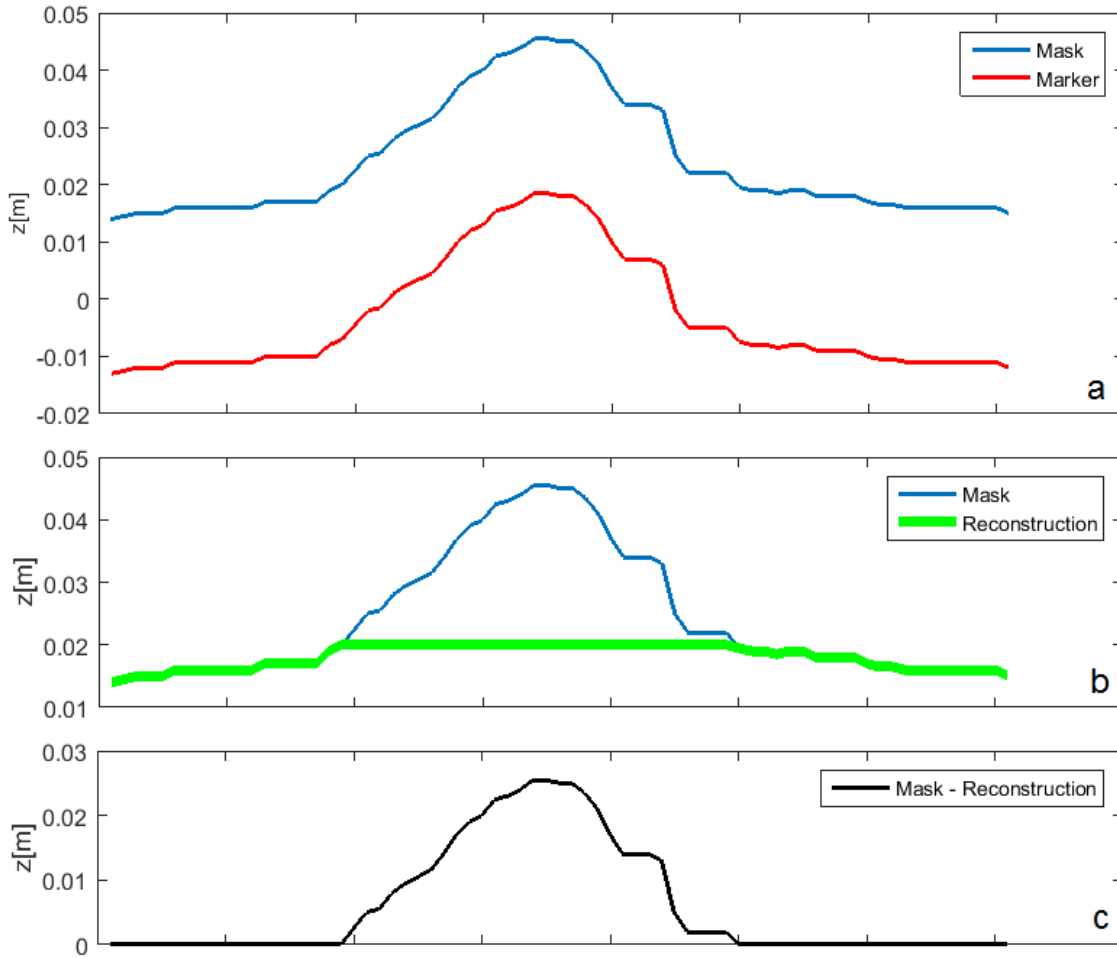


Figure 20. Schematic representation of geodesic morphological reconstruction for pothole detection, the reconstruction is carried out by geodesic dilation

#### 4.4.2. Pothole detection using 2D polynomial fitting (curve fitting)

For pothole detection, a 2D polynomial surface fitting procedure is proposed which is a generalization of the rut detection algorithm using 1D polynomial fitting (see section 4.3.1). (Negussie, 2015) investigated pothole detection using polynomial fitting on the portion of the road pavement surface which contains potholes. Due to the unequal longitudinal and transverse laser point distance the proposed algorithm starts by interpolating the laser point cloud.

The proposed algorithm used in this dissertation is as follow: First the exemplary surface which contains the potholes is selected. Due to the unequal longitudinal and transverse laser point distance the interpolation is applied. The main step is the iterative polynomial approximation of the surface for which 3<sup>rd</sup>, 4<sup>th</sup> or 5<sup>th</sup> order polynomials are used. These orders are empirically chosen. Choosing higher order polynomial leads to overfitting.

A) Approximate the surface using least squares adjustment

Eq ( 15 ) is the bi-variate polynomial of 3rd order.

$$z = a_0 + a_1x + a_2y + a_3x^2 + a_4y^2 + a_5xy + a_6x^3 + a_7y^3 + a_8x^2y + a_9xy^2 \quad (15)$$

This curve has 10 coefficients which are estimated by a linear adjustment according to Eq ( 5 ). Similar to section 4.3.1, the interpolated points of the pavement surface are used to estimate 2D polynomial coefficient  $a_i$ .

- B) Subtract the grid heights from the corresponding heights of the approximating polynomial.
- C) Generate a new surface raster heights in such a way that for each grid location  $(x_i, y_i)$ , the greater height of either the original surface raster heights or the approximating polynomial is selected. That means, original raster heights which are above the approximating polynomial are retained, while parts which are below are replaced by the approximating polynomial.
- D) Iterate the steps B and C until the number of grid points above the approximating polynomial is less than a certain threshold e.g. 1% of  $n$ .

It can happen that for a rough surface, some small elevations (local peaks) which may appear on the ground are neglected by step (D). Figure 21 and Figure 22 show a portion of a road surface and its corresponding surface raster which contains several potholes. A fitted 5<sup>th</sup> order polynomial on top of the surface raster is illustrated in Figure 23.



Figure 21. Orthomosaic of a portion of the road surface with several potholes

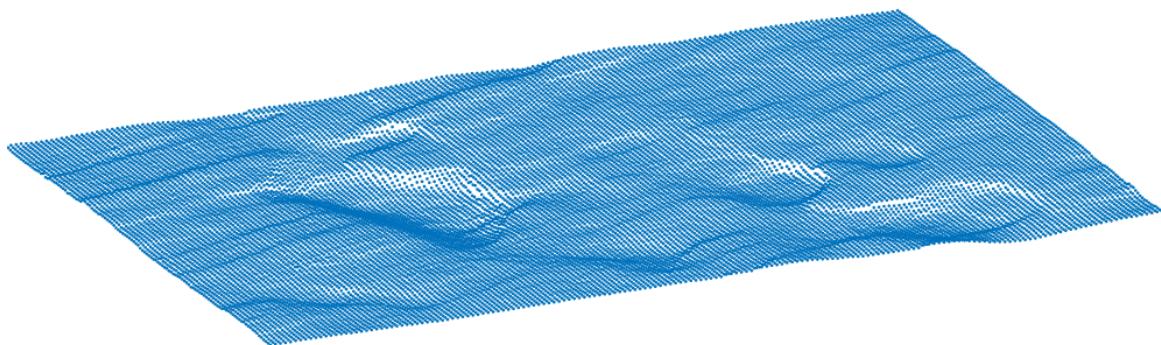


Figure 22. Oblique view of the height raster of the Figure 21

#### 4. Concept of road distress detection and deterioration analysis

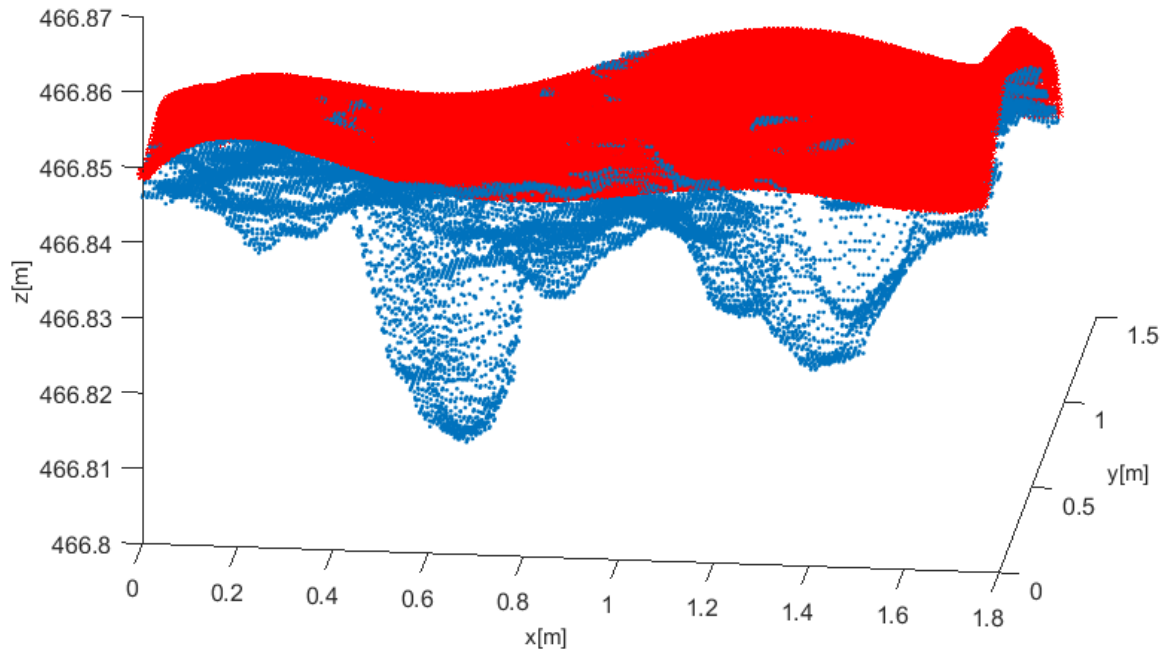


Figure 23. Iterative 2D polynomial fitting onto the road surface shown in Figure 21 after 50 iteration

### 4.5. Crack detection

Cracks appear mostly as narrow and expanded dark areas in the images. For the detection of pavement cracks in images captured by the mobile mapping system (see chapter 3), filtering using three rotation invariant kernels is proposed and described in detail in the following sections. The implemented kernels are Line Filter (LF), High-pass Filter (HPF) and Modified Local Binary Pattern (MLBP). A conceptual aspect of the procedure is to achieve a high degree of completeness. This is taken into account by fusion of filtering results.

#### 4.5.1. Primary filtering for image smoothing

To eliminate noise in the pavement images and also reduce the influence of the aggregates in the asphalt surface) median filter, Gaussian filter, bilateral filter and morphological dilation are typical filters which might be used to smooth the original pavement surface images. Among all above mentioned filters, bilateral filter is described as follows. (Paris, et al., 2009) stated that bilateral filter is similar to Gaussian filter, but additionally, it considers the pixel value differences with the neighbours in order to preserve edges during the smoothing process. The following equation describes the bilateral filter which is defined by a normalized weighted average of two Gaussians:



$$BF[I]_p = \frac{1}{W_p} \sum_{q \in S} G_{\sigma_s}(\|p - q\|) G_{\sigma_r}(|I_p - I_q|) I_q \quad (16)$$

Here,  $BF[I]_p$  is the filtered pixel value,  $p$  corresponds to the coordinates of the pixel which is to be filtered and  $q$  is the coordinates of the neighbouring pixels.  $W_p$  denotes the normalization factor:

$$W_p = \sum_{q \in S} G_{\sigma_s}(\|p - q\|) G_{\sigma_r}(|I_p - I_q|) \quad (17)$$

$G_{\sigma_s}$  denotes a spatial Gaussian weighting which reduces the impact of distant pixels.  $G_{\sigma_r}$  indicates a range Gaussian weighting which decreases the effect of neighbouring pixels  $q$  if their grey values are unequal to  $I_p$ . Figure 24 illustrates the effects of  $\sigma_r$  and  $\sigma_s$  which are called range and spatial parameters, respectively. If  $\sigma_r$  increases, the bilateral filter ‘gradually approximates Gaussian convolution more closely because the range Gaussian  $G_{\sigma_r}$  widens and flattens, i.e., is nearly constant over the intensity interval of the image’ (Paris, et al., 2009). Moreover, larger features will be smoothed by increasing  $\sigma_s$ . The spatial and the range parameters supply more functionalities than common Gaussian filter. There will be no smoothing on the image if both of parameters get to near zero (Paris, et al., 2009).

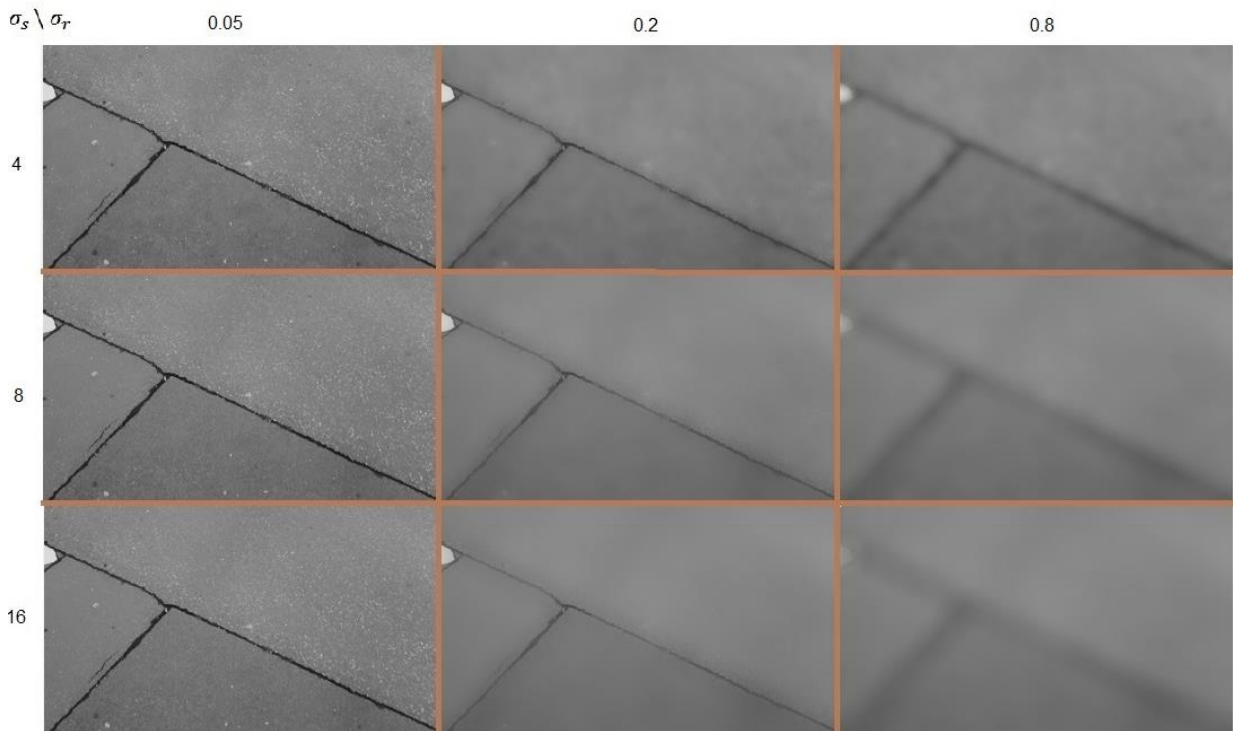


Figure 24. The effects of spatial ( $\sigma_s$ ) and range ( $\sigma_r$ ) parameters

#### 4. Concept of road distress detection and deterioration analysis

##### 4.5.2. Line filtering

Line filtering is carried out by template matching on some resolution levels in order to facilitate the detection of cracks which have different width in the imaged scene. The number of resolution levels depends on the image ground resolution and the crack width. Processing is done in a hierarchical manner from a coarse level (e.g. 1/8) to the original image resolution (1/1). The templates are masks for LF. The vertical oriented mask  $\mathbf{m}$  of the line filter is defined by:

$$\mathbf{m} = \frac{1}{n(n-1)} \begin{bmatrix} 1 & \dots & 1 & -(n-1) & 1 & \dots & 1 \\ & & & -(n-1) & & & \\ & & & -(n-1) & & & \\ & & & \dots & & & \\ & & & -(n-1) & & & \\ & & & -(n-1) & & & \\ & & & -(n-1) & & & \\ 1 & \dots & 1 & -(n-1) & 1 & \dots & 1 \end{bmatrix}_{n \times n} \quad (18)$$

By rotating the mask  $\mathbf{m}$ , further masks with different orientation are generated to achieve a rotation invariant kernel family. In this study, a kernel family of 18 quadratic is used which have incremental rotation angle of  $10^\circ$ . The width of the 2D quadratic masks amounts to an odd number (Miraliakbari, et al., 2014), (Miraliakbari & Hahn, 2014), (Miraliakbari, et al., 2016).

A convolution using mask  $\mathbf{m}$  calculates the average of the ‘neighbourhood left and right from the central pixels’ and subtracts the mean value of the central pixels from the neighbourhood mean. For a  $21 \times 21$  template the width of 10 pixels at the right and left of template centre must guarantee that enough neighbourhood is considered. Theoretically, the length of width and height of the template can be different. Experimental investigations indicated that the equal extend in both directions is appropriate (Miraliakbari, et al., 2016).

For the process of LF by template matching, some more mathematical details are given in the following. The images with different resolution levels ( $\mathbf{J}_k$ ) will be convolved with all masks of the template (in this method with 18 masks)  $\mathbf{m}_i$  according to Eq.( 19):

$$\mathbf{M}'''_{i,k} = \mathbf{J}_k * \mathbf{m}_i \quad (19)$$

The result of the convolution  $\mathbf{J}_k * \mathbf{m}_i$  is the same as the correlation  $\mathbf{J}_k \star \mathbf{m}_i$  because the kernel of LF is symmetric with respect to its centre. In order to scale the result of correlation to the normalized cross-correlation,  $\mathbf{M}'''_{i,k}$  is divided by the STDs of image windows ( $\sigma_{\mathbf{J}_k}$ ), the STD of the template ( $\sigma_{\mathbf{m}_i}$ ) and the kernel size ( $\mathbf{M}'''_{i,k}/\sigma_{\mathbf{J}_k}\sigma_{\mathbf{m}_i}n^2$ ) (Miraliakbari, et al., 2016). Here,  $k$  denotes the resolution level (from coarse to fine) and index  $i$  represents the template number based on its rotation angle (from 0 to 17). The relationship between the normalized cross-correlation and the convolution is addressed as follows:

The algorithmic implementation for normalization of the convolution is carried out in two steps:



$$\mathbf{M}''_{i,k} = \mathbf{J}_k * (\mathbf{m}_i / \sigma_{m_i}) \quad (20)$$

$$\mathbf{M}'_{i,k} = \mathbf{M}''_{i,k} \cdot / \sigma_{J_k} \quad (21)$$

$\mathbf{M}''_{i,k}$  is the convolution result obtained by convolving the image  $\mathbf{J}_k$  on resolution level  $k$  with the  $i^{th}$  mask of the template  $\mathbf{m}_i / \sigma_{m_i}$ . The mask in Eq( 20 ) is normalized by its STD.  $\mathbf{M}'_{i,k}$  is obtained by pointwise division of the matrix elements of  $\mathbf{M}''_{i,k}$  and the matrix elements of  $\sigma_{J_k}$ .  $\sigma_{J_k}$  is a matrix with the same size of  $\mathbf{J}_k$  and represents the STDs of the image windows  $\mathbf{C}_{r,c}$ . Here,  $r$  and  $c$  denote the indices of central pixel of image window in the original image. The size of the image window is equal to the size of the mask. In every resolution level  $k$ ,  $\mathbf{M}'_{i,k}$  contains  $i$  different results regarding the  $i^{th}$  mask. By normalizing  $\mathbf{M}''_{i,k}$  with  $\sigma_{J_k}$ , the result of normalization leads to a correlation as shown in the following.

The empirical covariance of the image window and the template can be written as:

$$Cov(\mathbf{C}, \mathbf{m}_i) = \frac{1}{n^2} \sum_{p=-\frac{(n-1)}{2}}^{\frac{(n-1)}{2}} \sum_{q=-\frac{(n-1)}{2}}^{\frac{(n-1)}{2}} (\mathbf{C}(p, q) - \mu_c)(\mathbf{m}_i(p, q) - \mu_{m_i}) \quad (22)$$

where  $\mu_c$  denotes the mean value of the image window  $\mathbf{C}$  and  $\mu_{m_i}$  represents the mean value of template  $\mathbf{m}_i$ . Due to the definition of the LF kernels (Eq ( 18 )),  $\mu_{m_i}$  amounts to zero:

$$\mu_{m_i} = \frac{1}{n^2} \sum_{p=-\frac{(n-1)}{2}}^{\frac{(n-1)}{2}} \sum_{q=-\frac{(n-1)}{2}}^{\frac{(n-1)}{2}} \mathbf{m}_i(p, q) = 0 \quad (23)$$

Hence, Eq ( 22 ) can be reformulated as:

$$Cov(\mathbf{C}, \mathbf{m}_i) = \frac{1}{n^2} \left( \sum_{p=-\frac{(n-1)}{2}}^{\frac{(n-1)}{2}} \sum_{q=-\frac{(n-1)}{2}}^{\frac{(n-1)}{2}} \mathbf{C}(p, q) \mathbf{m}_i(p, q) - \sum_{p=-\frac{(n-1)}{2}}^{\frac{(n-1)}{2}} \sum_{q=-\frac{(n-1)}{2}}^{\frac{(n-1)}{2}} \mu_c \mathbf{m}_i(p, q) \right) \quad (24)$$

As a consequence of  $\mu_{m_i} = 0$  follows:

#### 4. Concept of road distress detection and deterioration analysis

$$\sum_{p=-\left(\frac{n-1}{2}\right)}^{\left(\frac{n-1}{2}\right)} \sum_{q=-\left(\frac{n-1}{2}\right)}^{\left(\frac{n-1}{2}\right)} \mu_c \mathbf{m}_i(p, q) = 0 \quad (25)$$

Finally, the covariance of image window  $\mathbf{C}_{rc}$  and  $\mathbf{m}_i$  is obtained as follows:

$$\text{Cov}(\mathbf{C}, \mathbf{m}_i) = \frac{1}{n^2} \sum_{p=-\left(\frac{n-1}{2}\right)}^{\left(\frac{n-1}{2}\right)} \sum_{q=-\left(\frac{n-1}{2}\right)}^{\left(\frac{n-1}{2}\right)} \mathbf{C}(p, q) \mathbf{m}_i(p, q) \quad (26)$$

This equation represents convolution of image portion  $\mathbf{C}_{rc}$  and template  $\mathbf{m}_i$  divided by  $n^2$ . Reshaping of all  $\text{Cov}(\mathbf{c}, \mathbf{m}_i)$  values with respect to the  $\mathbf{C}_{rc}$  indices produces a matrix called  $\mathbf{Cov}(\mathbf{C}, \mathbf{m}_i)$  which has the same size of the original image in each resolution level  $k$ . The matrix of normalized cross-correlation is defined as:

$$\rho_{J_k \mathbf{m}_i} = \mathbf{Cov}(\mathbf{C}, \mathbf{m}_i) / (\sigma_{J_k} \sigma_{\mathbf{m}_i}) \quad (27)$$

Dividing  $\mathbf{M}'_{i,k}$  by  $n^2$  gives the matrix of normalized cross-correlation of the image and the mask. The relationship between Eq. ( 21 ) and Eq. ( 27 ) is given by:

$$\rho_{J_k \mathbf{m}_i} = \frac{1}{n^2} \mathbf{M}'_{i,k} \quad (28)$$

By calculating the normalized cross-correlation ( $\rho_{J_k \mathbf{m}_i}$ ) the detection of potential cracks is linked to a similarity measure between -1.0 and 1.0. The highest correlation between the image and all masks on each resolution level is found by:

$$\mathbf{M}_k = \max(\rho_{J_k \mathbf{m}_i} \forall i) \quad (29)$$

Classification of the scene into crack and non-crack pixels is carried out by thresholding  $\mathbf{M}_k$  with  $\mathbf{M}_k > \text{corr}_{min} = \mathbf{PC}_k$ , where  $\mathbf{PC}$  stands for potential crack. By merging the  $\mathbf{PC}_k$  of all resolution levels (Eq. ( 30 )) the potential cracks are detected in the image. Wider and narrower cracks of any orientation are expected to be detected by this process (Miraliakbari, et al., 2016).

$$\mathbf{PC} = \max(\mathbf{PC}_k \forall i) \quad (30)$$

Normalized correlation promises independency of the detection procedure from contrast of the image. Such independency has pros and cons. The advantage is the high sensitivity of line detection. For instance, applying this normalization leads to detect some cracks which are located in shadow area.

The disadvantage is that every line-shaped element can be detected; for example also line elements in which aggregates are separated by bitumen. To avoid this dilemma, further histogram analysis must be applied to see if the detected potential cracks are dark enough.

Figure 25 shows a sample of a pavement image including several cracks (left) and the potential crack detection results using the LF variant (right). The cracks are detected in all directions, however, there are some extra areas which are falsely representing the crack regions. These regions mostly belong to the bitumen between neighbouring or some moistures and oily spots on the asphalt surface.

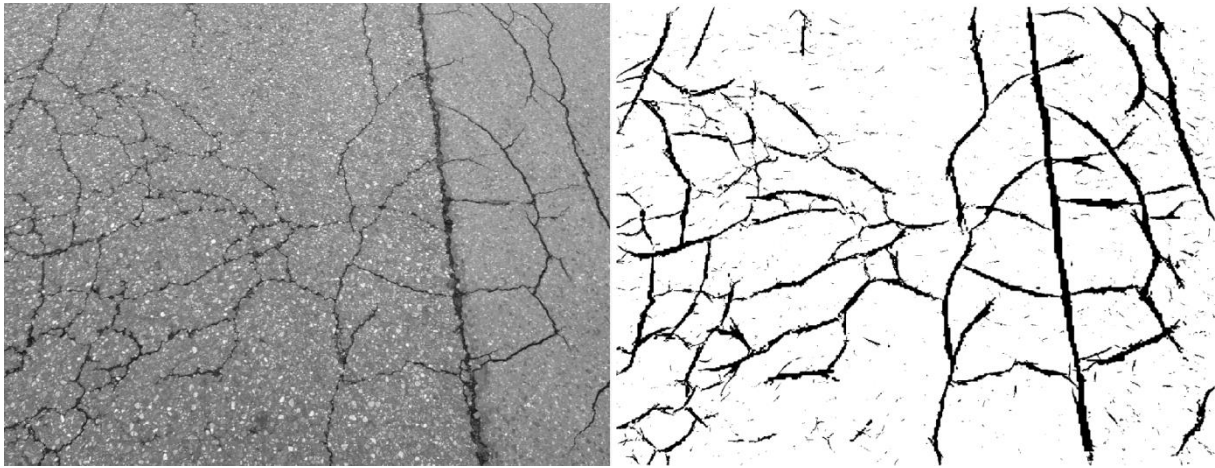


Figure 25. Sample of image (left) and crack detection result using LF (right)

### 4.5.3. High-pass filtering

High-pass filtering is mainly used for edge detection and image sharpening. As described in (Miraliakbari, et al., 2016), a Laplacian kernel  $\mathbf{h}$  is employed to filter the image over all resolution levels:

$$\mathbf{H}'_k = \mathbf{J}_k * \mathbf{h} \quad (31)$$

where  $\mathbf{J}_k$  is the image on the resolution level  $k$  and  $\mathbf{H}'_k$  represents the Laplacian filtered image. The Laplacian kernel  $\mathbf{h}$  used in this dissertation is given by:

$$\mathbf{h} = \begin{pmatrix} -1 & -1 & -1 \\ -1 & 8 & -1 \\ -1 & -1 & -1 \end{pmatrix} \quad (32)$$

In this method, the primary filtering is performed by using bilateral filter. It is very common to smooth the image with a Gaussian filter before applying the Laplacian. Smoothing with bilateral filter follows the same idea but with the advantage that the bilateral filter preserves edges. Adding the input image  $\mathbf{J}_k$  to the filtered image  $\mathbf{H}'_k$  supplies a Laplacian sharpened image  $\mathbf{H}_k$  subsequently (Gonzalez & Woods, 2002).  $\mathbf{H}_k$  contains positive and negative values at the change in the image and the negative responses are likely to be the potential crack positions. Histogram analysis is applied to the Laplacian sharpened image on each resolution level  $k$  to specify proper threshold in order to detect crack pixels. The same as LF approach, fusion over all  $k$  levels is accomplished (Miraliakbari, et al., 2016).

#### 4. Concept of road distress detection and deterioration analysis

Figure 26 shows the grayscale sample of a pavement image (left subfigure). The middle subfigure shows the Laplacian sharpened image  $H_k$ . The result of potential crack detection after thresholding is illustrated in the right subfigure. This result contains noise such as pixels related to the asphalt aggregate boundaries.

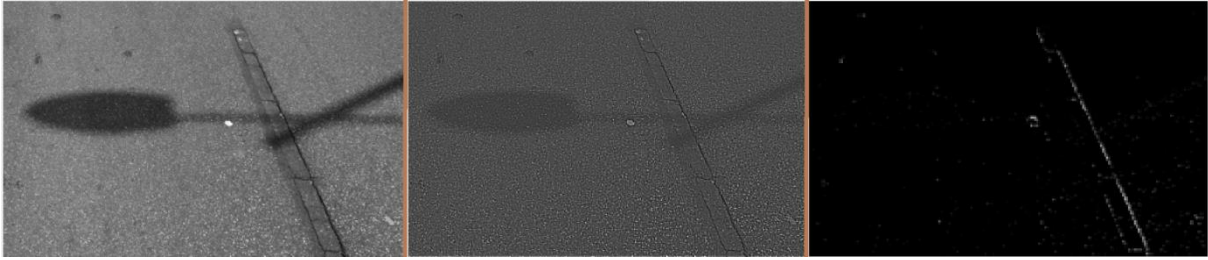


Figure 26. Grayscale image (left),  $H_k$  at resolution level 1/8 (middle) and potential crack positions including noise (right)

#### 4.5.4. Modified Local Binary Pattern (MLBP)

This method of crack detection is inspired by a feature extraction approach called Local Binary Pattern (LBP) which was proposed by (Ojala, et al., 2002) and applied by (Hu & Zhao, 2010) for detection of pavement cracks. LBP is a grey scale and rotation invariant approach for classification of texture. In LBP, the neighbourhood of a pixel is analysed to define the texture. The pattern shown in Figure 27 addresses the circularly symmetric  $P$  neighbouring pixels within the distance  $R$  from central pixel (Miraliakbari, et al., 2016).

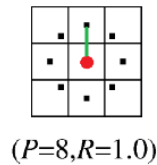


Figure 27. ‘Circularly symmetric neighbor sets’ (Ojala, et al., 2002) for  $P=8$  and  $R=1$  (Miraliakbari, et al., 2016), adapted from (Ojala, et al., 2002)

Texture  $T$  is defined as:  $t(s(g_0 - g_c), s(g_1 - g_c), \dots, s(g_{P-1} - g_c))$  where  $g_p$  represents the grey value of the neighbouring pixel  $p$ ,  $g_c$  refers to the grey level of central pixel  $c$ ,  $t$  denotes the texture operator and

$$s(x) = \begin{cases} 1, & x \geq 0 \\ 0, & x < 0 \end{cases} \quad (33)$$

According to Eq.( 33 ), the operator is grey scale invariant (Miraliakbari, et al., 2016). A factor defined by  $2^P$  is assigned for each  $s(g_p - g_c)$ .  $T$  is then transformed into a unique  $LBP_{P,R}$  which ‘characterizes the spatial structure of the local image texture’ (Ojala, et al., 2002).

$$LBP_{P,R} = \sum_{p=0}^{P-1} s(g_p - g_c) 2^p \quad (34)$$

In order to get rotation invariant “uniform” patterns, the following formula is used:

$$LBP_{P,R}^{riu2} = \begin{cases} \sum_{p=0}^{P-1} s(g_p - g_c) & \text{if } U(LBP_{P,R}) \leq 2 \\ P + 1 & \text{otherwise,} \end{cases} \quad (35)$$

where:

$$U(LBP_{P,R}) = |s(g_{P-1} - g_c) - s(g_0 - g_c)| + \sum_{p=1}^{P-1} |s(g_p - g_c) - s(g_{p-1} - g_c)| \quad (36)$$

Figure 28 illustrates possible rotation invariant binary patterns. The results of Eq. (35) vary from 0 to 9. The patterns shown in the first row of the figure are called “uniform” which have values between 0 to 8. Value 9 is assigned to the rest of the patterns called “nonuniform” (Ojala, et al., 2002).

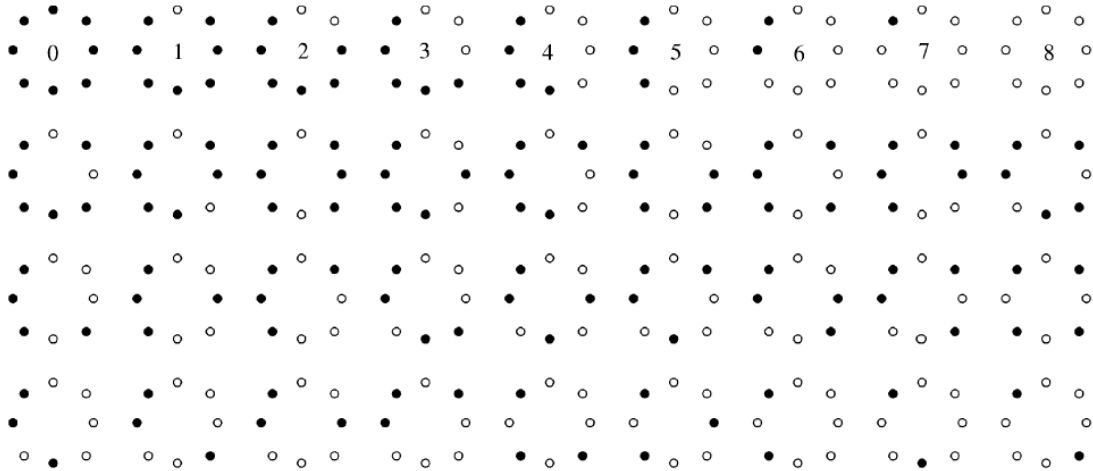


Figure 28. The 36 rotation invariant binary configurations (Ojala, et al., 2002)

For detecting pavement cracks, a modified LBP (MLBP) is implemented. MLBP considers only the patterns marked with numbers 3, 4 and 5 which are edge-shaped and therefore should be suitable for detecting linear structures like cracks. If one of these patterns is detected at a pixel of the image, that location is considered as a potential crack pixel. Hence, three pattern images namely:  $LBP_{3k}$ ,  $LBP_{4k}$  and  $LBP_{5k}$  are generated in each resolution level  $k$ . These three pattern images are fused using the max-operation. The fusion result is defined as  $LBP_{3,4,5k}$ . The texture operator is very discriminative and makes the potential crack result ( $LBP_{3,4,5k}$ ) noisy. Thus, the local variance is employed to reduce the noise by filtering the detected potential cracks (Miraliakbari, et al., 2016). According to (Ojala, et al., 2002) the local variances ( $VAR_{P,R}$ ) of a pixel is the variance of the grey level of all neighbouring pixels i.e. in this study 8 pixels. The local variance (contrast value) is defined as:

#### 4. Concept of road distress detection and deterioration analysis

$$VAR_{P,R} = \frac{1}{P} \sum_{p=0}^{P-1} (g_p - \mu)^2 \quad (37)$$

where  $\mu$  is the mean value of the neighbouring pixels. As described in (Miraliakbari, et al., 2016), the matrix of all local variances of the pavement image pixel is defined by  $\Sigma_{J_k}$ . An empirical threshold is used to convert the image of the local variances into the binary matrix ( $\Sigma_{J_k} > thres$ ). The local variances of the crack pixel boundaries are higher than those of isolated pixels (e.g. location of aggregates). The reason is that the central pixels are not taken into account in the local variance calculation. Potential cracks are detected in each resolution level by:

$$PC_k = (\Sigma_{J_k} > thres) \cap LBP_{3,4,5_k} \quad (38)$$

The final result of the MLBP is obtained by merging the  $PC_k$  with the max-operation like for the LF and HPF approaches.

##### 4.5.5. Post-processing of the potential crack regions

Most distinctive feature between crack and non-crack regions in the  $PC$  results of the LF, HPF and MLBP approaches is the size of the region. For eliminating small  $PC$  regions, the geometric properties of area and roundness are used. The crack regions have a larger area and lower roundness than non-crack regions; therefore, non-crack regions are eliminated if  $A < A_{min}$  and  $> Rounness_{min}$ . The post-processing is continued by removing the border of road marks which might be detected as potential crack. Road marks appear frequently in the mobile images and have a darker border compared to their bright surface and are even sometimes darker than the intact asphalt. This is because of aging, shadow or moisture. Road marks also appear as a distinctive peak in the histogram. Therefore it is easy to remove corresponding boundary pixels. In the MLBP approach additional morphological operations are used. Erosion is applied to disjoint non-crack pixels from the crack segments and closing is used to fill the gaps between the detected edges of the cracks (Miraliakbari, et al., 2016).

##### 4.5.6. Feature fusion implementation

The completeness of the potential cracks detected using prior approaches will always be limited. On the other hand, following the post-processing, not all non-crack regions have disappeared. In order to increase the percentage of the completeness of the crack detection and eliminate the existing non-crack regions, a feature fusion approach is pursued. The concept of feature fusion is to fuse the results of the LM, HPF and MLBP approaches which are  $PC_{LM}$ ,  $PC_{HPF}$  and  $PC_{MLBP}$ , respectively. The union of all detected potential crack results:

$$\mathbf{PC}_{\cup} = \mathbf{PC}_{LM} \cup \mathbf{PC}_{HPF} \cup \mathbf{PC}_{MLBP} \quad (39)$$

is a set of all objects that are members of  $\mathbf{PC}_{LM}$  or  $\mathbf{PC}_{HPF}$  or  $\mathbf{PC}_{MLBP}$  or of all three  $\mathbf{PC}$ s. The sets are the  $\mathbf{PC}$  matrices, the objects are the binary elements of this matrices indicating a potential crack location by 1 and a potential non-crack location by 0. The intersection of all potential crack results:

$$\mathbf{PC}_{\cap} = \mathbf{PC}_{LM} \cap \mathbf{PC}_{HPF} \cap \mathbf{PC}_{MLBP} \quad (40)$$

is a set of objects that are members of  $\mathbf{PC}_{LM}$  and  $\mathbf{PC}_{HPF}$  and  $\mathbf{PC}_{MLBP}$ . This means only those potential crack regions remain in the intersection result which have been detected by all three approaches.  $\mathbf{PC}_{\cup}$  and  $\mathbf{PC}_{\cap}$  can be linked together by binary reconstruction according to (Vincent, 1993). With the mask  $\mathbf{PC}_{\cup}$  and the marker  $\mathbf{PC}_{\cap}$  which fulfil the condition that  $\mathbf{PC}_{\cap} \subseteq \mathbf{PC}_{\cup}$ , a binary reconstruction from the mask  $\mathbf{PC}_{\cup}$  can be obtained by:

$$R_{\mathbf{PC}_{\cup}}(\mathbf{PC}_{\cap}) = \bigcup_{\mathbf{PC}_{\cap} \cap \mathbf{PC}_{\cup(i)}} \mathbf{PC}_{\cup(i)} \quad (41)$$

According to (Vincent, 1993),  $\mathbf{PC}_{\cup(i)}$  is the set of connected components of  $\mathbf{PC}_{\cup}$ . Eq (41) is a special case of the more general formulation of morphological reconstruction by dilation. For more details please refer to (Vincent, 1993).

## 4.6. Patch detection

Mends like cracks differ in the pavement images from the neighbouring intact road surface. As the term mend in road construction has a general meaning for a fixed area and can contain other regions like sealed cracks, in this study it is preferred to use the term “patch”. It is assumed that patches have mostly common characteristics, namely: a) closed, b) darker and newer than the neighbouring intact asphalt surface, c) very dark boundary, d) homogeneous surface compared to the neighbouring area.

### 4.6.1. Patch detection using geodesic morphological reconstruction

Geodesic dilation is used to examine the feasibility of this reconstruction method for patch detection. The idea is to separate the pavement image into patch and non-patch regions. If patch pixels are darker than the neighbouring area, either geodesic erosion with the grey scale image or geodesic dilation with the complement of the grey scale image (for 8-bit image  $I_{\text{complement}} = 255 - I$  where  $I$  is the grey scale image) is computed. Figure 29 illustrates the procedure of patch detection using geodesic morphology reconstruction. Subfigure (a) shows the original pavement image. In order to smooth the image, the median filter is applied (subfigure (b)). While the dilation option is used for morphological reconstruction and the patch is darker than the neighbouring pavement surface, the complement of the

#### 4. Concept of road distress detection and deterioration analysis

image is calculated and shown in subfigure (c). By performing the complement as mask, the darker regions (mostly patch in this sample) will appear brighter. Hence these regions are expected to be detected via geodesic dilation. Following mask generation, the marker is produced by subtracting a certain grey scale from the overall grey value of the mask which is in this sample 100 (see subfigure (d)). Subfigure (e) illustrates the result of geodesic dilation (reconstructed image). In order to filter out the background (intact pavement surface), the result of geodesic dilation is subtracted from mask (see subfigure (f)). At this stage, mostly the black region has grey scale equal 0 (background) and the rest of the scene, depending on the subtraction result, hold positive value. Subfigure (g) shows the thresholded result of subfigure (f). Apart from the detected patch region, small depression of the road section is also detected which must be filtered in the final step (see subfigure (h)).

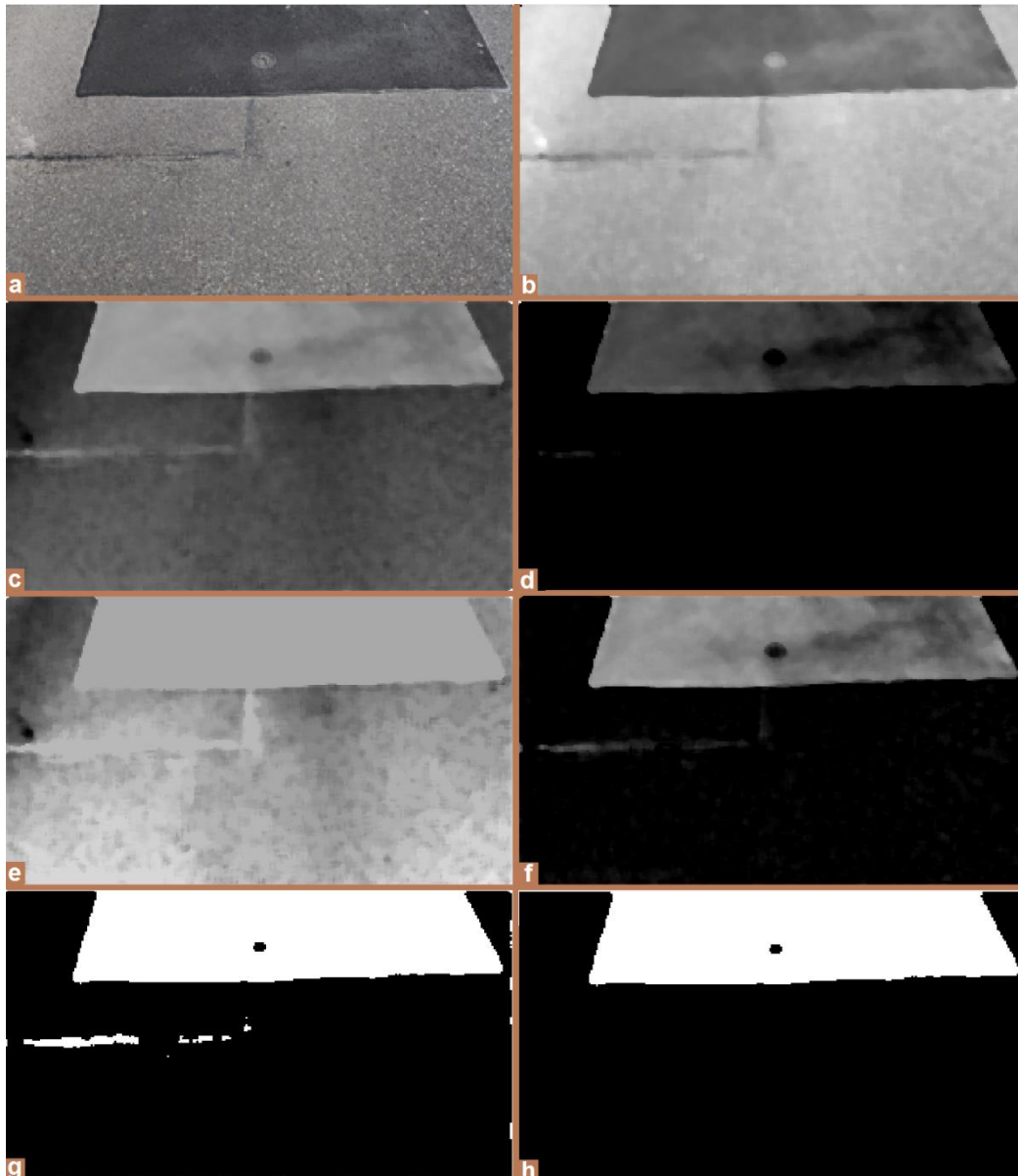


Figure 29. a) original pavement image, b) filtered image using median filter, c) complement of filtered image (mask), d) subtraction of a certain grey scale from mask (marker), e) result of geodesic dilation (reconstructed image), f) subtraction of geodesic dilation result from mask, g) thresholded result of (f), g) filtered result of (g)



#### 4.6.2. Patch detection using texture measures (gradient magnitude and local STD)

The very dark boundary between the patch and intact pavement surface is considered to separate the image scene into patch and non-patch regions. Figure 30 represents the flowchart of the automatic patch detection using the image gradient magnitude. With the grey scale image, the gradient magnitude image is calculated. The boundaries around the patches show up as borders of high magnitude. On the other hand the small magnitudes represent the pixels which belong to the homogenous surface. With the threshold selection methods, e.g. the method proposed by (Otsu, 1979), a proper threshold for gradient magnitude image can be found. By thresholding, the boundaries of the patches but also the boundaries between the bitumen and aggregates are detected. Although the first assumption is that the border of the patches is mostly shown as closed line in the binary results, the mobile images may not always cover the whole patch area. So the algorithm looks first for the regions with hole which refer to the first assumption (appearance of the isolated patch in the mobile image). If the size of the region is more than a certain number of pixels, this region will be a patch candidate otherwise it will be filtered out. If the mobile image does not cover the whole patch area, the intersection of the patch boundary with the image border closes the line segment and the new close region will also be considered as patch candidate. As patches mostly have less grey level than the intact pavement surface, the average of the grey value of the patch candidate region(s) is considered to define the patch region.

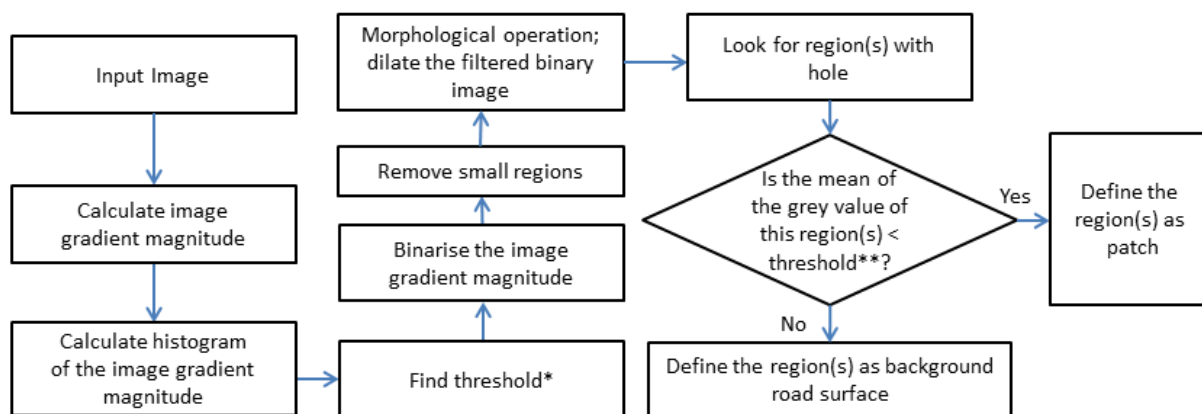


Figure 30. Flowchart of gradient-based patch detection (threshold\* and threshold\*\* correspond to image gradient magnitude and image grey value, respectively)

Figure 31 shows the histogram of the image gradient magnitude. Inspired by Otsu's proposal to obtain an automatic threshold, the following procedure for automatic thresholding is proposed: A straight-line is defined through the highest peak (highest count) and end of the histogram. The bin number which belongs to the longest distance between the histogram curve and the straight-line is considered as the threshold.

#### 4. Concept of road distress detection and deterioration analysis

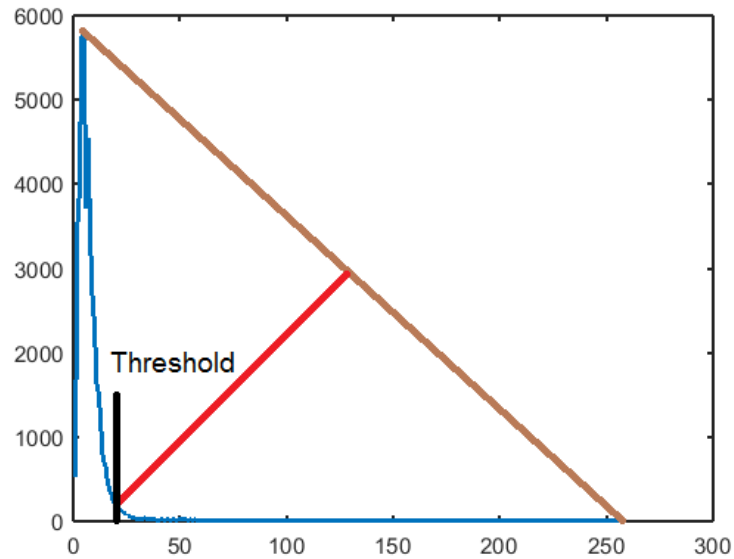


Figure 31. Automatic thresholding using histogram of image gradient magnitude

By thresholding the magnitude image, a binary image is obtained which shows the borders between the darker and brighter objects. In road images, those objects are mostly the patches, road marks and aggregates. Therefore, in addition to the patch boundaries, there will be always artefacts in the thresholded result (see Figure 32).

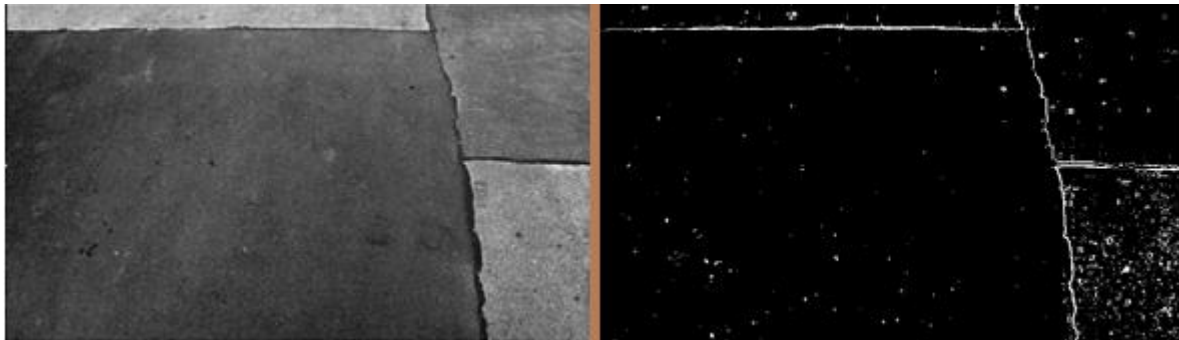


Figure 32. Binary image generated by the automatic thresholding

Area as one of the geometric properties is used to filter the artefacts which are mainly the boundary between the aggregates and bitumen. Figure 33 shows the result of filtered binary image (top-left), dilated-filtered binary image (top-right), filtering non-linear regions using roundness (bottom-left), labelling the areas for classification of the scene into patch and non-patch classes (bottom-right).

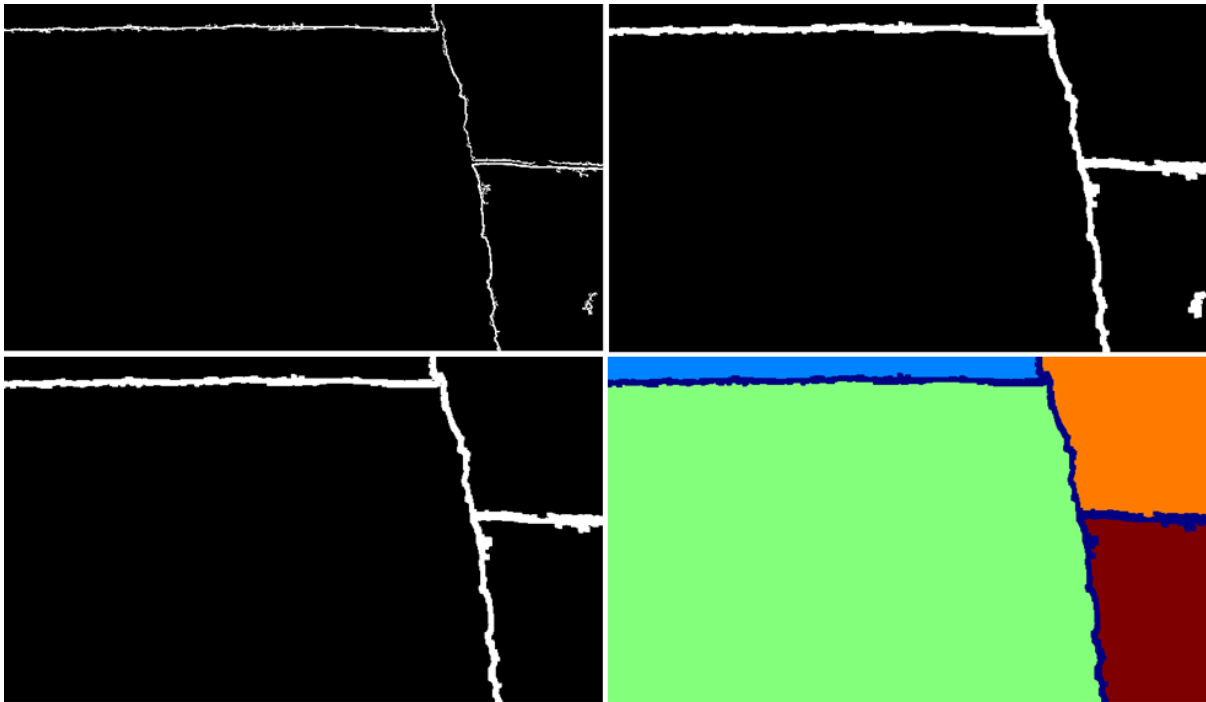


Figure 33. Filtered binary image (top-left), dilated-filtered binary image (top-right), removing non-linear regions using roundness (bottom-left), four separated areas (bottom-right)

Classification uses the mean grey value of each area. Dark areas (orange and green area in Figure 33) are classified as patches and are separated from the rest of the pavement.

Patches in pavement images may differ with respect to homogeneity and colour. Further, their boundaries to neighbouring asphalt surfaces might not have sharp edges. In such cases, the gradient-based processing may fail and an alternative approach is needed to detect the patch areas. An alternative is to use the variance or 'local STD' as texture measure rather than the gradient magnitude. Figure 34 shows the procedure of patch detection using 'local STD'.

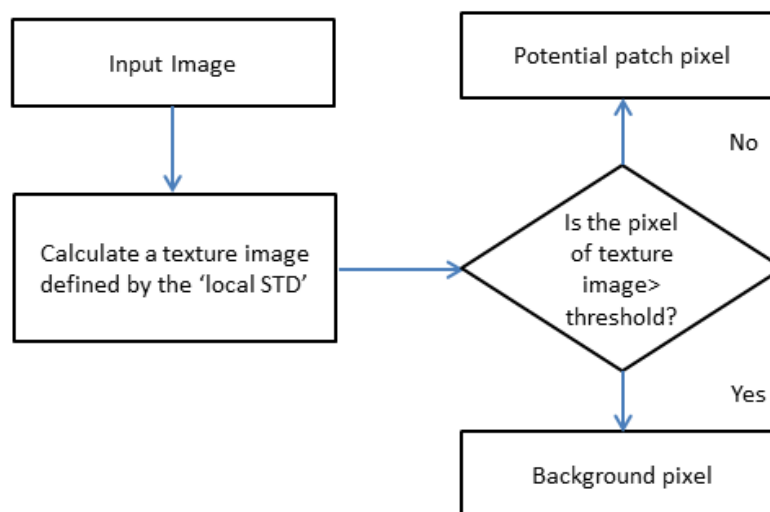


Figure 34. Local STD-based patch detection

#### 4. Concept of road distress detection and deterioration analysis

Figure 35 shows a pavement image sample which has different patches. The local STD-based approach is useful for this kind of pavement images containing several patches which have unequal age and material.

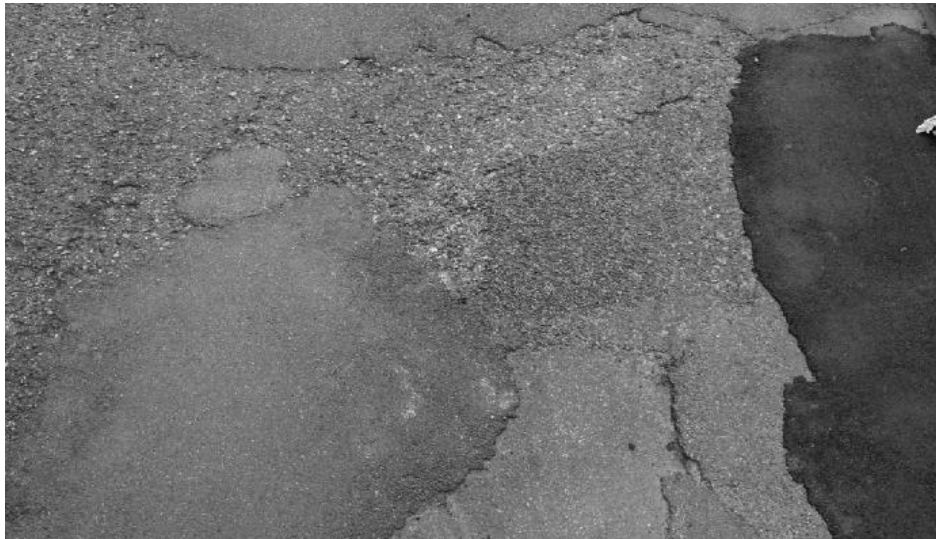


Figure 35. A pavement grey scale image with different patches

The different regions shown in this figure differ with respect to the grey tone and variability. The patches are fairly homogeneous as there are almost no aggregate visible in the patch regions. Therefore, the texture image obtained by filtering the image with 'local STD' within those regions will have less value than the neighbouring regions. Figure 36 illustrates the texture image obtained by filtering the image with 'local STD'. The brighter regions (shown with number 1 to 7) represent the lower 'local STD', therefore, they are more likely to be patches than the other areas.

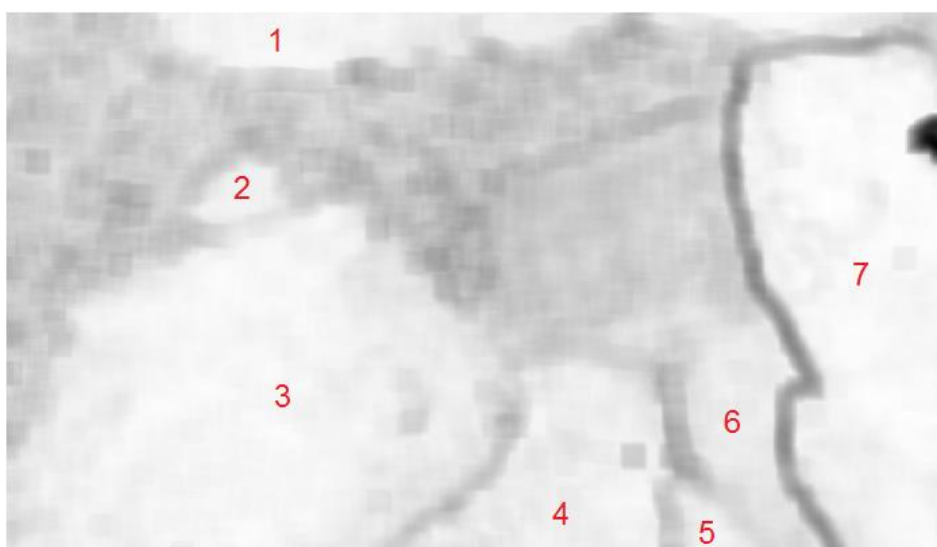


Figure 36. The texture image obtained by filtering the image with 'local STD'

## 4.7. Asphalt pavement quality analysis using spectrometry

According to (Curran, 1994), a goal of remote sensing is to distinguish objects on the ground's surface using radiation which 'has interacted with the surface'. Such an objective can be pursued by means of an imaging spectrometer. The spectrometer can record 'a finely-sampled and continuous spectrum of radiation' for the total range of 400 nm to 2400 nm (Curran, 1994). The Polytec PSS 2221 introduced in section 3.4.1 allows recording data in 256 bands in the wavelength range of 1253 nm to 2259 nm.

### 4.7.1. Spectral feature analysis

(Heiden, et al., 2007) consider various linear and non-linear features, related to the recorded spectral domain. Some of them are mean, STD, depth of absorption, or slope in a certain wavelength range. The values of these features can be determined for certain materials recorded in a laboratory environment. In this research, empirical linear features by visual inspection of the training signatures are defined. Comparison of those feature vectors with the feature vectors from LDA reveals correspondences in the respective wavelength range. Line slope is one of the simplest and most important features tested in this study. A line fitting by regression yields the following formula for the line slope within the wavelength domain of  $\lambda_k$  to  $\lambda_{k+1}$  (Engels, et al., 2015):

$$LS = \sum_{j=0}^{N-1} r_{k+j} \left\{ \frac{6(2j+1-N)}{N \Delta\lambda (N+1)(N-1)} \right\} \quad (42)$$

The wavelength domain begins with  $\lambda_k$ . In this formula,  $r_{k+j}$  is the reflectivity value of  $\lambda_{k+j}$ ,  $N$  denotes the number of the reflections within the domain and  $\Delta\lambda$  is the wavelength increment.

### 4.7.2. Linear discriminant analysis (LDA)

For a supervised classification it is beneficial to find appropriate discriminating features, i.e. functionals of the spectral signatures, which enable a robust separation of the classes irrespective of possible in-class variations. Such features are most easily established if previous physical knowledge about the reflective properties of the respective material classes is available. In the case of road condition determination e.g., the aging and deterioration of asphalt is accompanied by a decrease of hydrocarbonate absorption, see e.g. (Cloutis, 1989); the occurrence or absence of such absorptions is an ideal indicator for the road condition. In real world applications, however, pure materials are rarely encountered, and sometimes epiphenomena are more significant for a material state than evidence from lab analysis. It is accordingly often preferable to determine best-discriminating features empirically from training data. Admittedly, empirical methods entail the risk that the training data have, apart from their nominated class association, unrecognized common properties which cause a bias in the determined features. Therefore, the training data must be carefully selected and have to cover a wide variety of instances of the nominated material class.

#### 4. Concept of road distress detection and deterioration analysis

A well-established method for the extraction of optimal linear features from training data is the Linear Discriminant Analysis (LDA), which was conceived by (Fisher, 1936). The basic idea is to find directions in feature space, along which the separation of the classes is optimal in a certain sense. These so-called “feature vectors” obviously correspond to linear combinations of the original spectrometric channels; in most cases, there is no ready physical interpretation for these empirical features. In the definition of the optimal feature vectors not only the differences of the class centres, but also the within-class covariance matrices are taken into account.

In the simplest case, LDA deals with only two classes which is sufficient for purpose of this study, i.e. separation between good and bad road sections. In this case, there is only one feature vector  $\mathbf{w}$ . It gives the direction, for which the ratio of the between-class covariance  $\mathbf{S}_B$  and within-class covariance  $\mathbf{S}_W$  is maximal:

$$J(\mathbf{w}) = \frac{\mathbf{w}^T \mathbf{S}_B \mathbf{w}}{\mathbf{w}^T \mathbf{S}_W \mathbf{w}} \rightarrow \max \quad (43)$$

The target function  $J(\mathbf{w})$  can be interpreted in terms of the normalized difference of the class means in the respective direction, i.e. their coordinate difference (with respect to the axis given by the feature vector) divided by its STD. Thereby, the resulting value for the target function immediately represents a measure for the separability of the classes.

Elementary calculus leads to the following generalized eigenvalue problem:

$$\mathbf{S}_B \mathbf{W} = \lambda \mathbf{S}_W \mathbf{W} \quad (44)$$

Here the eigenvalue  $\lambda$  equals the target function  $J(\mathbf{w})$ . This problem is commonly transformed to a standard eigenvalue problem by diagonalization of the within-class covariance matrix. In a second step, the transformed eigenvalue problem is solved; finally the eigenvector corresponding to the biggest eigenvalue is back-transformed (Engels, et al., 2015).

$$\mathbf{S}_{new} \mathbf{W}_{new} = \lambda \mathbf{W}_{new} \quad (45)$$

$\mathbf{W}_{new}$  and  $\lambda$  are both the unknown which must be solved from ordinary eigenvector problem. The next step is to back transfer the  $\mathbf{W}_{new}$  to  $\mathbf{W}$ .

LDA turns out to be a beneficial tool for the reduction of dimensionality, which greatly facilitates subsequent classifications. Furthermore, the components of the feature vectors  $\mathbf{W}_i$  represent valuable information which original channels are significant for the classification. In this dissertation, two classes “Bad” and “Good” are proposed for separability analysis. Classification of the mobile spectrometry data is carried out using training data (containing the two mentioned classes) which are captured separately. Result of classification might look inhomogeneous due to the short distance

#### 4.8. Integration of road distresses and spectrometry classification outcomes

interval between the spectrometry spots. The spectral signatures may slightly vary from one point to the next point which is in the vicinity of ca. 3 cm to 5 cm of previous point and by chance be classified differently from the neighbouring spots. The majority filter is proposed to overcome this difficulty.

#### **4.8. Integration of road distresses and spectrometry classification outcomes**

The last step of the concept concentrates on the integration of road distresses. All results are geo-referenced which helps to integrate and visualize them in a GIS package. In this dissertation, the four pavement distresses: rut, pothole, crack and patch and the classification result of mobile spectrometry are integrated. A joint evaluation of all detection and classification results for road condition mapping can be applied afterwards, but this is not part of this dissertation.

## 5. Laser scanning data processing, results and discussion

In this chapter two pavement distresses are detected by means of laser scanning data, namely: rut and pothole. Following section describes and analyses the result of road surface extraction.

### 5.1. Road surface and boundary extraction

In this section three aims are investigated. The first aim is to find out whether a one- neighbourhood (1N) or a four-neighbourhood region growing (4N) is more beneficial for the extraction of the pavement surface. For this purpose, the processing of a 4N and a 1N region growing using HB variant are compared. The second aim is to compare HB and HDB processing and understand which one is more advantageous to use. The last aim of this section is to select proper threshold for data processing.

#### 5.1.1. Comparison of one- and four- neighbourhood regions growing

As described in section 4.2.2, two- and four-neighbourhood region growing are proposed for road pavement surface extraction. 4N region growing causes more overshoot region (commission error). If there is partly low or no curbstone within the point cloud segment, the region growing passes beyond the road border, continues on the sidewalk and considers the whole pedestrian area of the road segment as the road surface. In contrast, when 1N region growing penetrates from road border with low or no curbstone into the sidewalk, it continues only in 1 direction. Therefore, less pedestrian area of the point cloud segment will be identified as road surface (Miraliakbari, et al., 2015). Figure 37 illustrates the difference between 4N and 1N region growing using HB variant regarding to the overshoot regions. Both subfigures are chosen from the same region and point cloud data. The threshold for the termination of data processing is 2 cm for both region growing variants. In the upper subfigure which illustrates the result of 4N region growing, many parts of the pedestrian area are falsely detected as pavement surface because after passing the road boundary, the region growing continues in 4 directions and misclassifies the whole sidewalk of the point cloud segment. In the lower subfigure which shows the result of 1N region growing, fewer pedestrian regions are falsely discovered as road surface. The lower subfigure shows that only small regions of the road boundary (marked with the yellow circles) contain either no curbstone or curbstone which is lower than the threshold. It is obvious that the region growing continues only in 1 direction and misclassifies only few parts of the sidewalk as road surface.



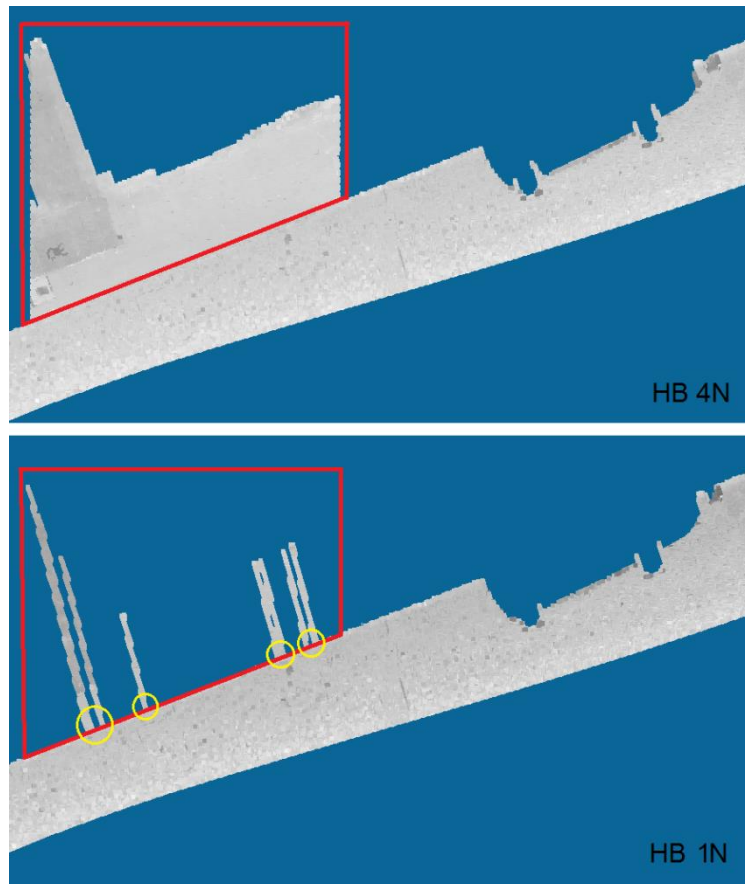


Figure 37. Comparison of 4N (top) and 1N (Bottom) region growing using HB variant regarding to the overshoot regions

In case of gap region (omission error), 4N region growing produces less gap region compared to the 1N region growing. If there are some distresses such as cracks and potholes in the pavement surface, the 4N region growing will not stop even though the height difference is more than the predefined threshold and continues along the other directions. In contrast, the 1N region growing terminates the process of road surface extraction in the vicinity of the pavement distress because it continues only in one direction. Figure 38 shows the difference between 4N and 1N region growing using HB variant regarding to the gap region. Like in Figure 37, the scene, input point cloud data and the threshold are the same for both subfigures. Regions A and B which are surrounded by red circles are the locations with gap regions for both 4N and 1N regions growing. Region A shows the location of pavement distress. Whereas 1N region growing stops when it meets the distress border, 4N region growing continues from the other directions and detects the intact road surface area which is behind the distress. However, also the result of 4N region growing contains gap regions. Region B shows location of a street gully. Due to the shortage of laser scanning data on the gully, it is expected that both region growing variants perform the same results at this region, however, 4N region growing extracts partial area of gully surface.

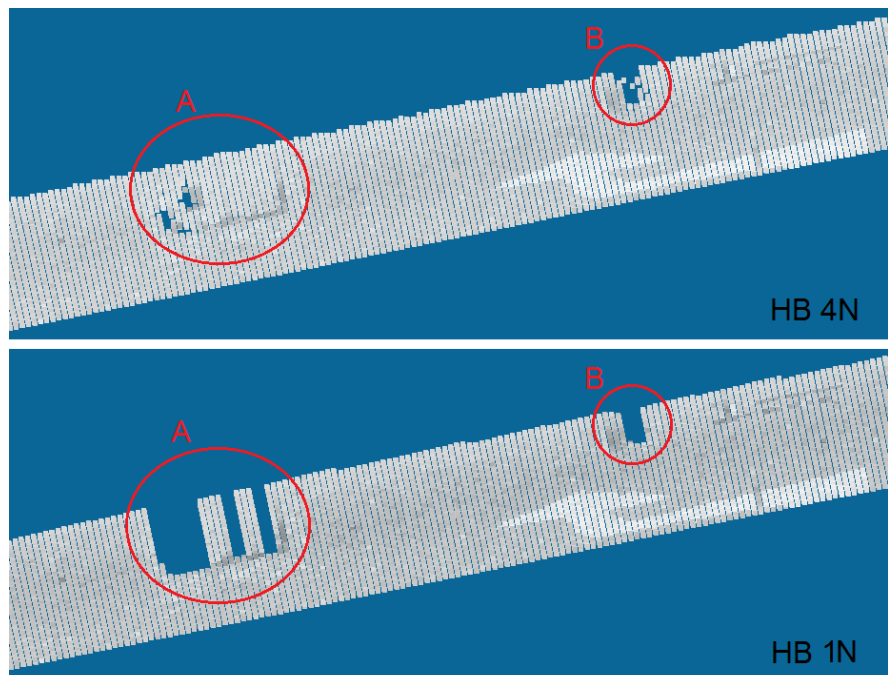


Figure 38. Comparison of 4N (top) and 1N (Bottom) region growing using HB variant regarding to the gap regions

Both variants have advantages and limitations. If there is low curbstone at the road boundary, 1N region growing has higher correctness compared to 4N region growing. If there is pothole or deep longitudinal cracks on the road surface 4N region growing performs higher completeness (Miraliakbari, et al., 2015) compared to 1N region growing.

The 1N region growing is more beneficial for the road surface extraction due to the following reasons:

- 1- Experimentally it is recognized that the chance of having low curbstones is more than having potholes and deep longitudinal cracks on the road, so, in one study area, the overshoot regions in 4N region growing is greater than the gap regions in 1N region growing.
- 2- As the manual editing after automatic process is always necessary, the manual separation of road surface from sidewalk in the point cloud data is much harder than filling the gap regions with the original input data.

### 5.1.2. Comparison of HDB and HB outcomes

The difference between HB and HDB outcomes is visible at the vehicle boundaries with the road surface. As explained in section 4.2.1, In HB variant, if there is one or more than one empty voxel between the non-empty voxels along the Z-axis, the region growing continues. At the car boundaries, the empty voxels are between the laser scanning points on the ground and on the car doors (Miraliakbari, et al., 2015). The location of empty voxels is shown with the red colour in the left subfigure of Figure 39. As the HB variant does not stop the region growing, the point clouds under the car chassis (shown with the green colour in right subfigure) will be detected as road surface.

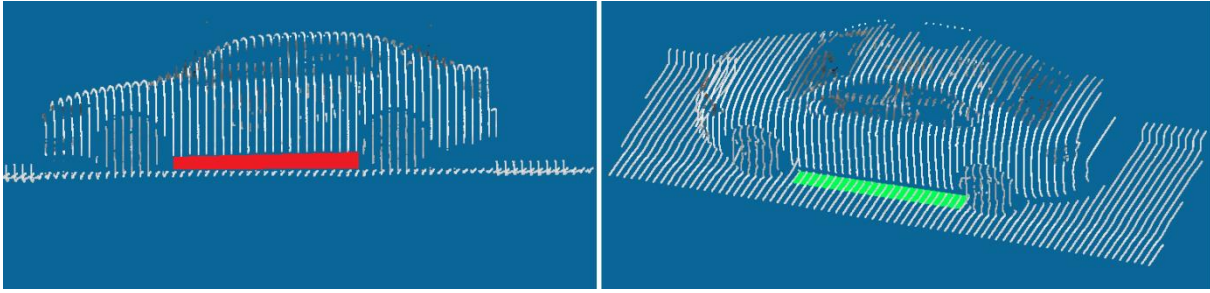


Figure 39. Empty space between car doors and road surface shown with red colour (left), laser scanning points under the car chassis shown with green colour (right)

Figure 40 shows the comparison of HB and HDB variants. The scene, input laser scanning data, region growing (4N) and the threshold (2 cm) are the same for both variants. Regarding the HDB variant, presence of the objects like car doors above the points of the pavement surface will stop the process because the variant considers the boundary of those objects as curbstone. Using HB variant the remaining laser scanning point cloud on the pavement surface and below the car chassis will be detected as road surface.

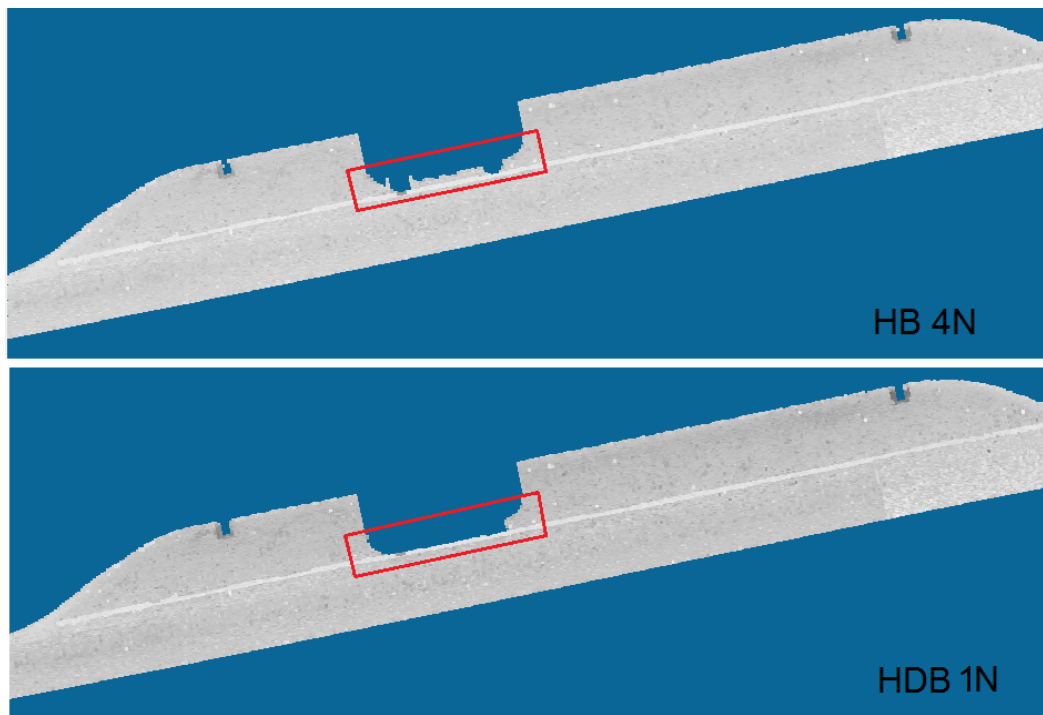


Figure 40. Comparison of HB (top) and HDB (bottom) variants

Although, there are not much differences between the HB and HDB results, the HB variant is more beneficial for the road boundary extraction, because it provides additional information about the objects located above the road surface. For instance, the empty space between the car chassis and road surface (Figure 39) produces empty voxels and can localize the car doors. As an outlook for improvement of road boundary extraction, this information will help to avoid detecting of car doors and reduce the commission error of the results.

### 5.1.3. Comparing the results using different thresholds

Proper thresholds are very essential for the termination of the road pavement surface extraction process. Figure 41 illustrates the outcomes of road pavement surface extraction by means of HB variant and 1N region growing using different thresholds. Upper left subfigure shows the input data, Upper right, lower left and lower right subfigures are the results of using 4cm, 2cm and 1 cm thresholds, respectively. As shown in the upper right subfigure, the result of road surface extraction using 4 cm threshold produces overshoot area (shown in the red circle). This failure is because of the existence of low curbstones at the road boundary of this region (Miraliakbari, et al., 2015). In the lower left subfigure, there is no overshoot region, however, it has marginally gap area surrounded by red circle. Selection of 1cm threshold produces frequently gap region which clarifies that this threshold is not suitable for the data processing.

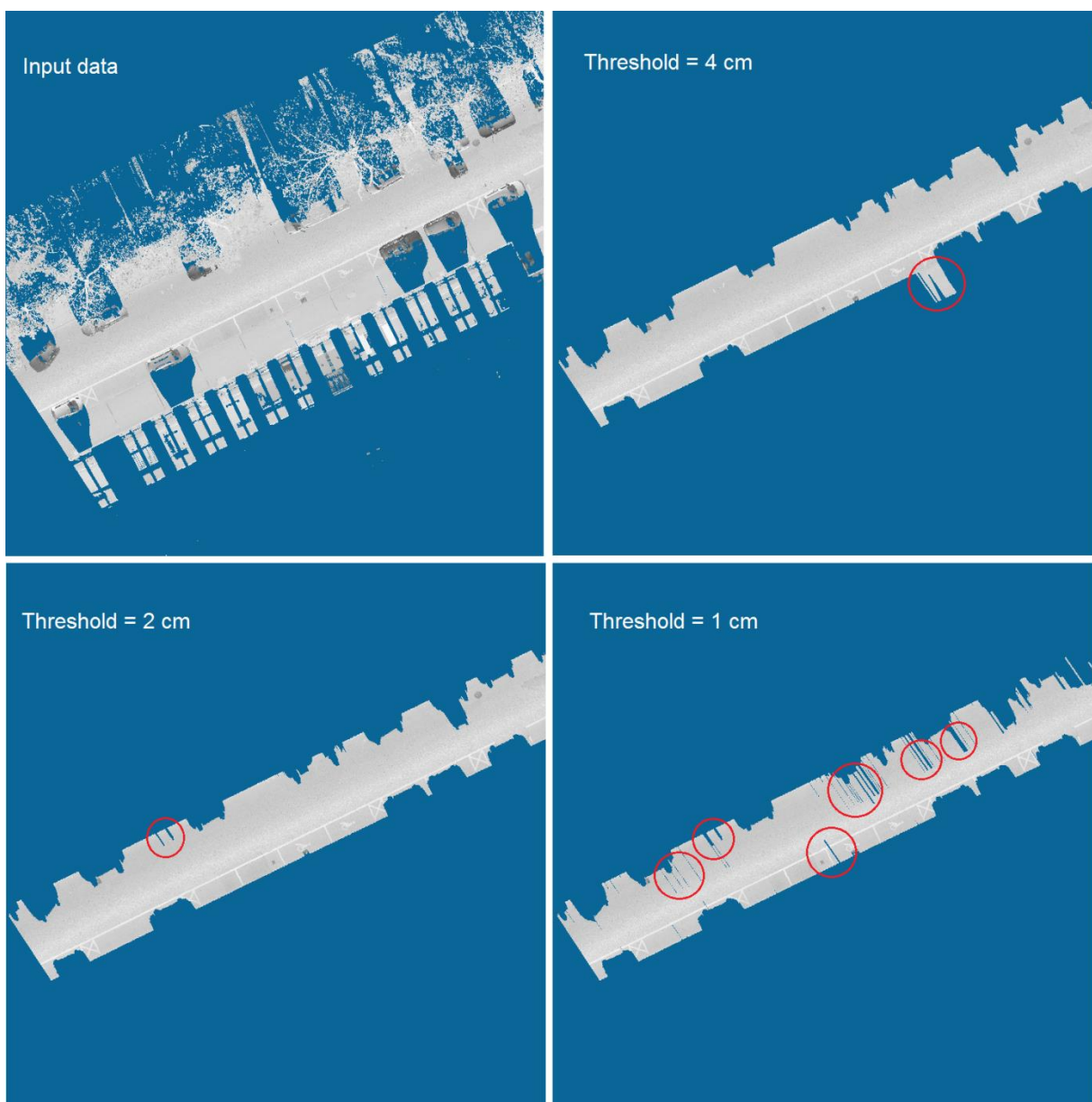


Figure 41. Comparison of road surface extraction using 4 cm (upper right), 2 cm (lower left) and 1 cm (lower right) thresholds, adapted from (Miraliakbari, et al., 2015)

The comparison of the results with different thresholds shows that a 2 cm threshold is appropriate to be chosen. It is rare to have less than 2 cm height difference between the curbstone and the road surface at the road boundary. On the other hand selection of lower threshold might end up having several false negative (FN) regions on the road surface. In the worst case when there is no curbstone at the road boundary, threshold selection does not play any role and there will be always false positive (FP) region.

#### 5.1.4. Accuracy assessment of the road surface extraction

In this section, the accuracy assessment of the results of road surface extraction using 1N region growing and HB variant is carried out. The threshold used for the termination of process is 2 cm. For validation purpose, the ground truth is extracted by manual digitizing of the road boundary using unprocessed laser scanning data. For accuracy assessment, completeness and correctness (Eq. ( 46 ) and Eq. ( 47 )) are calculated. Dataset A shown in Table 3 (section 3.6) is used for the accuracy assessment.

$$\text{Completeness} = \frac{\text{correctly detected road surface}}{\text{correctly} + \text{not detected road surface}} \quad (46)$$

$$\text{Correctness} = \frac{\text{correctly detected road surface}}{\text{correctly} + \text{falsely detected road surface}} \quad (47)$$

Figure 42 shows the result of accuracy assessment of road pavement surface extraction using HB variant and 1N regions growing. While the white region is the background, the omitted areas are represented in yellow colour, wrongly detected areas are shown in blue colour and brown region shows the correctly extracted road pavement surface. The percentages of completeness and correctness amount to 93.8 % and 94.9 %, respectively (Miraliakbari, et al., 2015).

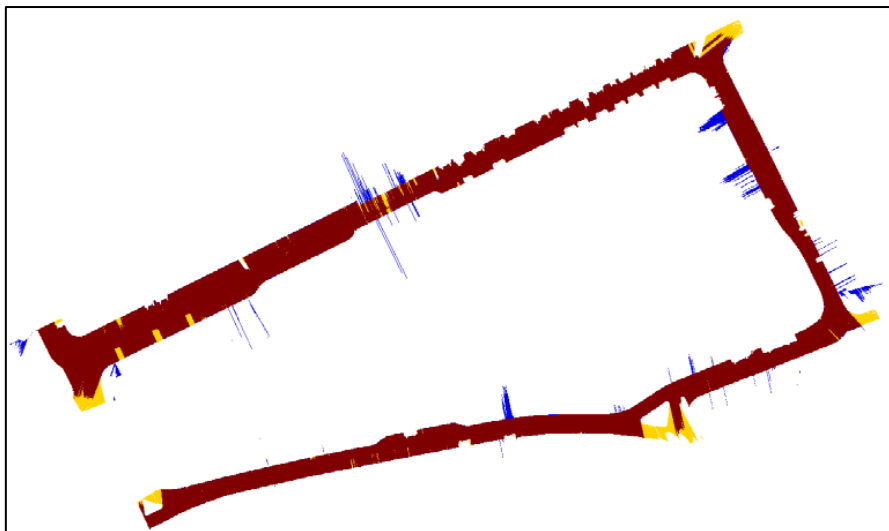


Figure 42. Accuracy assessment of road pavement surface extraction by means of HB variant and 1N region growing, adapted from (Miraliakbari, et al., 2015)

### 5.1.5. Road boundary extraction

Potential road boundaries are the cells which are located at the boundaries of extracted road surface. Due to the existence of obstacles (mainly cars), there will be regions which are wrongly detected as road boundary (Miraliakbari, et al., 2015). Figure 43 shows the boundary region of extracted road using 1N region growing for the HB variant. The threshold is set to 2cm for the road surface extraction. In this figure, the road boundaries include the wrongly detected regions such as car wheels and noise (outliers) such as the boundaries of gap (e.g. Figure 38 bottom) or end of overshoot regions (e.g. Figure 37 bottom).

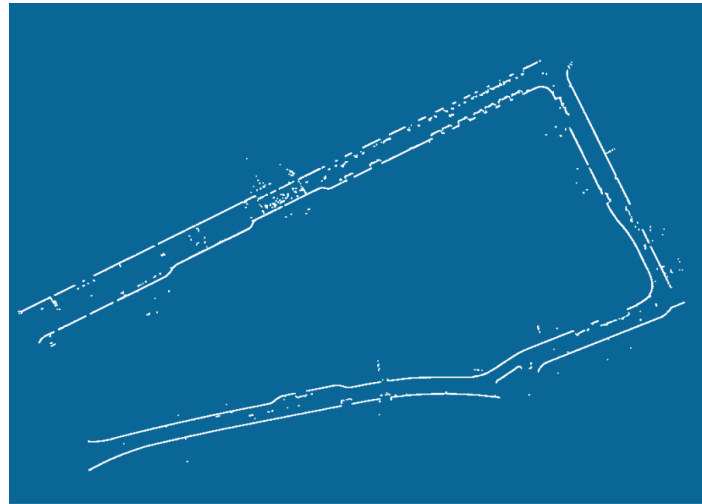


Figure 43. Potential road boundary cells including noise and wrongly detected regions

The noise removal and elimination of the wrongly detected regions is applied using geometric properties of area and roundness. Figure 44 shows the filtered result of potential road boundaries. For this sample, regions which have area smaller than  $50 \text{ cm}^2$  and roundness greater than 0.2 are eliminated.



Figure 44. Filtered result of potential road boundaries by means of area and roundness as geometric properties of the potential road boundary regions



The filtered result of potential road boundaries has several gaps and these gaps must be filled. The gap filling is applied by fitting 4<sup>th</sup> order spline to the filtered potential road boundary regions (Miraliakbari, et al., 2015). Figure 45 illustrates the result of road boundary extraction. Validation of the road boundaries show that only two regions which are shown with the red circles are wrongly extracted.

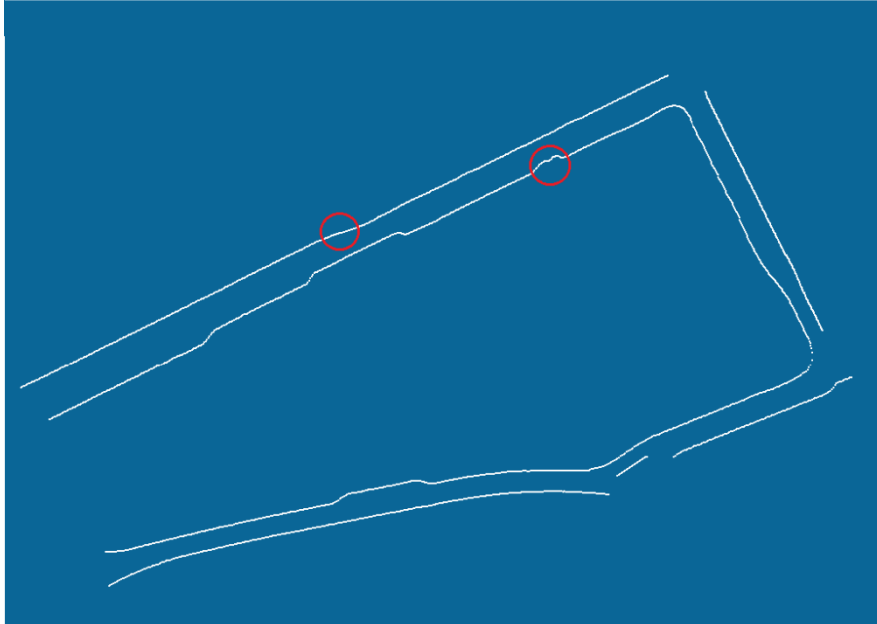


Figure 45. Result of road boundary extraction by connecting the filtered road boundary regions using fitting 4<sup>th</sup> order spline

Figure 46 shows closer view of these two regions and the real road boundaries (green lines). The wrongly extracted road boundary in the left subfigure is because of: first lack of data (filtered result) at this region and secondly the special shape of road boundary (L shape) at this area. In the right subfigure, the wrongly extracted road boundary is because of the existence of falsely detected road boundary regions which are not eliminated by the filtering criteria.



Figure 46. Comparison of falsely detected road boundaries with the ground truth

## 5.2. Rut detection

Results of three rut detection methods, namely: rut detection using 1D polynomial fitting, 1D cross-correlation and curvature are presented and discussed in the following subsections.

### 5.2.1. Rut detection using polynomial fitting on the scanlines

In this section two aims are investigated. The first aim is to find out which polynomial order is appropriate for the algorithm. Experiments with polynomial order 3 to 8 are carried out in this section. The second aim is to find out which iteration number is relevant for the algorithm. Finally, thresholded results of height difference between fitted polynomial and the scanlines are illustrated.

#### Defining proper polynomial order

The test area (white area in Figure 47) located at a parking place contains 428 scanlines on the road surface. This area is considered to find out which polynomial order is proper for the rut detection. The investigation is started with lower polynomial orders (3, 4 and 5). These three low order polynomial fitting onto a scanline are illustrated in Figure 48.

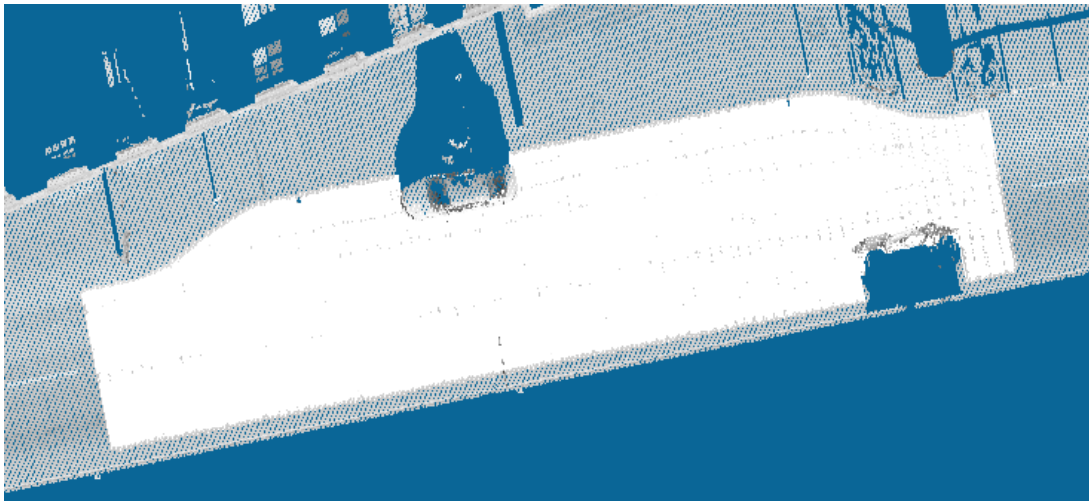


Figure 47. Study area for rut detection experimental investigation

The polynomial must fit onto the local maxima (rut supports) of the scanlines. The failures are shown with the red and yellow circles in both figures. The polynomial of 3<sup>rd</sup> order locates above local maxima of the scanline. The polynomial of 4<sup>th</sup> order has the same problem but less than polynomial of 3<sup>rd</sup> order. This problem is shown with the red circle. Although the polynomials of 4<sup>th</sup> and 5<sup>th</sup> order fit mostly on rut supports, but as shown with the yellow circles, the polynomial has sometimes concave shape between the rut supports. The concave shape results residual values (height difference between the polynomial and scanline) to be less than the residual values when a straight-line passes through the rut support. Based on the empirical experiences and as illustrated in these figures, the polynomial order 3, 4 and 5 are not well suited for the rut detection purpose.



The investigation continues for higher order polynomials namely: 6, 7 and 8 (Figure 49 and Figure 50).

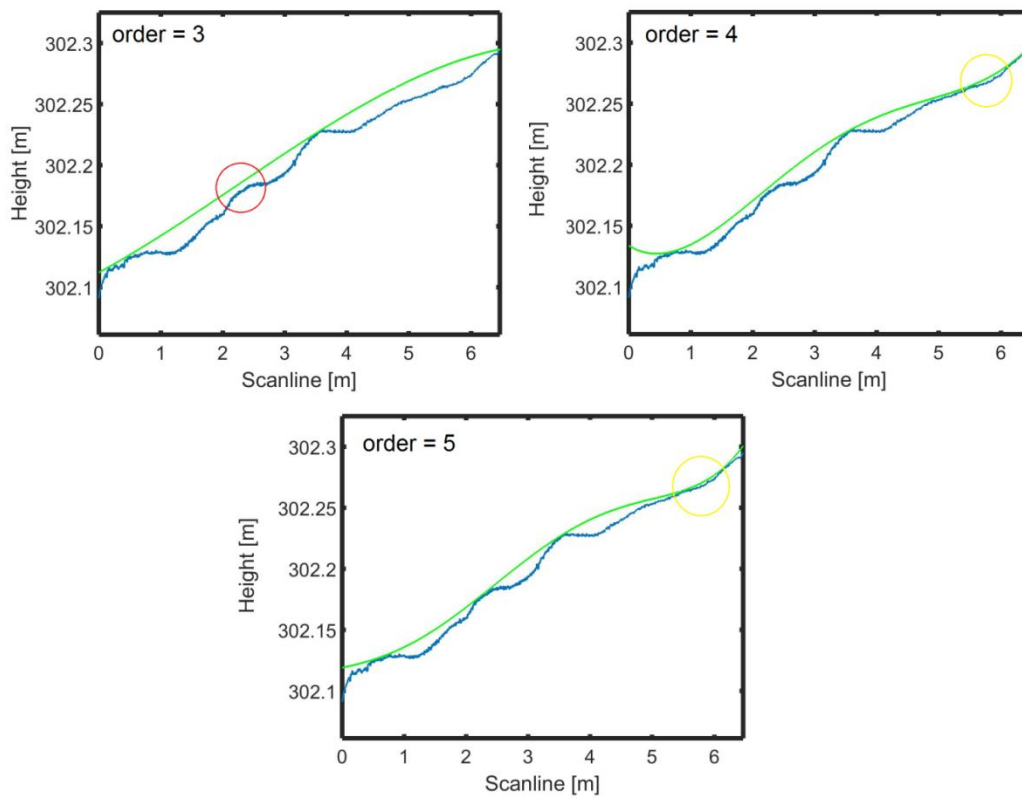


Figure 48. Results of polynomial fitting onto the scanline with polynomials of 3<sup>rd</sup> (top left), 4<sup>th</sup> (top right) and 5<sup>th</sup> order (bottom)

## 5. Laser scanning data processing, results and discussion

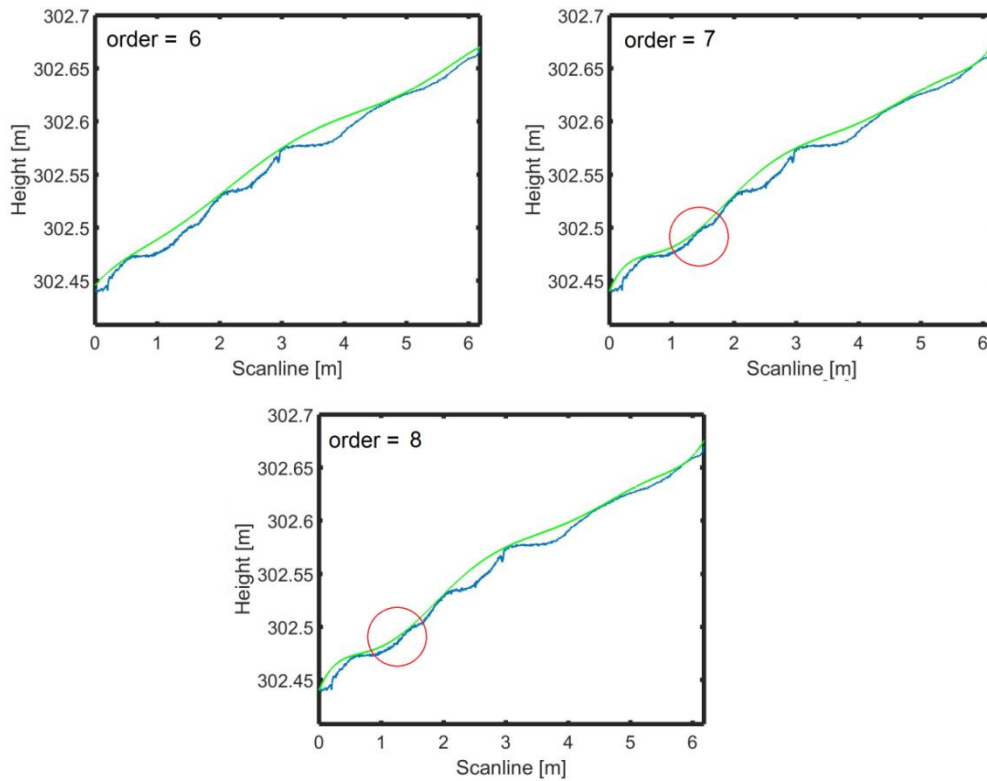


Figure 49. Results of polynomial fitting onto the scanline with polynomials of 6<sup>th</sup> (top left), 7<sup>th</sup> (top right) and 8<sup>th</sup> order (bottom)

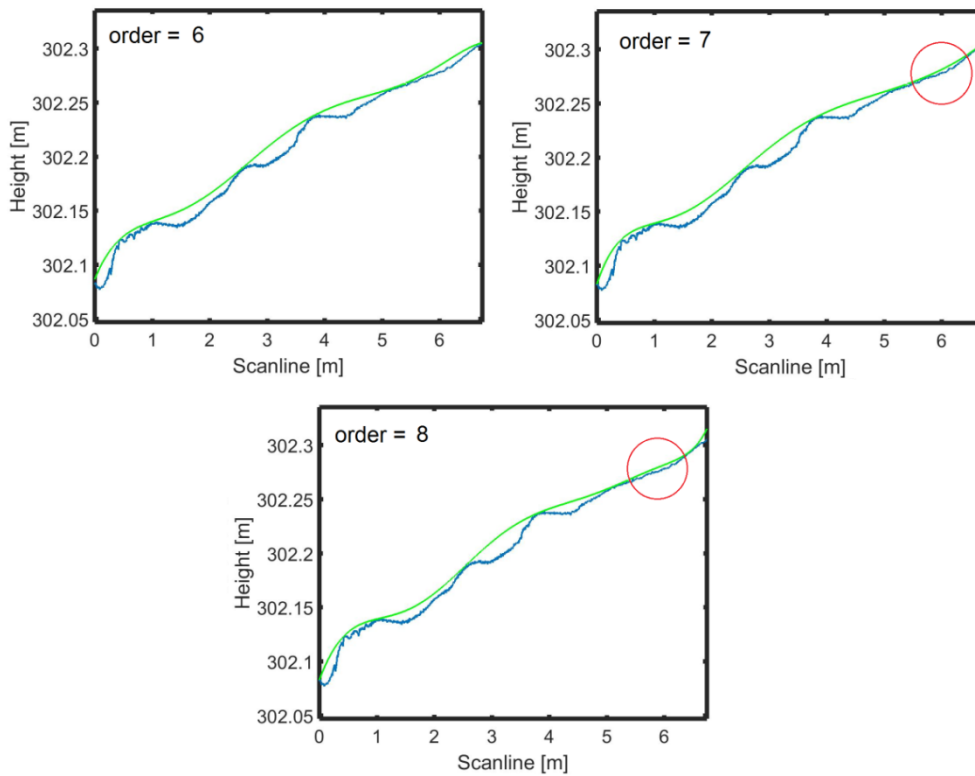


Figure 50. Results of polynomial fitting onto the scanline with polynomials of 6<sup>th</sup> (top left), 7<sup>th</sup> (top right) and 8<sup>th</sup> order (bottom)

As presented in Figure 49 and Figure 50, the polynomial fitting of 7<sup>th</sup> and 8<sup>th</sup> order sometimes feature strongly concave curved sections (shown with the red circles) between the local maxima of the scanlines. In the same way, overshoot is encountered at the margin of scanline for these orders of polynomial. The overshoot is mostly depends on the street shape and its variation in the cross section. Experimental investigation on several scanlines shows that polynomial of 6<sup>th</sup> order performs better results compared to the other polynomials, however, the overshoot at the margin of scanline is still the limitation of this order of polynomial.

Figure 51 visualizes the overlaid thresholded result of height difference between the fitted polynomials of 4<sup>th</sup>, 5<sup>th</sup> and 6<sup>th</sup> order and scanline. Hereafter, for the sake of simplicity, the height difference between fitted polynomial on the scanlines and the scanlines themselves is called “height residual”. This overlaid results in generating 7 classes. Brown region shows the intersection of results of all three polynomial orders (4<sup>th</sup>, 5<sup>th</sup> and 6<sup>th</sup>). Red, orange and green regions show the intersection of results of polynomials of 5<sup>th</sup> and 6<sup>th</sup>, 4<sup>th</sup> and 6<sup>th</sup>, and 4<sup>th</sup> and 5<sup>th</sup> orders, respectively. Yellow, cyan and blue regions are the remaining results of polynomials of 6<sup>th</sup>, 5<sup>th</sup> and 4<sup>th</sup> orders, respectively which have no overlapping with other results. The percentage of the class regions with respect to the total detected area is shown in Table 4.

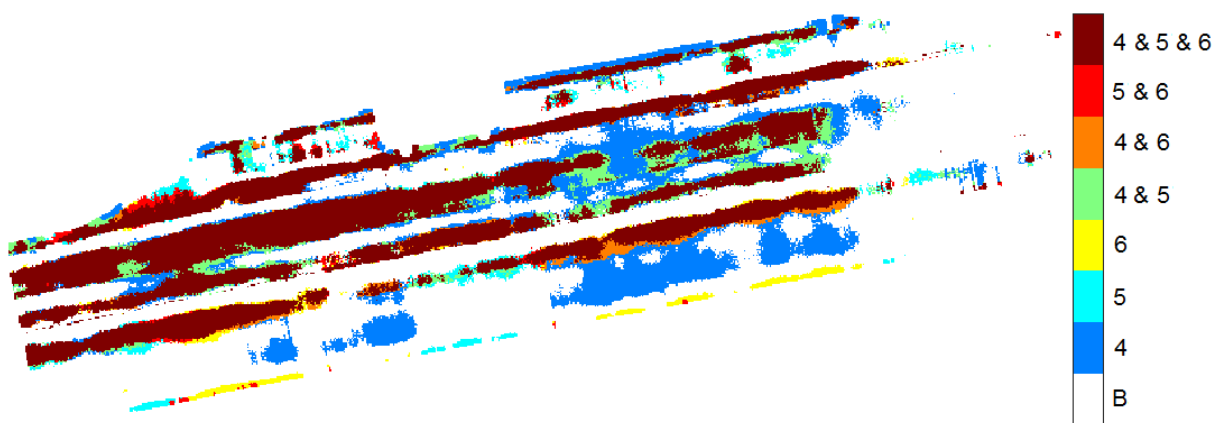


Figure 51. Overlaid thresholded results of height residuals of 4<sup>th</sup>, 5<sup>th</sup> and 6<sup>th</sup> order polynomials, the threshold value amounts to 1 cm

Order	4	5	6	4&5	4&6	5&6	4&5&6
%	26.1	3.7	2.7	8.4	2.5	1.8	54.5

Table 4. Percentage of class regions with respect to the total detected regions in Figure 51

These figure and table show that the polynomial fitting of 4<sup>th</sup> order allocates several parts of the street as rut regions. Comparison of the results of Figure 51 with the corresponding scanlines shows that in blue regions, the 4<sup>th</sup> order polynomial has concave shape and locates above the scanline, therefore the height residual exceed the threshold. The brown region occupies 54.4 % of the detected regions and is likely to belong to rut regions.

The same investigation is carried out for higher order polynomials and the results are shown in Figure 52 and Table 5.

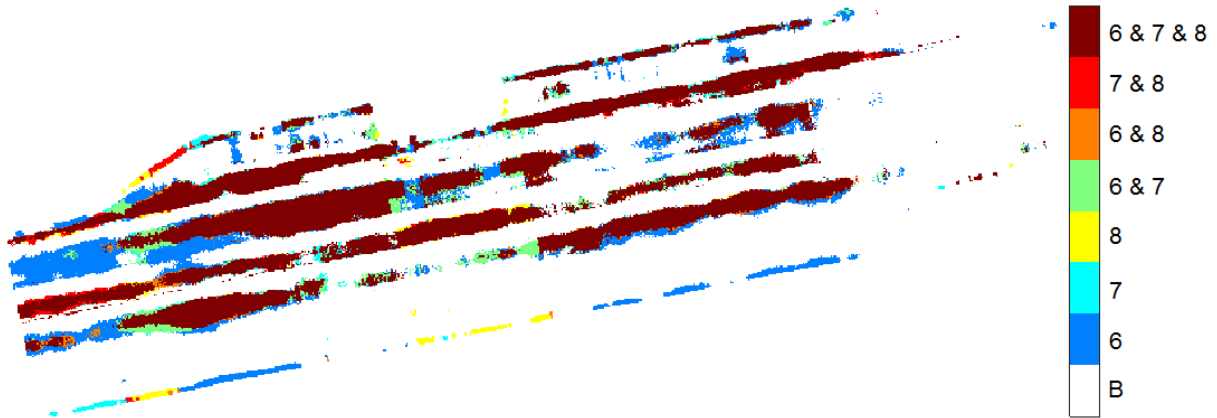


Figure 52. Overlaid thresholded results of height residuals of 6<sup>th</sup>, 7<sup>th</sup> and 8<sup>th</sup> order polynomials, the threshold value amounts to 1 cm

Order	6	7	8	6&7	6&8	7&8	6&7&8
%	21.8	2.4	1.9	6.1	1.6	2.3	63.4

Table 5. Percentage of class regions with respect to the total detected region in Figure 52

The brown region occupies 63.4 % of the total detected region and is likely to belong to rut regions. Polynomial fitting of 6<sup>th</sup> order assigns several parts of the street as rut regions which are not detected by the other fitted polynomials (blue region). Comparison of this region with the corresponding locations of cross section of 6<sup>th</sup> order polynomial and scanlines shows that, 6<sup>th</sup> order fitted polynomial does not feature convex curved but nearly straight-line sections between the local maxima of the scanlines. The only drawback of using 6<sup>th</sup> order polynomial is that it performs overshoot at the margin of scanline. It results in false detection of rut regions at the bottom of the test area (blue narrow areas at the bottom of Figure 52).

### Result of accuracy assessment

Definition of detected rut region:

$$Detected\ rut\ region = P(i) \in Scanline \vee H_{Polynomial}(i) - H_p(i) > thresh \quad (48)$$

where  $P(i)$  denotes the  $i^{th}$  scanline point on the road surface,  $H_{Polynomial}(i)$  is the height of  $i^{th}$  fitted polynomial point,  $H_p(i)$  is the height of  $i^{th}$  scanline point and  $thresh$  is the threshold of height residuals which is 1 cm.

Definition of detected rut region in ground truth:

$$Rut\ region\ in\ ground\ truth = P(i) \in Scanline \vee H_{Polygon}(i) - H_p(i) > thresh \quad (49)$$

where  $P(i)$  denotes the  $i^{th}$  point of the scanline on the road surface,  $H_{Polygon}(i)$  is the height of  $i^{th}$  digitized polygon point,  $H_p(i)$  is the height of  $i^{th}$  point of the scanline and  $thresh$  is the threshold of height residuals which is 1 cm.

The accuracy assessment is performed to confirm the usefulness of the polynomial of 6<sup>th</sup> order for rut detection. For validation, the traditional method of rut detection (laying straight edge across the rut) is simulated by digitizing the local maxima (rut supports) of the scanline and connecting them with straight-lines. The thresholded result of height difference between the digitized polygon and scanline is considered as ground truth. 20 scanlines with the incremental distance of 1 m are taken as ground truth data into account. Table 4 shows the percentage of recall (completeness), precision (correctness) and accuracy of the results of 4<sup>th</sup> to 8<sup>th</sup> order fitted polynomial. As shown in this table, result of 6<sup>th</sup> order fitted polynomial has the highest accuracy (Eq. ( 50 )) of 90.8 %. In the equation, TP and TN stand for true positive and true negative, respectively.

$$Accuracy = \frac{TP + TN}{TP + TN + FP + FN} \quad (50)$$

Polynomial order	4	5	6	7	8
Recall %	93.8	91.2	86.5	71.4	66.9
Precision %	57.5	65.5	73.3	71.9	77.6
Accuracy %	82.0	90.2	90.8	87.8	88.5

Table 6. Percentage of recall, precision and accuracy of the detected rut region using 4<sup>th</sup> to 8<sup>th</sup> order fitted polynomial

### Iteration

After selection of the proper polynomial, it is necessary to find out which iteration number is well suited for fitting the polynomial onto each scanline. To do that, two conditional statements for terminating the iteration are compared. In the first conditional statement, if the Route Mean Square Error (RMSE) of the height difference between the fitted polynomials in (i)<sup>th</sup> and (i+1)<sup>th</sup> iterations is smaller than  $\epsilon$ , the iteration will be terminated. In the second conditional statement, if the number of scanline points above the fitted polynomial is less than a small threshold (here the threshold is set to 1% of the total number of scanline points), the iteration will be terminated. Of course, the iteration number varies from one scanline to another due to the shape and undulation of the scanline. For comparison of these conditional statements, two scanline samples are examined (Table 7).

Conditional statement	Number of iteration		$\max(H_P - H_{Polynomial} \forall i)$	
	Sample 1	Sample2	Sample 1	Sample2
RMSE of the height difference between (i) <sup>th</sup> and (i+1) <sup>th</sup> iterations < $\epsilon$	343	344	0.5 mm	0.7 mm
number of scanline points above the fitted polynomial < 1%	128	165	1 mm	1.5 mm

Table 7. Comparison between conditional statements used for termination of iteration

The table shows that the first conditional statements results having more iterations, however, the highest distance of local maxima which locates above the fitted polynomial is less than 1 mm.

## 5. Laser scanning data processing, results and discussion

Moreover for the first condition, higher iterations do not change the location of the fitted polynomial (Figure 53).

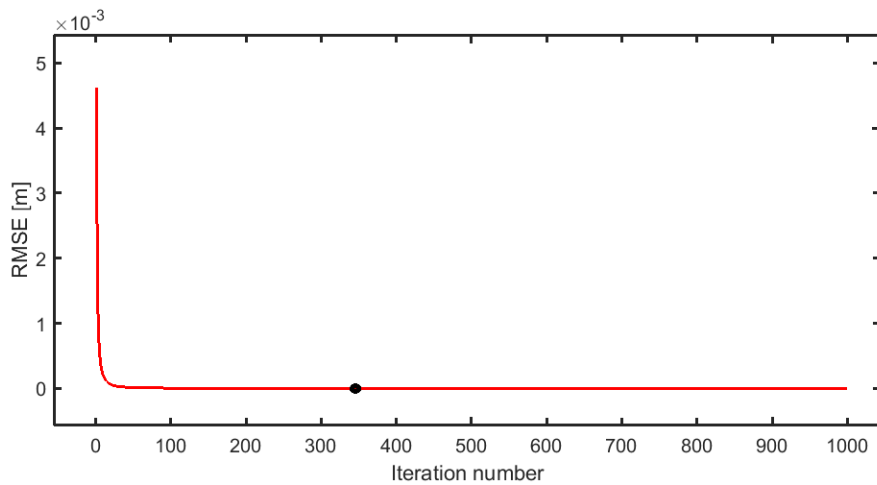


Figure 53. The RMSE of the height difference between  $(i)^{\text{th}}$  and  $(i+1)^{\text{th}}$  iterations of polynomial fitting onto the scanline, corresponding to sample1

The second condition may not be as robust as the first one, because if a rut supports contains small peak (shown with red circles in Figure 54) and the points on the peak are lower than the threshold (1 %), the fitted polynomial locates under this peak. Hence, the magnitude of calculated height residual will be smaller than in reality.



Figure 54. Schematic representation of peaks on rut support (uplifting of the sides of a rut)

Results of rut detection using 1D polynomial fitting are visualized in Figure 55. The utilized polynomial order amounts to 6 and first conditional statement is used for the termination of the iteration.

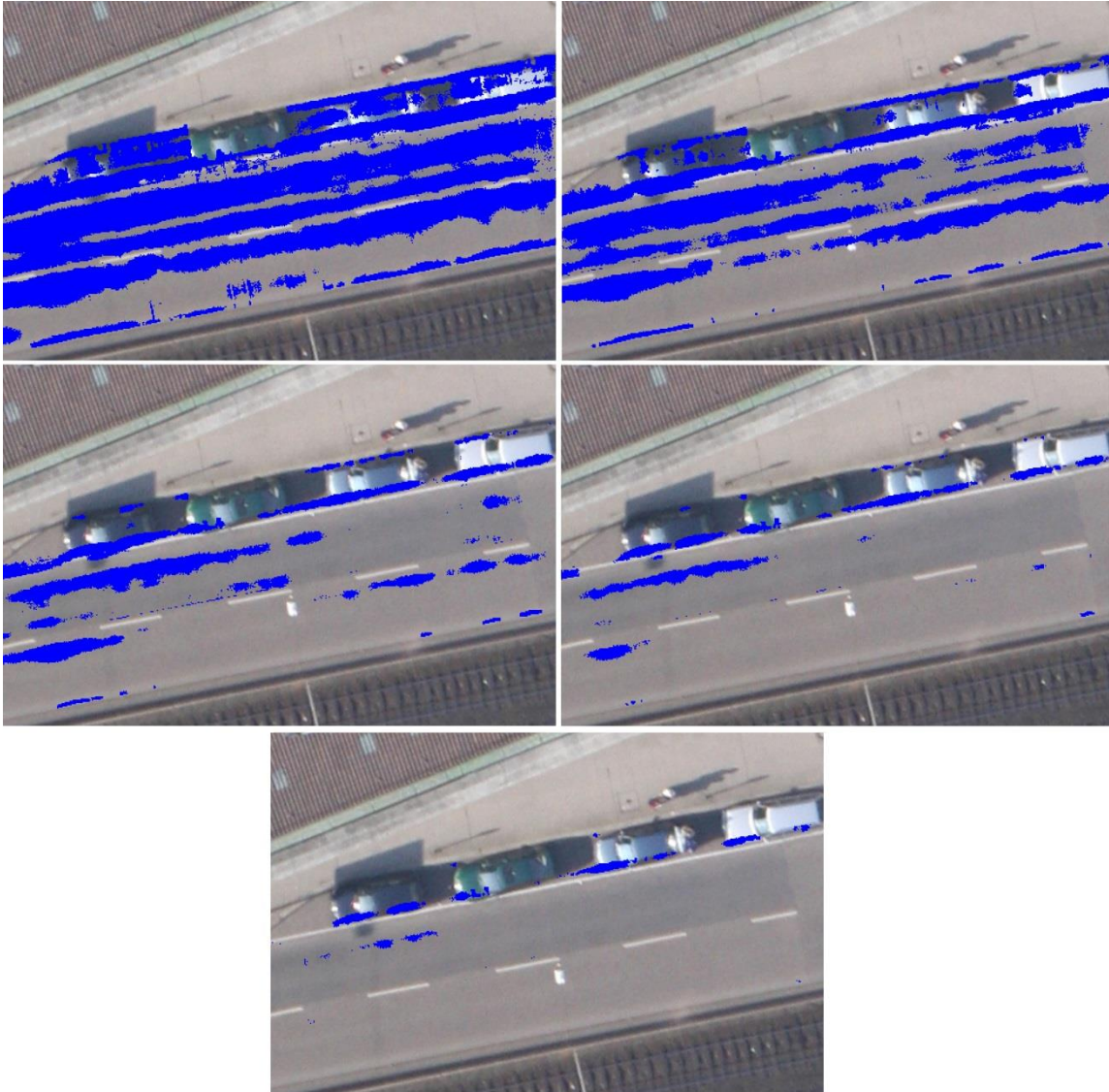


Figure 55. Result of rut detection using 1D polynomial fitting; the blue regions indicate the height residuals based on the following thresholds: 0.5 cm (top left), 1.0 cm (top right), 1.5 cm (middle left), 2.0 cm (middle right) and 2.5 cm (bottom)

The blue regions of the top left subfigure that represent the height differences greater than 0.5 cm occupy most of the road segment. It shows that the cross profile of the road has a lot of unevenness within the range of 0.5 cm. The blue regions shown in this subfigure are presented parallel with the driving direction. The big area of the blue regions shows that the depressions are wide and not necessarily deep. Next subfigure (top right) shows that choosing greater threshold cases having smaller blue regions (rutting areas). The last subfigure (bottom) shows that the deepest ruts are located mostly at the parking area of the street segment. It is because, the stand traffic load in this area is more than the other regions of the street segment.



### 5.2.2. Rut and potential rut detection using 1D cross-correlation

The aim of this section to find out which template width and correlation threshold are well suited for rut and potential rut detection. For this comparison, two input data are used, namely: original scanlines and the height residuals using polynomial of 6<sup>th</sup> order. The comparison is carried out by validation of the template matching results using template widths of 40 cm, 60 cm and 80 cm. The selection of template width is based on the typical rut widths on the road. The utilized correlation thresholds are 0.5, 0.6, 0.7 and 0.8.

Definition of detected rut point:

$$Detected\ rut\ point = P(i) \in Scanline \ \forall \ correlation\ coeff.(i) > thresh \quad (51)$$

Table 8 and Table 9 show the percentage of detected rut points which are inside the rut region in ground truth using height residuals and original scanlines as input data for template matching, respectively. As shown in both tables, the correctly detected rut points have the highest rate using template width of 40 cm and correlation threshold of 0.8.

Correlation coef.	Width = 40 cm	Width = 60 cm	Width = 80 cm
> 0.8	83.95	75.35	70.17
> 0.7	72.95	70.17	69.14
> 0.6	67.06	65.63	65.86
> 0.5	63.42	60.84	61.63

Table 8. Percentage of detected rut points which are inside the rut region in ground truth (Input data for template matching: height residuals)

Correlation coef.	Width = 40 cm	Width = 60 cm	Width = 80 cm
> 0.8	94.43	76.07	32.76
> 0.7	87.09	80.52	54.93
> 0.6	80.21	75.90	59.46
> 0.5	73.27	73.68	68.49

Table 9. Percentage of detected rut points which are inside the rut region in ground truth (Input data for template matching: original scanlines)

Figure 56 and Figure 57 compare the result of rut detection using cross-correlation and polynomial fitting of 6<sup>th</sup> order. The input data used for template matching are height residuals and original scanlines in Figure 56 and Figure 57, respectively. In both figures, the white region (background) is the intact pavement surface. Class 1 and class 3 illustrate the detected rut regions using polynomial fitting of 6<sup>th</sup> order. For the detection of rut regions, the threshold applied for the height residuals (Eq.( 48 )) amounts to 1 cm. Class 2 and class 3 show the detected rut points using cross-correlation. Class 3 depicts mostly the middle of the ruts which are detected by polynomial fitting.



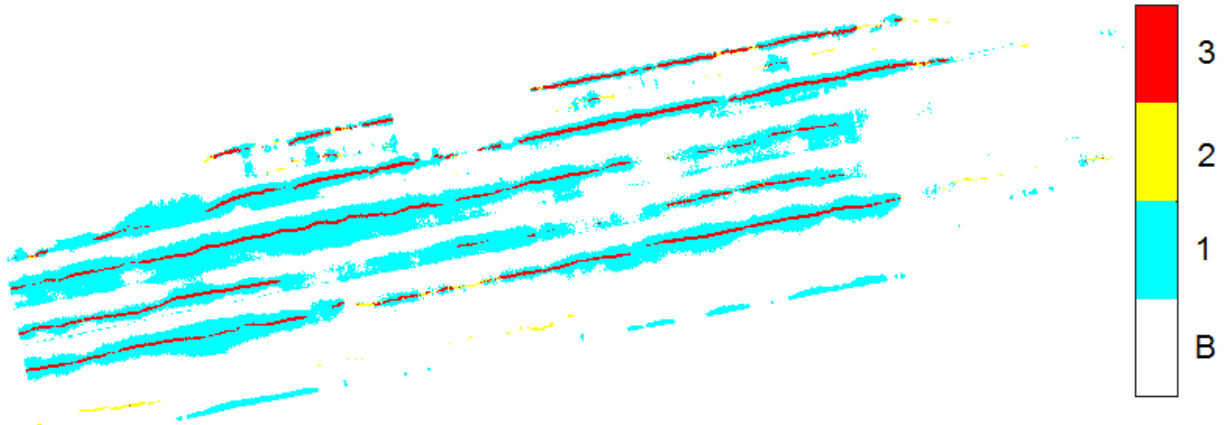


Figure 56. Comparison of detected rut region using cross-correlation (template width = 40 cm and correlation threshold = 0.8) and polynomial fitting of 6<sup>th</sup> order, input data for template matching is “height residuals”,

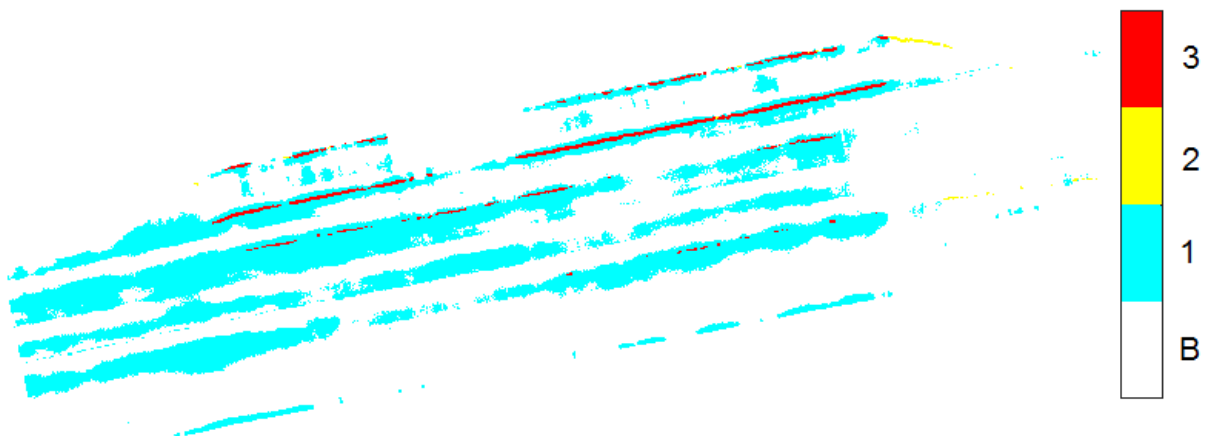


Figure 57. Comparison of detected rut region using cross-correlation (template width = 40 cm and correlation threshold = 0.8) and polynomial fitting of 6<sup>th</sup> order, input data for template matching is “original scanlines”

### Comparison of input data for template matching

The detected rut points by cross-correlation (class 2 + class 3) occupy more area in Figure 56 than in Figure 57. If the input data is the height residuals, cross-correlation detects more rut points. This is because the template matching is dependent of the inclination of the input data. In the study data, the road surface has lateral slope which varies from 1.3° to 2.0° and consequently, ruts might also get lateral slope. This lateral slope weakens the template matching (Figure 57) because the semi- major axis of the template has inclination angle of 0°. As the slope angle of height residual data is 0, the template matching performs appropriately and detects more rutting points. Figure 58 illustrates cross section of an exemplary scanline (left) and its height residuals (right) shown with blue profiles. As expected, the highly correlated parts of the profiles which are illustrated with red colour appear more in the right subfigure. Therefore, it is recommended to use the height residuals as input data for cross-correlation.

## 5. Laser scanning data processing, results and discussion

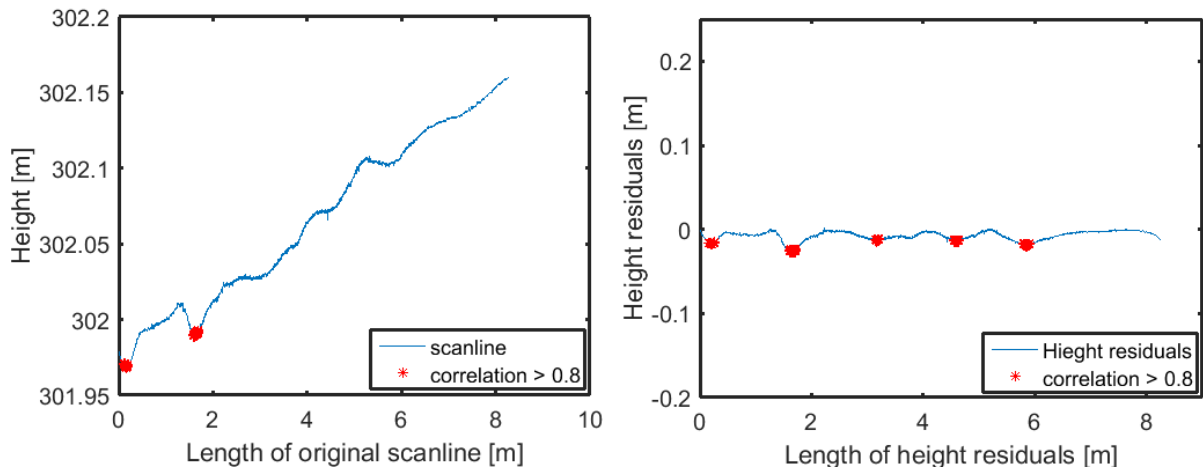


Figure 58. Cross-correlation-based rut detection using original scanline with the lateral slope of ca.  $1.4^{\circ}$  (left) and using height residuals (right)

### Comparison of the rut detection using cross-correlation and polynomial fitting

In Figure 56, the detected rut points using cross-correlation (class 2 + class 3) occupy quite narrow regions compared to the polynomial fitting results (class1 + class 3). The detected rut points are located at the middle of the ruts (see Figure 56 and right subfigure of Figure 58). The existence of class 2 shows that high correlation also presents partially at other locations with minor height residuals (less than the threshold of 1 cm) which means that the cross-correlation does not depend on the depth of the rut. This is partially because of presence of the STD of ‘windowed road section’ in the ‘denominator of correlation coefficient’. Therefore, the correlation coefficient will be independent from the depth of any depression. As a result small depressions on the road pavement surface can have significant correlation value (Miraliakbari, et al., 2014). In this study, these locations (class 2) are called “potential rut” which their depth will increase by the time.

In contrast to polynomial fitting, cross-correlation has the advantage that it localizes the local minima of the scanline profile e.g. middle of the ruts. Hence, deepest part of the ruts can be detected using 1D cross-correlation. Another advantage of cross-correlation is that it localizes the potential ruts and predicts the location of future ruts as additional information for rehabilitation procedure. The limitation of cross-correlation is that it cannot judge about the severity degree of rutting because rut depth cannot be measured by this method.

### 5.2.3. Rut detection using curvature

Figure 59 shows the result of estimated curvature along the scanlines. The negative curvatures are mostly located at the border of rut with the intact pavement surface. Higher curvatures are located near the parking place of the street. Apart from the parking area, several yellow longitudinal lines are visible along the street which declares the existence of transvers unevenness across the road.

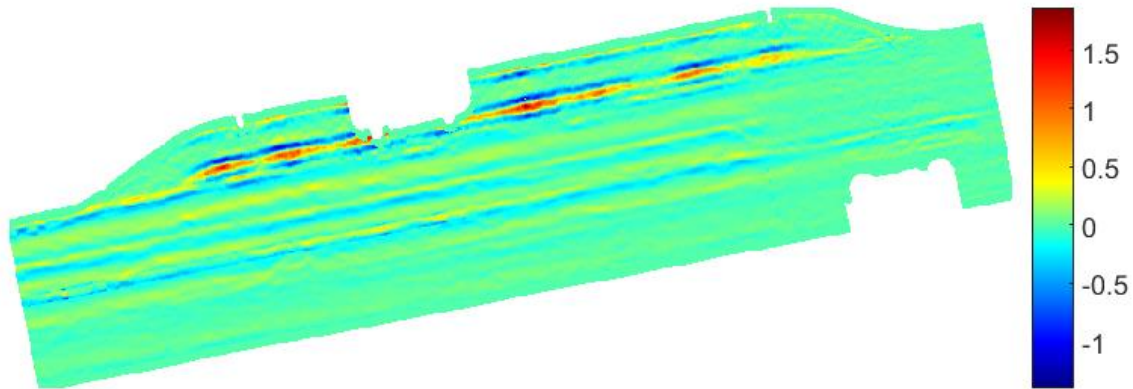


Figure 59. Estimated curvature along the scanlines

As cross section of the rut has certain curvature, for rut localization, a threshold for the curvature is considered ( $k_{thresh}$ ). The threshold selection is based on the width and depth of a typical rut. The regions which their curvature exceed the threshold are identified as rut regions. If the threshold is high, only small regions will be identified as rut regions. According to Eq. ( 12 ) in section4.3.3,  $k_{thresh} = 1/2$  is the selected threshold which indicates the curvature of the ruts with 1cm depth and 40 cm width. In Figure 60, comparison between the rut detection results using polynomial fitting and curvature is illustrated.

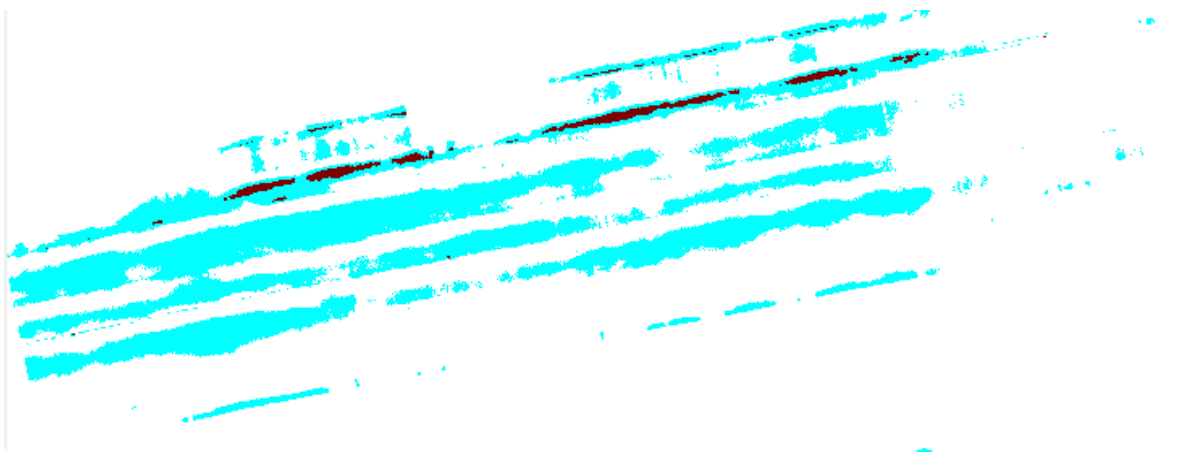


Figure 60. Comparison of rut detection results using polynomial fitting with the threshold of 1 cm (cyan regions) and curvature with the threshold of  $k_{thresh} = 1/2$  (brown regions)

The cyan regions occupy more area than the brown regions and this area difference clarifies the limitation of the rut detection using curvature. The rutting regions which are wider than 40 cm and

## 5. Laser scanning data processing, results and discussion

shallower than 1 cm are not detected due to their lower curvature, however, these regions are fairly recognized by means of polynomial fitting. In Figure 61, although both red and black ruts are deeper than 1 cm, the red one is wider and has lower curvature compared to the black one.



Figure 61. Schematic view of the curvature difference between two ruts (shown in red and black)

By reducing the  $k_{thresh}$  e.g.  $2/9$  i.e. curvature of a rut with 1cm depth and 60 cm width or  $1/8$  which shows curvature of a rut with 1cm depth and 80 cm width, the chance of detecting wider ruts will be higher. Nevertheless, the shape of the rut is also important. If the middle of the rut is flat, the curvature amounts to zero and only the sides of the rut (shown in Figure 62 with yellow circles) show up in the detection results because of having significant curvature.

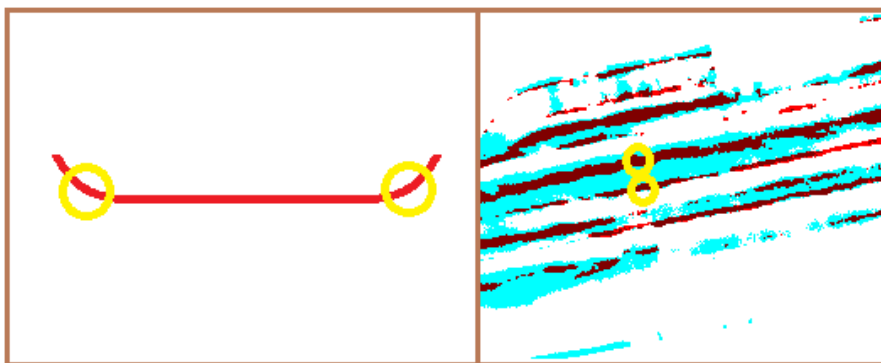


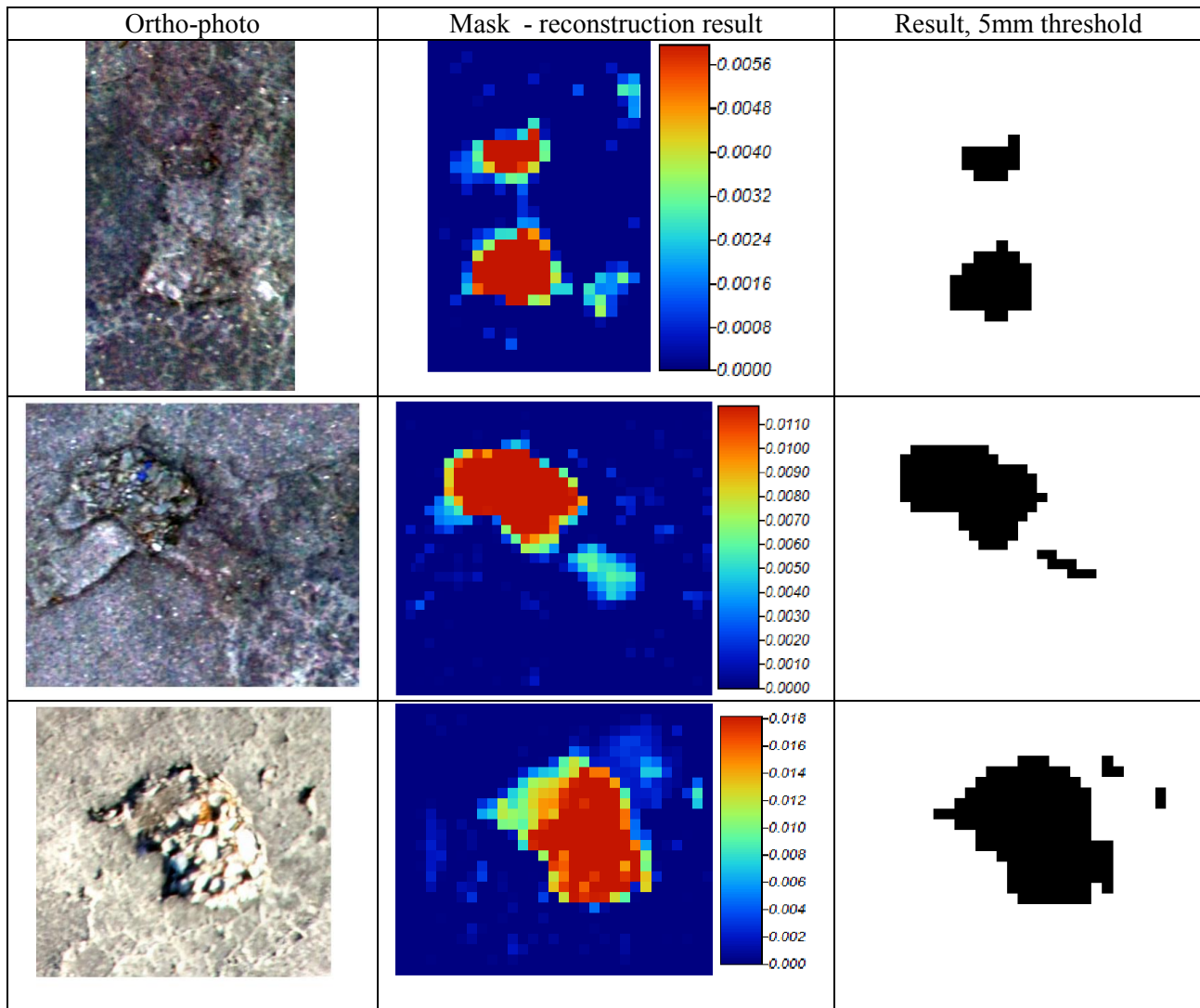
Figure 62. Left subfigure: schematic view of a cross section of a rut; the middle of the rut is flat, right subfigure: comparison of rut detection results using polynomial fitting with the threshold of 1 cm (cyan regions) and curvature with the threshold of  $k_{thresh} = 1/8$  (brown regions)

### 5.3. Pothole detection

On the city avenues in Germany, potholes are normally fixed faster than other distresses, therefore, it is relatively challenging to find potholes in the test regions described in section 3.6. This section aims to present and discuss the result of pothole detection using geodesic image reconstruction and 2D polynomial approximation onto the mobile laser scanner data.

### 5.3.1. Pothole detection using geodesic image reconstruction

5 captured samples of potholes are shown in the left column of Figure 63. Geodesic image reconstruction according to section 4.4.1 requires a regular grid. Therefore, the point cloud is interpolated to a height raster. In order to have a proper approximation of the boundary of the potholes, a 1 cm grid size is used. For geodesic image reconstruction, an offset of 2 cm between the marker and mask is applied. The regions detected by subtracting the height raster from the reconstruction result can be seen in the middle column of Figure 63 (the depth is shown in meter unit). If the surface of the road is broken, holes of more than 5 mm depth will be quickly detected. The 5mm depth is considered as threshold for generating a binary image from subtraction results which contains pothole and non-pothole regions (Figure 63 right column).



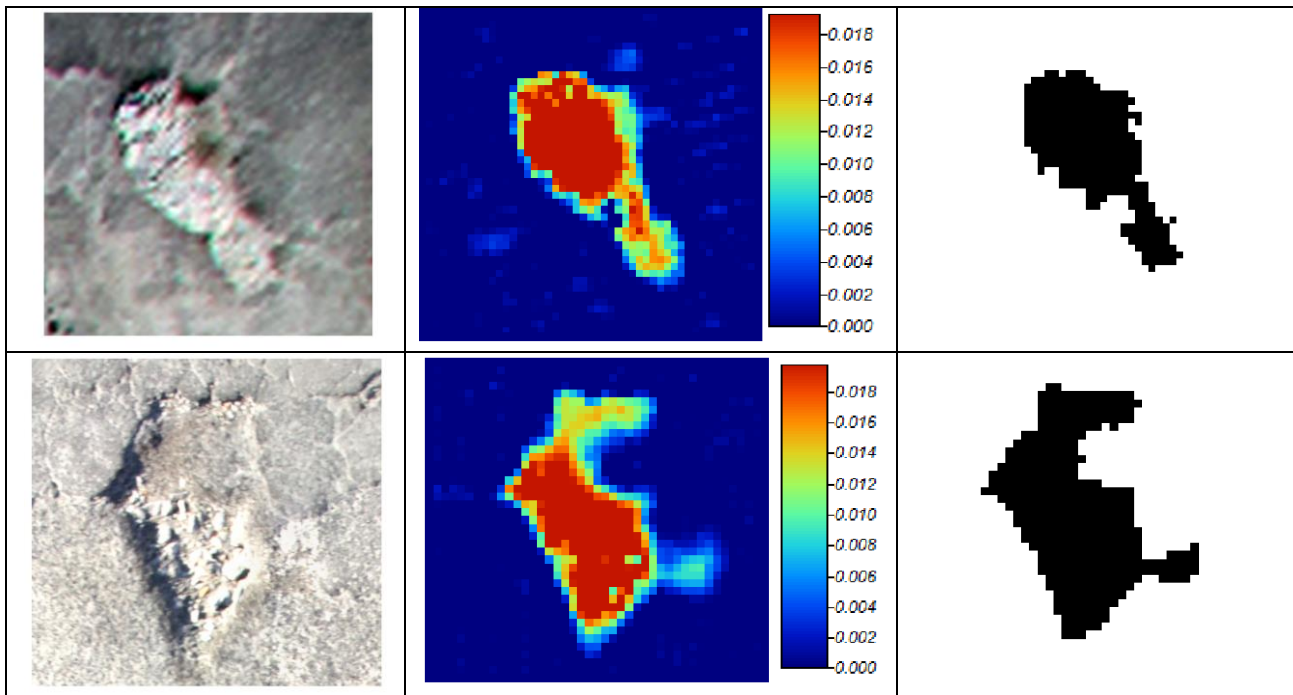


Figure 63. Result of pothole detection using geodesic morphological reconstruction. Ortho-photo of the pothole region is shown in the left column. Middle column illustrates the subtraction of the reconstruction result from the height raster (mask). Right column shows the binary image containing pothole (black region) and non-pothole region using 5 mm threshold

### 5.3.2. Pothole detection using 2D polynomial fitting on the laser scanning data

For pothole detection using 2D polynomial fitting, the test data used in previous section is considered in this section as well. Based on the experiments, the bi-variate polynomial of 5<sup>th</sup> order is selected for pothole detection. After fitting polynomial onto the pothole region, the height of the surface is subtracted from the height of polynomial. The threshold of 1 cm divides the area into pothole and non-pothole region. Thresholded result of subtraction which shows the pothole region is illustrated in the right column of Figure 64.



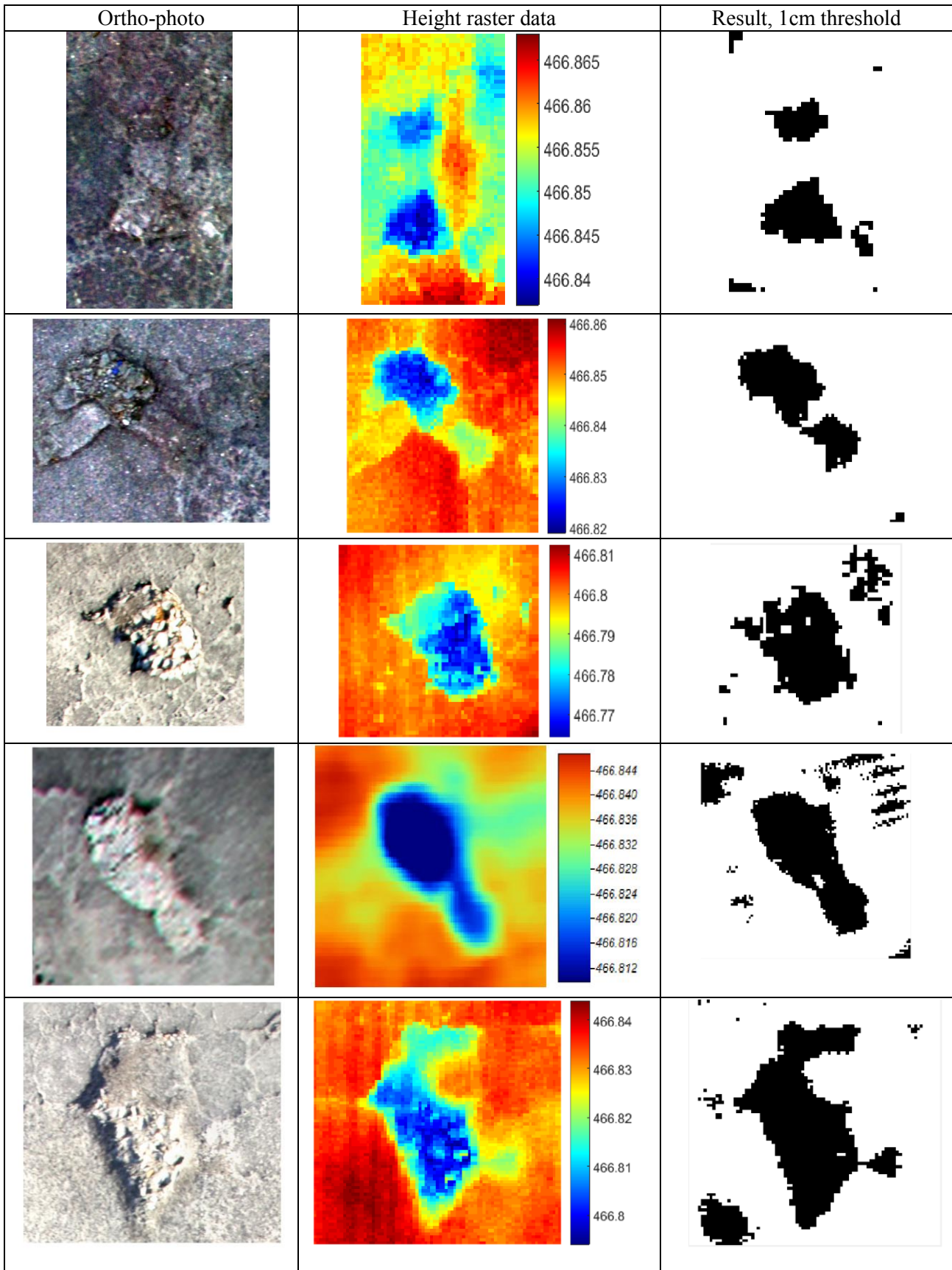


Figure 64. Result of pothole detection using 2D polynomial fitting. Ortho-photo of the pothole region is shown in the left column. Middle column illustrates the corresponding height raster of the pothole region. Right column shows the binary image containing pothole (black region) and non-pothole region using 1cm threshold

## 5. Laser scanning data processing, results and discussion

### **Comparison of pothole detection using geodesic image reconstruction and 2D polynomial fitting**

Both methods detect the pothole regions and separate them from the intact pavement surface. The major difference between the results of proposed methods is that using 2D polynomial fitting, some minor regions are falsely detected as pothole at the margins of the image clips. This is due to the overshoot which is encountered for bi-variate polynomial of 5<sup>th</sup> order.



## 6. Camera data processing, results and discussion

In this chapter, the experimental investigation on crack and path detection using camera data is reported. Two of the major road failures are cracks and patches. Density and frequency of the cracks and patches are significant indicators for road condition assessment. According to (IFI, 2014) the evaluation of road condition consists of a weighted average of parameters such as unevenness, cracking area, rut depth, etc. Compared to the mentioned road distresses, highest weight belongs to the alligator cracks. Such high weight confirms the importance of cracks in road condition mapping (Miraliakbari, et al., 2014), (Miraliakbari & Hahn, 2014). Cracks and patches are two distresses on the road which are detectable in RGB images because their reflectivity is different from the intact pavement surface. The RGB images used in this study are well suited for crack detection as their ground resolution amounts to ca. 1mm to 1.5mm (Miraliakbari, et al., 2016).

### 6.1. Crack detection

Cracks appear regularly as dark, narrow and linear structures in the images. Moisture in the cracks regions increases the dark representation of the cracks. Using high image resolution (1mm or 2mm) even narrow cracks can be visible in the images (Miraliakbari, et al., 2016). Results of filtering techniques for crack detection are outlined in the next subchapters.

Figure 65 illustrates the typical pavement crack histogram. The highest peak in the histogram belongs to the intact pavement surface. Such surface contains bitumen and aggregates. Experimentally can be seen that mostly pixels with low grey-values indicate the cracks regions (Miraliakbari, et al., 2014) , (Miraliakbari & Hahn, 2014). The problem is that by simple thresholding, crack pixels cannot be detected very well.

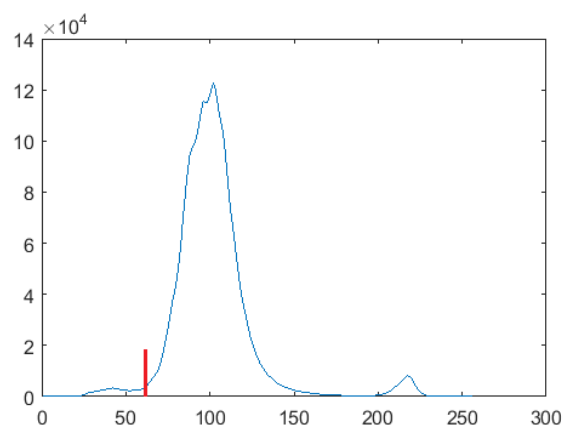


Figure 65. Pavement image histogram containing cracks (the threshold is represented with the red line)

For crack detection, the three filtering methods discussed in subsection 4.5, namely LF, HPF and MLBP are tested, analysed and compared with each other. The dataset used for crack detection is a stream of mobile images taken from Canon 5D Mark II. For the comparative evaluation of pavement crack detection using these three methods, 20 image samples are selected among the whole dataset used for crack detection. These 20 samples consist of linear, block and alligator (fatigue) cracks. Ground resolution of the images approximately amounts to 1mm to 1.5 mm (Miraliakbari, et al., 2016). Figure 66 illustrates 12 samples of image data.

## 6. Camera data processing, results and discussion



Figure 66. 12 image samples including linear, block and alligator (fatigue) cracks (Miraliakbari, et al., 2016)

### 6.1.1. Crack detection using LF

A proper window size used in this section amounts to  $21 \times 21$  pixels (Miraliakbari, et al., 2016). Figure 67 (right) shows 18 quadratic masks with the incremental angle of  $10^\circ$ .

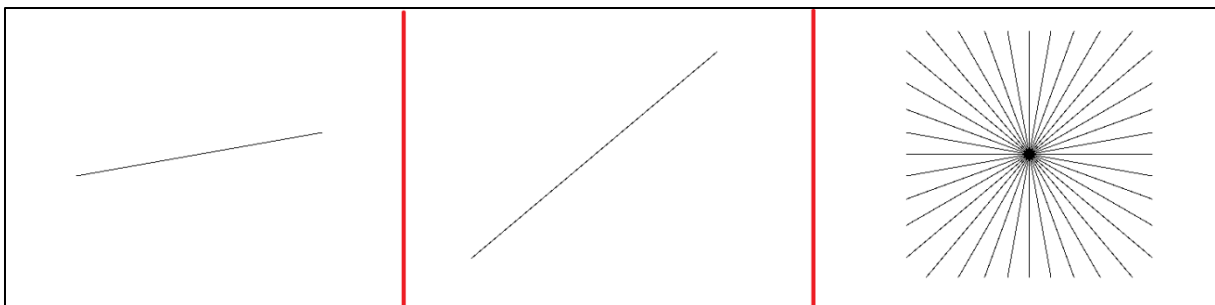


Figure 67. First quadratic mask (line filter) with angle of 10 (left), fifth quadratic mask with angle of  $50^\circ$ , superimposed 18 quadratic mask with the incremental angle of  $10^\circ$

**Investigation on Level of detail (LOD)**

LF is carried out on four LODs and proceeds from the coarsest level (1/8) to the finest level (1/1). The main reason of using different LODs is to detect potential cracks which have different widths (Miraliakbari, et al., 2016). Figure 68 shows results of detected cracks on the four resolution levels. The figure shows the original image containing cracks (top), detected potential crack pixels on 8 mm (middle left), 4 mm (middle right), 2 mm (bottom left), 1 mm (bottom right).

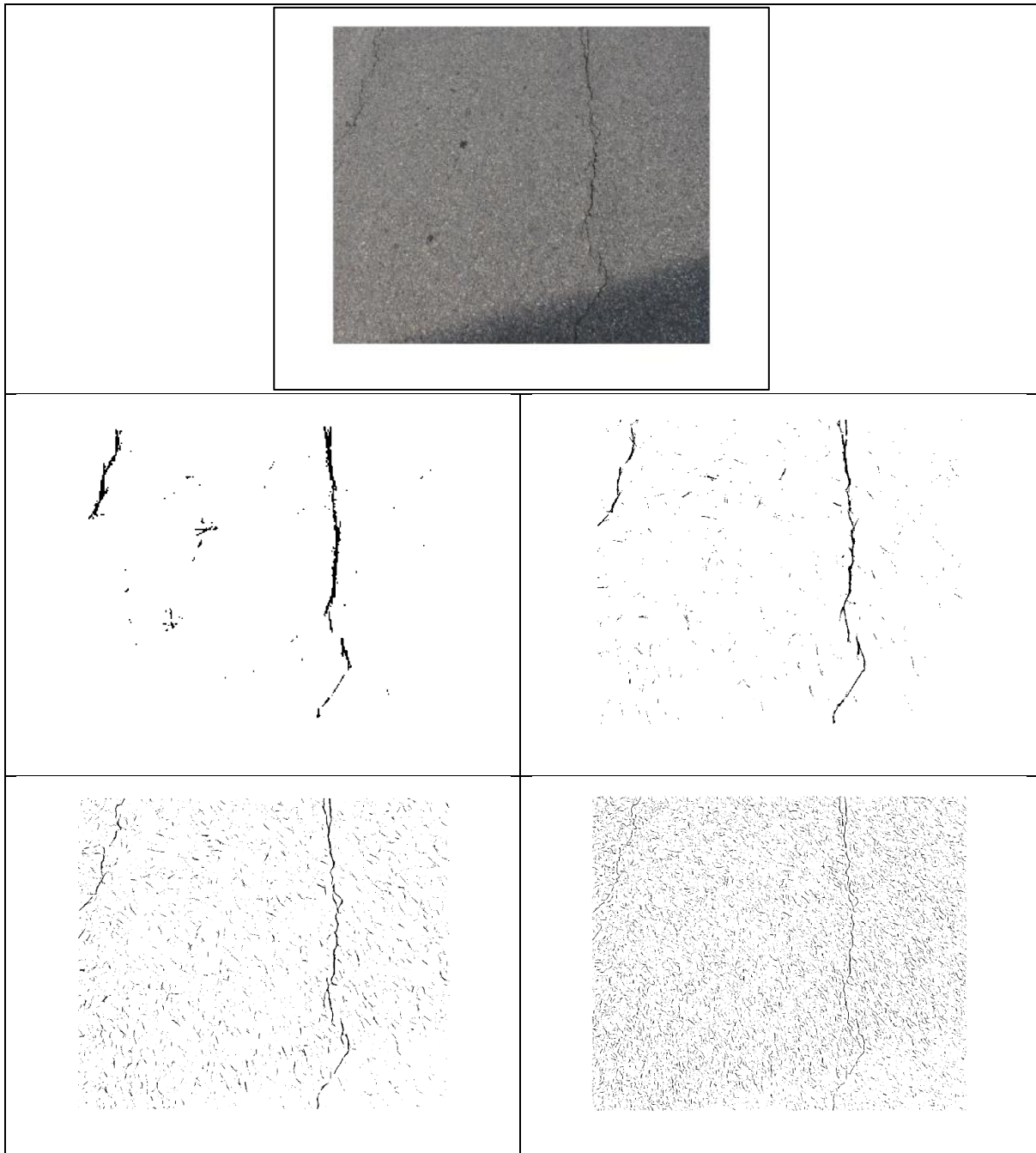


Figure 68. Original image containing cracks (top), detected potential crack pixels on 8 mm (middle left), 4 mm (middle right), 2 mm (bottom left), 1 mm (bottom right)

## 6. Camera data processing, results and discussion

The experiment suggests that, in LF approach, the proper LODs which should be considered for crack detection are from 1/8 as coarsest level to 1/2 as finest level. As the assumption is that the crack width is maximum 1 cm, the LOD coarser than 1/8 is not suggested. As described in (Miraliakbari, et al., 2016), selecting finest level of detail (1/1) might cause having too many noises in the potential crack image. These noises are due to the dark pixels which are located at the boundary of bitumen and asphalt aggregates. However, selection of LOD 1/1 is not problematic while the small artefacts are removable during post-processing step.

### Investigation on the template size

The size of the template plays an important role in crack detection process. Inappropriate selection of template size (either too small or large size) might result commission and omission errors in the process of pavement crack detection. Experimental investigations in this research proves that the proper size of selected quadratic template (in pixel) amount to  $21 \times 21$ px. Figure 69 represents the comparison of crack detection using LF in different LODs (from left to right 1/8, 1/4 and 1/2) and dissimilar template size (from top to bottom 11, 21, 51 and 71).

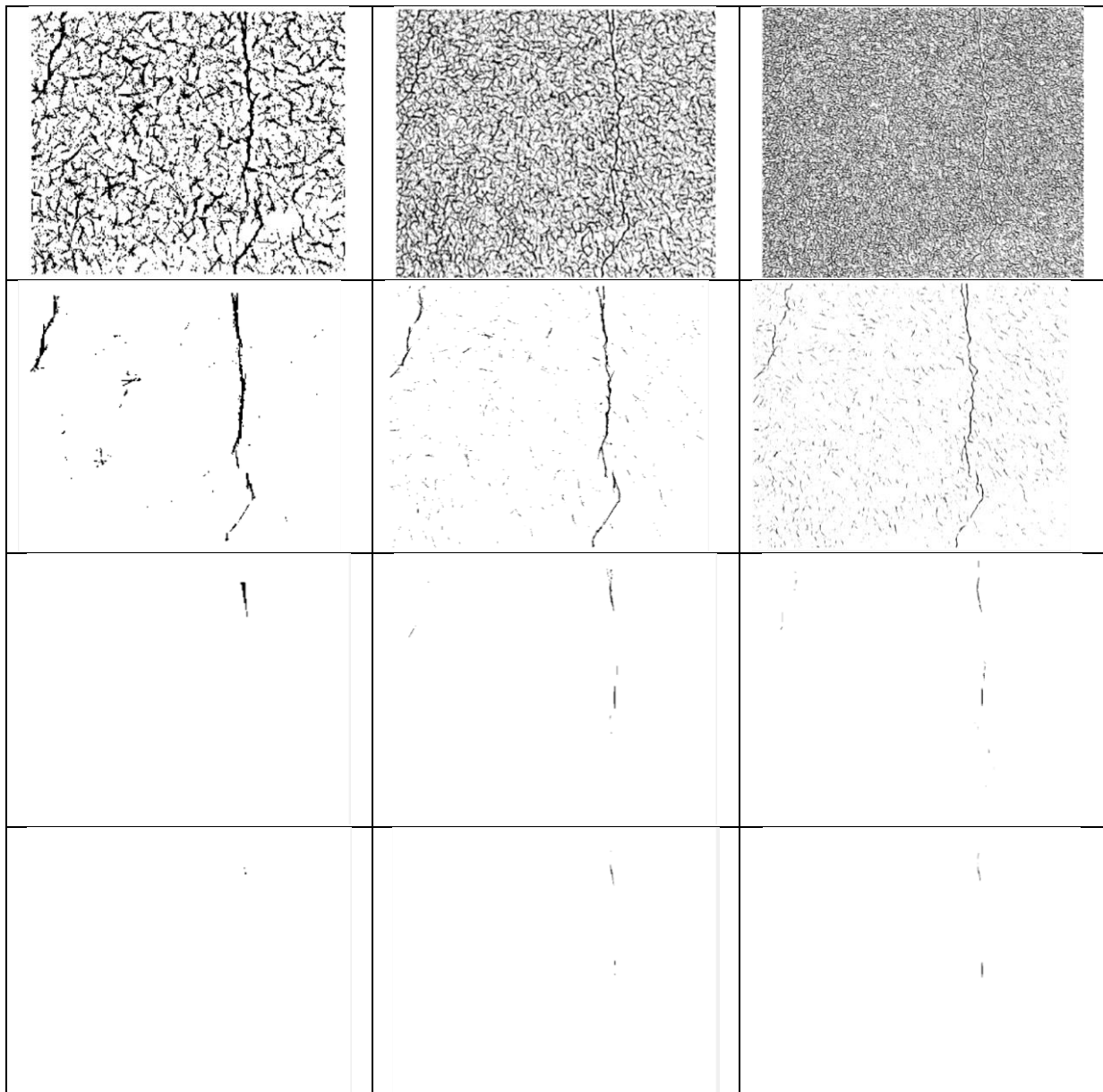


Figure 69. Comparison of crack detection using LF in different LODs (from left to right 1/8, 1/4 and 1/2) and dissimilar template size (from top to bottom 11, 21, 51 and 71)

The original RGB image is shown in Figure 68. The first row illustrates the potential cracks generated from small masks ( $11 \times 11$  px). In this row, the crack images are quite noisy in every LOD. The reason of presence of so many artefacts is the small size of the template. Second row shows the crack images generated from the appropriate masks which have the size of  $21 \times 21$  px. In this row, on the one hand the artefacts of the crack images are relatively low and on the other hand the crack segments are detected properly. Third and fourth rows represent the crack images generated by masks of  $51 \times 51$  px and  $71 \times 71$  px. Most of the crack pixels are vanished using these templates and the remaining crack pixels are somehow hardly visible. The disappearance of the crack pixels has some reasons. Using a large mask size, the average value of pixels located in the neighbourhood of crack segment (within  $51 \times 51$  and  $71 \times 71$  bounding box) is at the same range of the average value of the crack pixels within the mask so that the convolution cannot detect the crack pixel. Second reason is that the crack segment may not remain straight-line within the length of the bigger template especially for coarse LODs. It results in smaller correlation than the predefined threshold ( $corr_{min}$  in section 4.5.2).

### 6.1.2. Crack detection using HPF

Using the advantage of image sharpening, the crack regions can be distinguished better from the neighbouring regions. Contrary to the previous section, in this method only one kernel which itself is rotation invariant has been taken into account (Miraliakbari, et al., 2016). By convolving the kernel, primary result will be an image which contains negative and positive values (Figure 70 right). In the sample shown in Figure 70, LOD 1/8 has been selected for representation. The minimum value of the result is -544 and the maximum value amounts to 1305. The negative values of the convolution result are important. Larger negative values represent the boundaries of the regions with sudden grey value changes. These regions are represented as dark regions such as crack segments and some isolated points. Therefore, using an empirical threshold, the positive and low negative values which are mostly representing the intact pavement surface will be eliminated.

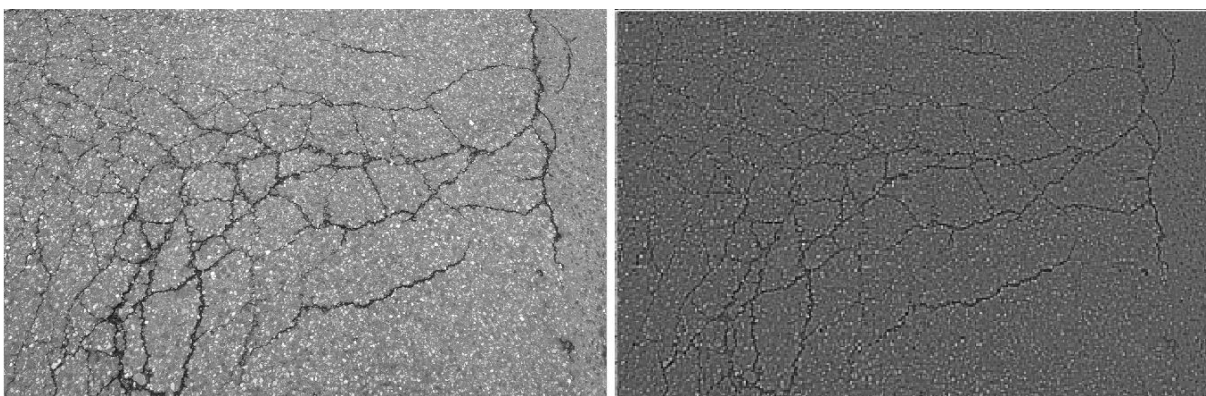


Figure 70. Original image (left), boosted image after convolving the filter containing negative and positive values (right)



## 6. Camera data processing, results and discussion

HPF is sensitive to the isolated features such as dark oily spots or aggregates which have different contrast compared to their neighbourhood. Hence, the result of crack detection using HPF looks noisy (Figure 71) although, input image is smoothed using bilateral filter. On the other hand, there exist a lot of discontinuities along the crack segment which is another consequence of using this kernel. To avoid these discontinuities, morphological dilation is performed to connect the component of crack segment. Figure 71 shows the result of crack detection using HPF after applying the threshold. The union of the detection result on LODs 1/2, 1/4 and 1/8 before dilation (left) and after dilation (right) are shown in this figure. In the right subfigure, the crack segments are presented thicker and mostly connected with each other.

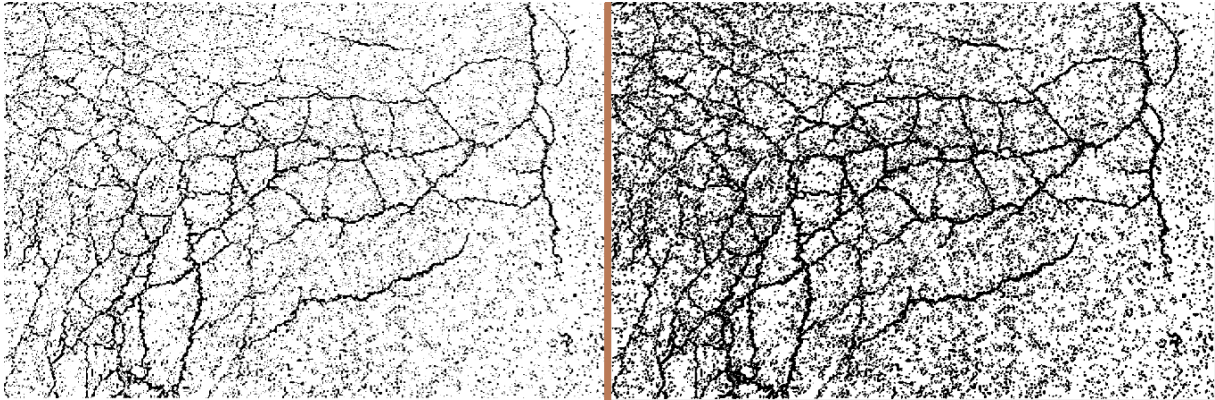


Figure 71. Union of crack detection result using HPF on LODs 1/2 1/4 and 1/8 before dilation (left) and after dilation (right)

Figure 72 illustrates a lower left clip of the crack image shown in Figure 71. In the left subfigure, details such as aggregates, crack segments and bitumen are fairly shown. The figure shows crack detection result using HPF fused over LOD 1/2, 1/4 and 1/8 before dilation (middle) and after dilation (right). As presented in the right subfigure, most of the gaps between the crack segments are filled after the dilation process. The selection of proper size for the structuring element is crucial and the size of structural element depends on the resolution of the image. Although, following the dilation process, the areas of noises are increased the noises will be eliminated by means of post-processing (section 6.1.4).

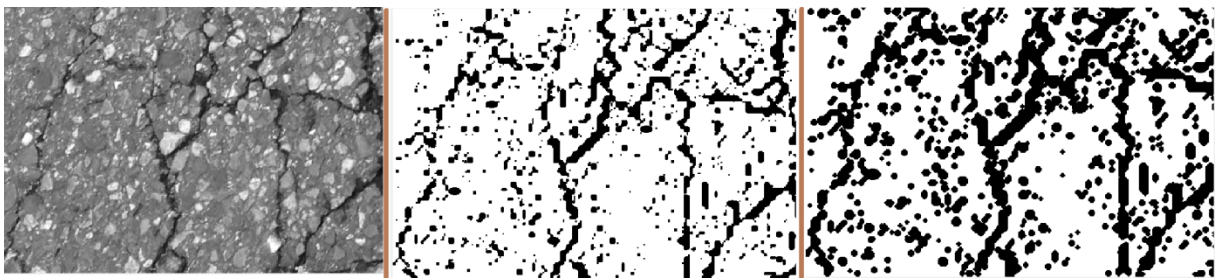


Figure 72. An image portion (left), crack detection result using HPF fused over LOD 1/2, 1/4 and 1/8 before dilation (middle) and after dilation (right)

The experimental investigation proves that crack detection using HPF is the fastest one while only one kernel is utilized for the crack detection process (Miraliakbari, et al., 2016).

### 6.1.3. Crack detection using MLBP

As discussed in section 4.5.4 only three templates out of nine unified invariant binary configurations are utilized in MLBP due to their edge detection manner. Figure 73 represents the original image (left) and corresponding result of LBP including all unified patterns (from 0 to 8) on LOD 1/4.

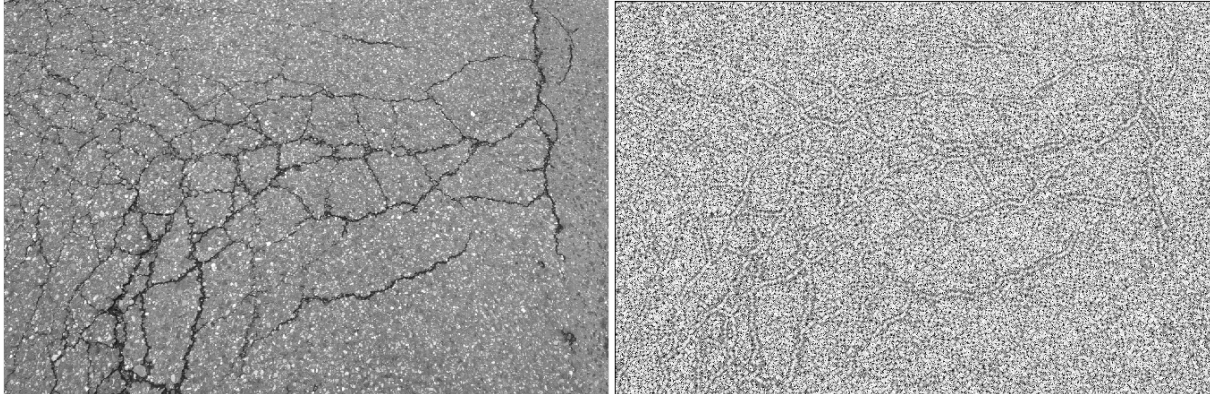


Figure 73. Original image (left) and result of LBP containing all unified patterns (from 0 to 8) on LOD 1/4 (right)

As represented in the right subfigure, the result is quite noisy. The reason is that all unified pattern (see Figure 28) are taken into account and most of them are irrelevant for crack detection process. The union (fusion) of the result of LBP using patterns 3, 4 and 5 is shown in Figure 74 (left). Although the result is still noisy, one can recognize the crack by black line segments representing the border of the crack in the left subfigure. In order to filter the binary result of LBP, the local variance of pavement image pixel is calculated. It is obvious that the pixels which are located at the boundary of crack segments have higher variances compared to the intact pavement pixels. Therefore, the outcome is thresholded to ignore low variances. The result of thresholded local variance of the image is illustrated in Figure 74 (right).

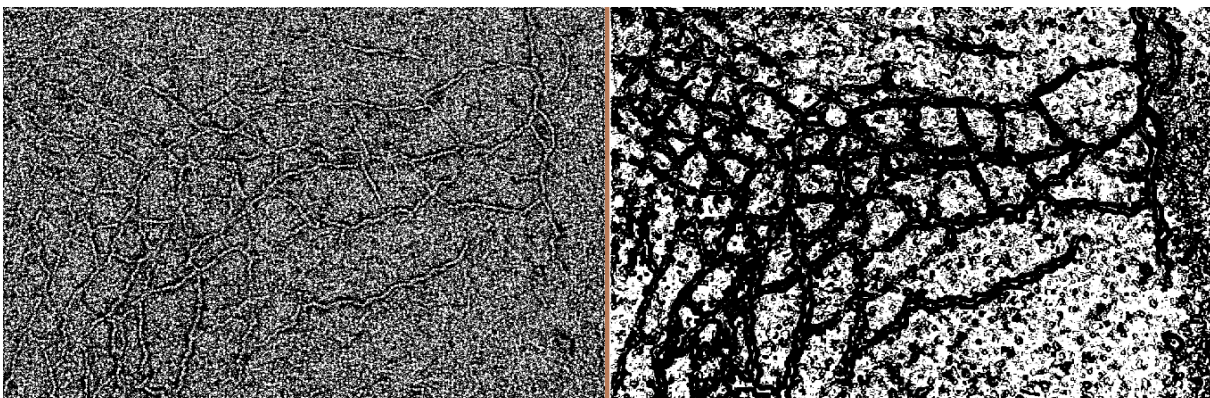


Figure 74. Result of union of binary pattern 3, 4, and 5 in all LODs (left), result of thresholded local variance of the image (background is represented in white colour)

Intersection of union of the three binary patterns and the thresholded local variance of the image (MLBP) produces the potential crack segments which mostly cover the boundary of the cracks (Figure 75). In Figure 75, the illustrated results are raw outcomes and still contain noise.



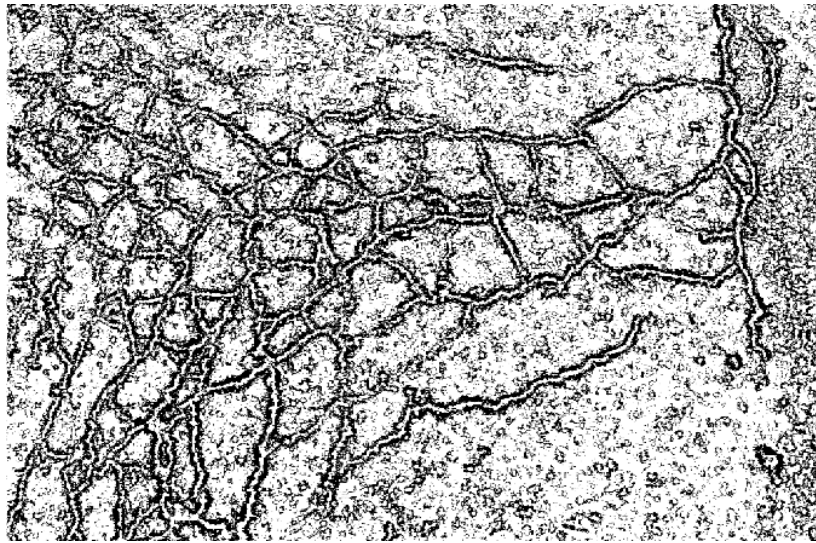


Figure 75. Intersection result of union of binary pattern and the thresholded local variance of the image (background is represented in white colour)

As shown in these figures there are some isolated points which are falsely represented as crack segments which are as a matter of fact the dark borders between the bitumen and the aggregates. Also in MLBP results, there will be always some artefacts appearing in the outcome that are mostly connected to the real crack segments. In order to remove the artefacts from the real crack segments first the morphological operation as erosion is carried out. By applying erosion, it is tried to disjoint the artefacts from the real crack pixels. Moreover, the isolated artefacts can be eliminated by erosion. Afterwards closing is considered to connect the crack pixels to each other by filling the inner part of the cracks together with thickening crack area (Miraliakbari, et al., 2016) (see Figure 76). The sequential order of erosion and closing is applied only in this approach.

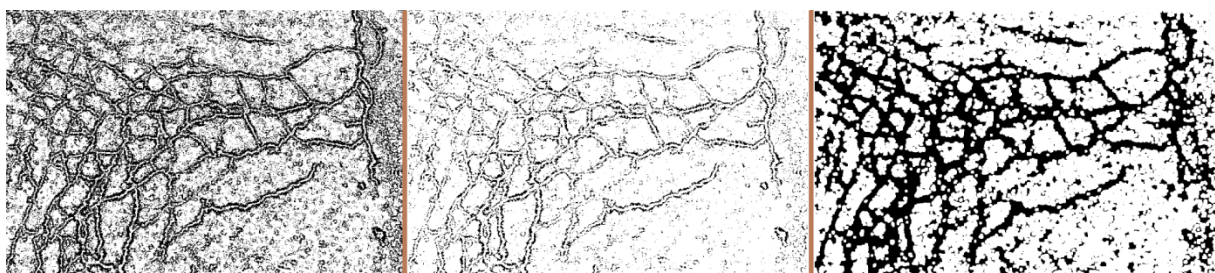


Figure 76. Intersection result of union of binary pattern and the thresholded local variance of the image (left), eroded result (middle), applying closing operation (right)

#### 6.1.4. Post-processing of crack detection results

Injured and imperfect pavement surface, wet surface and dirt (e.g. oily spots) on the road can bother the crack detection process. Moreover, the boundary of the road marks, gullies, manhole heads and leaves can be falsely detected as crack. Such unwanted effects degrade the crack detection results and



increase the need of post-processing. Two samples are shown in Figure 77 and Figure 79 together with all post-processing steps.

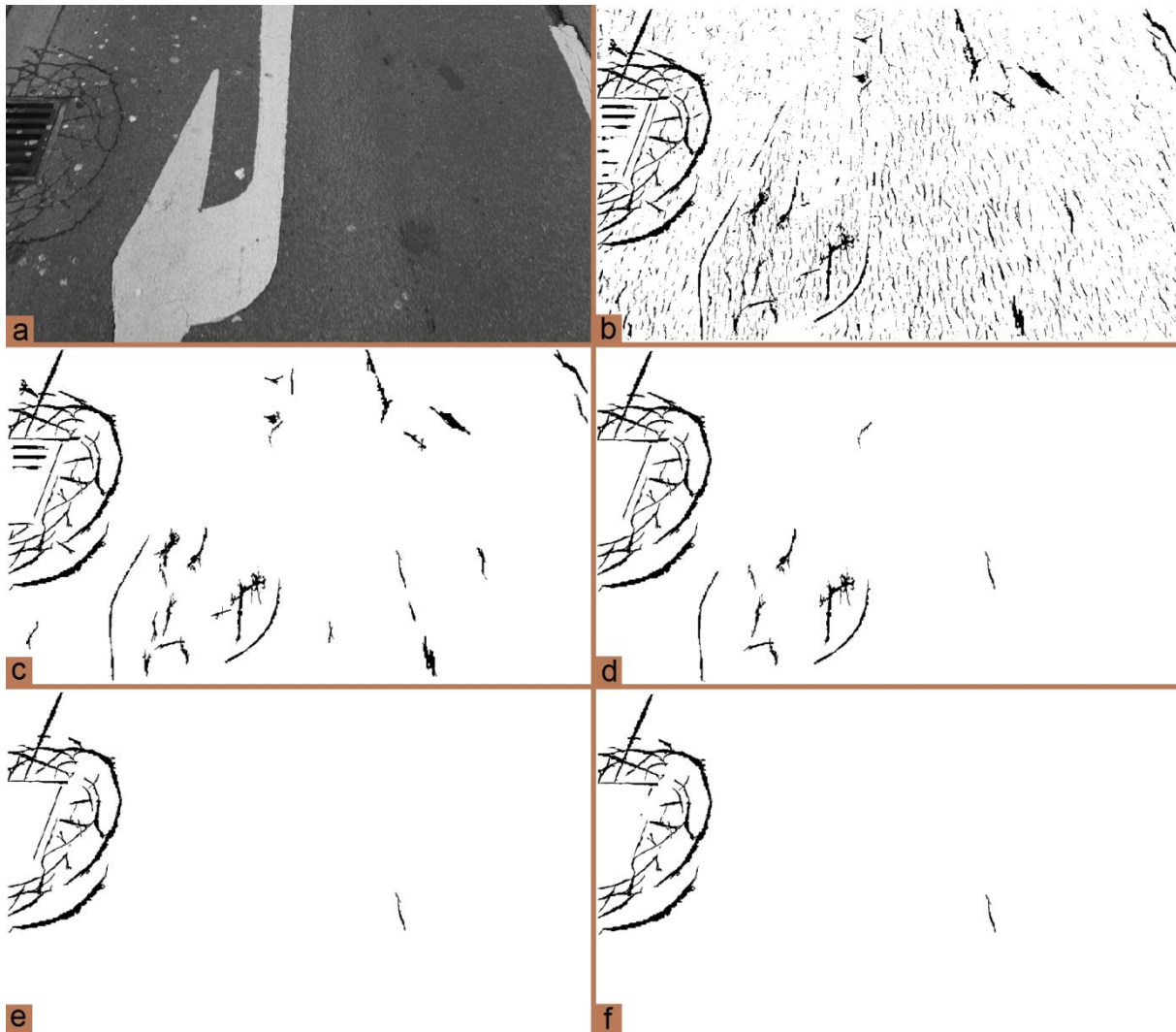


Figure 77. Original image, (a), potential binary result of crack detection results using LF including all artefacts (b), binary result of crack detection filtered based on the area (c), further filtered result using roundness criterion (d), removing all detected regions located inside or at the border of the road mark (e), filtering all detected regions sharing border with the gully (f)

As presented in Figure 77 (a) whereas all crack segments are detected in the preliminary outcome, the result is full of artefacts which are mainly the boundaries between the bitumen and aggregates. By thresholding, the segments of the binary results which have small area are eliminated. Subfigure (c) looks cleaner but still there are plenty of artefacts. Segments which have greater roundness compared to the crack regions are afterwards filtered (subfigure (d)). Inside the gully region, luckily, due to the roundness of the detected segments, all three segments have been removed during the second filtering based on the roundness (see Figure 78). In the next step all detected regions located inside or at the border of the road mark are filtered (e) and finally misclassified regions which share border with the gully are removed (f). A closer view of the detected cracks in the vicinity of the gully is depicted in Figure 78.

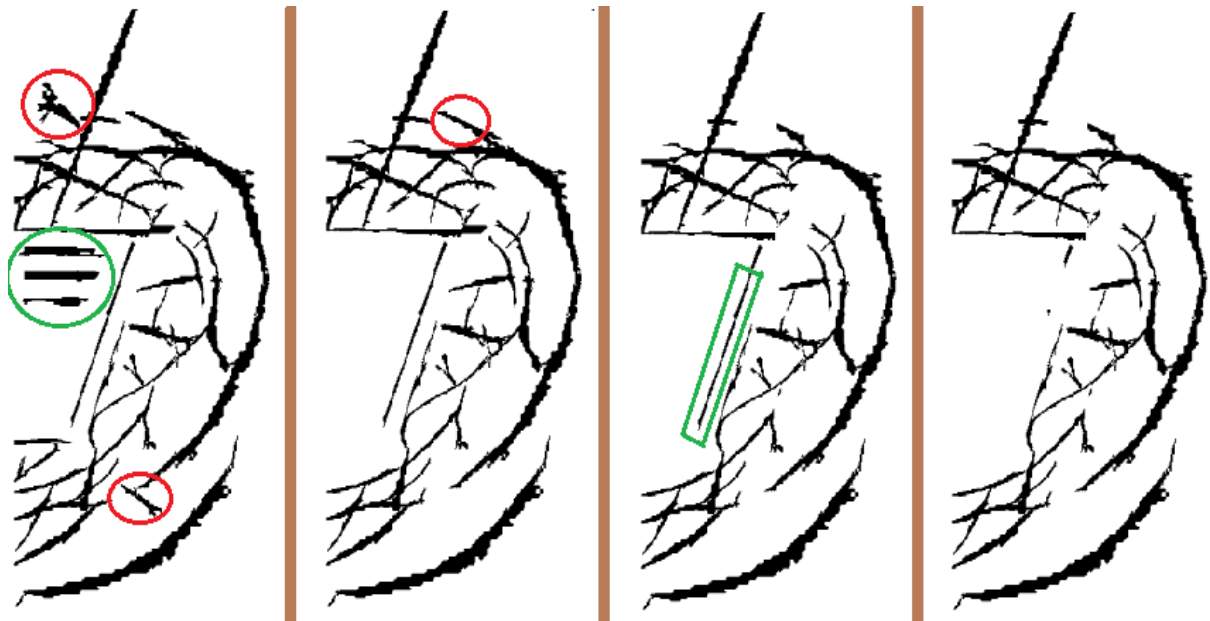


Figure 78. Detected cracks after filtering based on criterion ‘area’ (left), detected cracks after filtering based on criterion ‘roundness’ (second), outcome after filtering road mark borders (third) and gully borders (right), falsely eliminated crack segments are marked in red, correct removal is represented inside the green region

As shown in Figure 78, inside the gully there are three segments which are falsely detected as cracks (marked with green circle). Due to their thickness, they are vanished through the further filtering by means of the roundness. Also the right part of the frame of gully (marked with green rectangle) is eliminated during the last post-processing step (manhole-gully removal). The local STD of the pavement image is considered for gully removal, because the gully region is more homogenous compared to the pavement region. Nevertheless, some crack pixels (inside the red circles) are eliminated during the post-processing steps.

Figure 79 illustrates another sample of crack detection by means of Lf method together with the post-processing steps. The pavement image includes intact pavement asphalt, crack regions, one leaf and a part of road mark (a). Subfigure (b) shows the initial including artefacts which are mainly the boundary between the aggregates and bitumen, border of road mark and some other non-crack regions which are due to the existence of moistures on the pavement surface. Subfigures (c and d) are the results of filtering based on the area and roundness, respectively. In this sample the roundness threshold is set to 0.12. The falsely detected regions which are inside or at the boundary between the road mark and asphalt are filtered (d) by means of histogram analysis (Miraliakbari, et al., 2016).

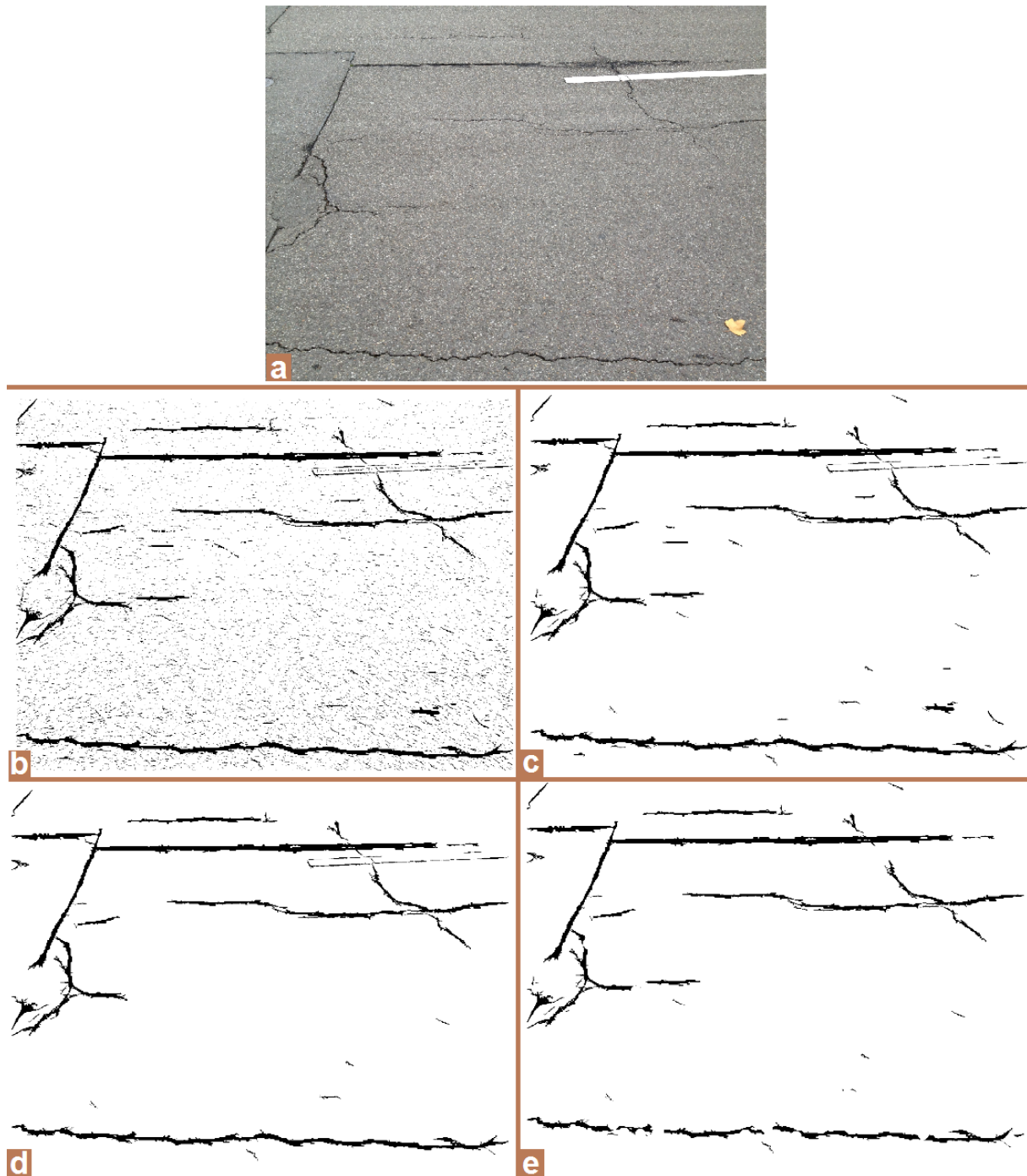


Figure 79. Original image, (a), potential binary result of crack detection results using LF including all artefacts (b), binary result of crack detection filtered based on the area (c), further filtering using roundness criterion (d), removing all detected regions located inside or at the border of the road mark (e), adapted from (Miraliakbari, et al., 2016)

### 6.1.5. Comparison of crack detection using LF, HPF and MLBP

With respect to the processing speed, HFT is the quickest method for automatic crack detection compared to LF and MLBP. The main reason of such fast computational speed is that HPF uses only one template the template itself is rotation invariant. LF variant utilizes 18 kernels, so that is more time taking. In MLBP method, three different kernels (binary patterns 3, 4 and 5) have been used together with the thresholded local STD which make the process computationally more expensive.

## 6. Camera data processing, results and discussion

Remarkably it is observed that in LF, the edges which are mostly the boundary between the shadow and sun on the pavement surface are never detected. In contrast to LF, MLBP works as edge detector because of the shape of selected binary patterns (binary patterns 3, 4 and 5). Because of its high sensitivity, edges located mostly on the border of bright aggregates in the neighbourhood of crack area will be connected to the crack segments. Hence, the morphological operation is utilized in order to disjoint those edges from the crack pixels by means of erosion and fill the gaps between the crack edges using closing criterion. Figure 80 illustrates the final result of crack detection (after post-processing) by means of Lf, HPF and MLBP variants (Miraliakbari, et al., 2016).

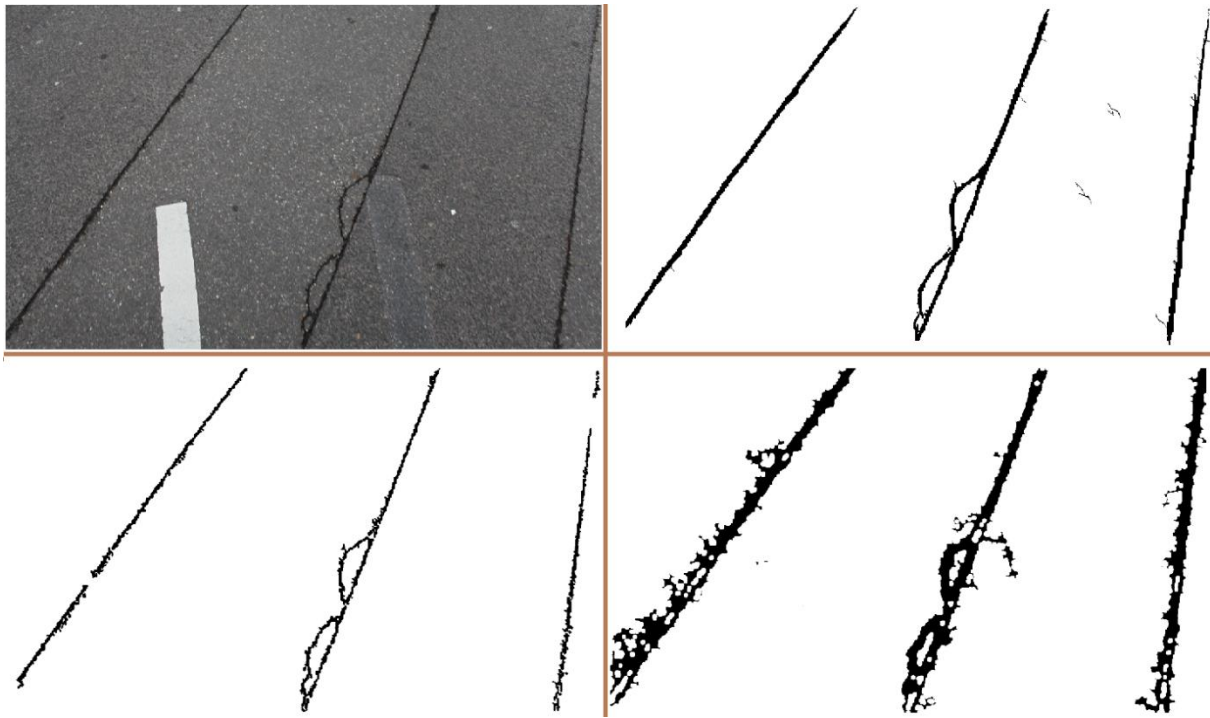


Figure 80. Crack detection results after the post-processing steps; original pavement image (top left), final result of pavement crack detection by means of LF (top right), HPF (bottom left) and MLBP (bottom right) (Miraliakbari, et al., 2016)

For the accuracy assessment of the crack detection process the focus is on completeness (Miraliakbari, et al., 2016), because, here the omission errors are more critical than commission ones. The main reason is that first: due to the down-sampling of the original image in the coarser LODs, cracks which their width is smaller than a pixel in the current coarse LOD will mostly appear due to the interpolation process of down-sampling. If such cracks are detected in that LOD, after resampling of the crack detection result, they will be represented thicker than their actual size in the finer LODs. Therefore, the probability of having thicker results than the original crack width is high and it will increase the commission error during the accuracy assessment. Secondly, in the evaluation standards of road condition mapping, the area of cracking region is important. In such case, additionally if there are by chance some minor non-crack regions detected by the proposed methods, they will not harm the evaluation results. Nevertheless, it is tried to ignore non-crack regions as much as possible.

The completeness of crack detection results are calculated for all 20 samples of pavement images. For all samples, in the post processing step, the 'optimal' values of roundness which are used for LF, HPF and MLBP amount to 0.2, 0.5 and 0.2, respectively. Table 10 lists the percentage of the completeness of for these samples with respect to the crack detection variants. Furthermore, the average of completeness value of each detection variant is listed. The comparison shows that due to the overall

sensitivity of LF to linear structures, all experiments have completeness over 60 %. The completeness of three samples is below 50 % in HPF variant and for MLBP method, only one sample's completeness is less than 40 % which is the worst case compared to the rest of the results. Whereas the mean values of LF and MLBP completeness are nearly the same, the completeness outcome of MLBP could be much lower if there was not further closing in the process. By closing procedure in MLBP, it has been tried to connect the crack edges and fill the crack results. The percentages of detection completeness are illustrated in Figure 81 (Miraliakbari, et al., 2016).

Image Nr.	LF %	HPF %	MLBP %
1	91.25	82.79	94.38
2	81.96	65.59	84.43
3	64.39	51.78	90.56
4	70.46	49.02	58.71
5	67.18	43.60	39.86
6	94.46	69.57	86.35
7	92.00	74.38	94.02
8	73.19	62.74	66.62
9	83.76	91.39	91.52
10	62.40	91.67	91.88
11	70.97	92.47	90.62
12	87.97	92.29	94.90
13	86.82	91.70	82.19
14	84.53	94.82	91.83
15	88.36	86.53	90.18
16	91.13	96.96	96.51
17	71.09	44.02	78.40
18	90.49	87.21	72.39
19	91.39	85.44	74.42
20	79.71	70.75	51.69
Average of completeness	81.2	76.2	81.1

Table 10. Completeness of crack detection with respect to the image samples and the crack detection method (LF, HPF and MLBP) adapted from (Miraliakbari, et al., 2016)

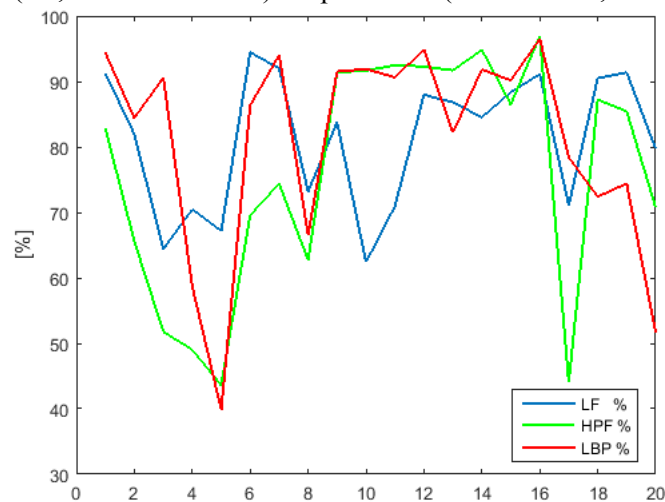


Figure 81. Completeness result of crack detection with respect to LF, HPF and MLBP (Miraliakbari, et al., 2016)



## 6. Camera data processing, results and discussion

The graphs represented in the figure admit that mostly a low completeness in one variant is compensated in another variant. Whereas samples 4, 5 and 17 have completeness less than 50 % using HPF variant, their completeness in LF raises and is over 60 %. Hence, fusion of crack detection results can increase the completeness results (Miraliakbari, et al., 2016).

### 6.1.6. Fusion of the crack detection results

In order to increase the value of completeness in crack detection results and reduce remaining artefacts of each detection approach, feature fusion approach is considered. Figure 82 illustrates a sample of pavement image and post-processed results of crack detection. For this image, the percentages of completeness of crack detection using LF, HPF and MLBP amount to 90.49 %, 87.21 % and 72.39 %, respectively.

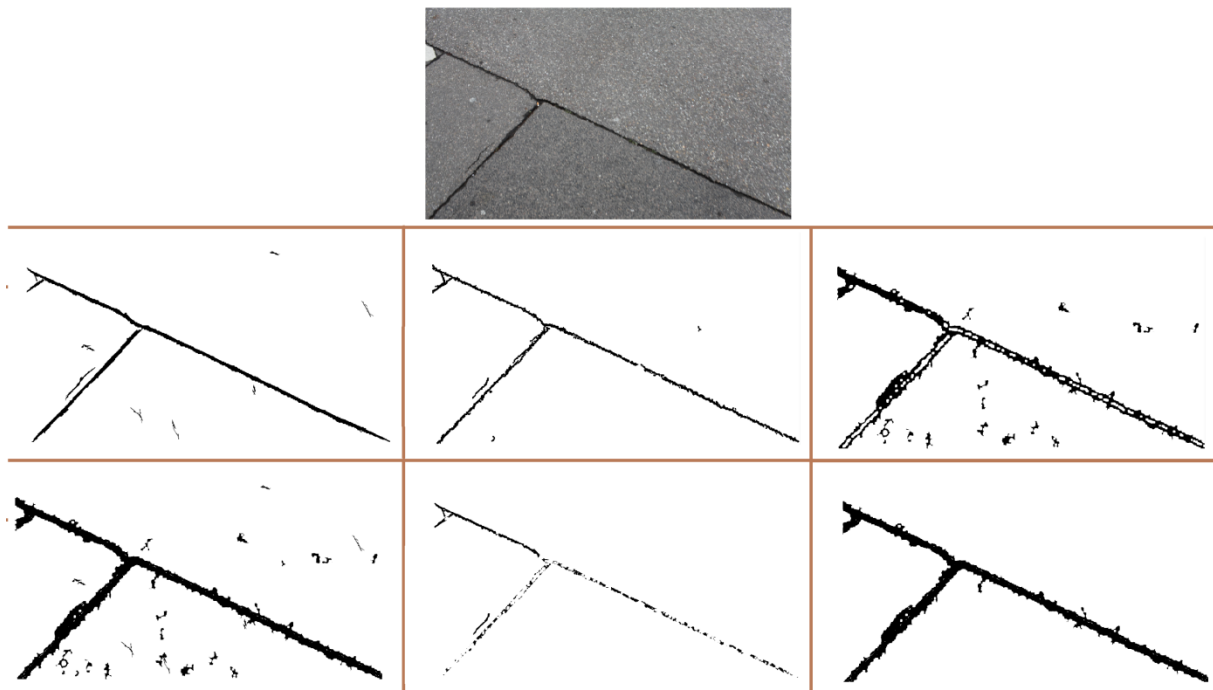


Figure 82. Original image (top), post-processed result of crack detection using LF (middle left), HPF (middle middle) and MLBP (middle right), union of all results (bottom left), intersection of all results (bottom middle) and result of binary reconstruction (bottom right)

As presented in Figure 82, all post-processed results contain some non-crack regions which are falsely detection as crack segment. On the other hand each result has lack completeness (especially using MLBP method) which can be compensated by the fusion. In this sample, the completeness of the fusion result amounts to 99.5 %. Another advantage of using fusion is that by fusing LF, HPF and MLBP, the artefacts (the non-crack segments) will mostly disappear (Figure 82). The disadvantage is that because of fusing MLBP results, the artefacts (aggregate boundary which are in the vicinity of the cracks) connect to the crack in some area. On the other hand the cracks appear thicker than their actual width (subfigure bottom right). Alternative is to make use of only LF and HPF in the fusion process. In this regard, the result of fusion using LF and HPF (Figure 83) looks much similar to the ground truth than the result of previous fusion. The completeness of 98.6 % for this fusion is still significantly high. The mean of overall completeness for all 20 samples using fusion results of LF and HPF amounts to 86.7 %.

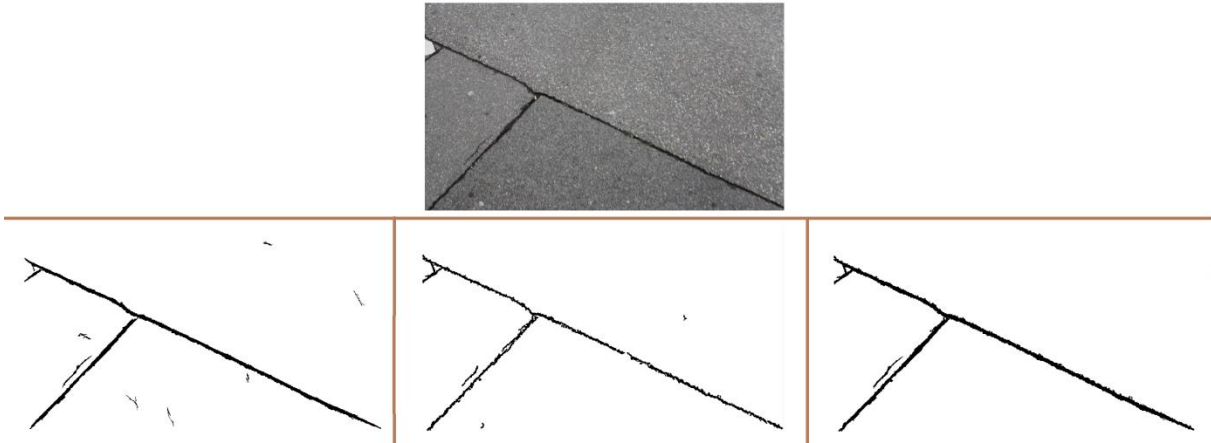


Figure 83. Original image (Top), Post-processed result of crack detection using LF (bottom left), HPF (bottom middle) and result of binary reconstruction (bottom right)

## 6.2. Patch detection

For the automatic patch detection, geodesic morphological reconstruction and texture measures which are image gradient magnitude and local STD are utilized.

### 6.2.1. Patch detection using geodesic morphological reconstruction

The geodesic morphological reconstruction is sensitive to grey value variations within the patch, in particular if the grey scale difference  $g_{off}$  (section 4.4.1) between the marker and mask is small. An example of such failure is depicted in Figure 84. Two connected patches which are darker area than the intact asphalt surface are shown in this figure. A large area of the right patch is brighter than the rest of this patch which leads unsuccessful detection of the patch region.

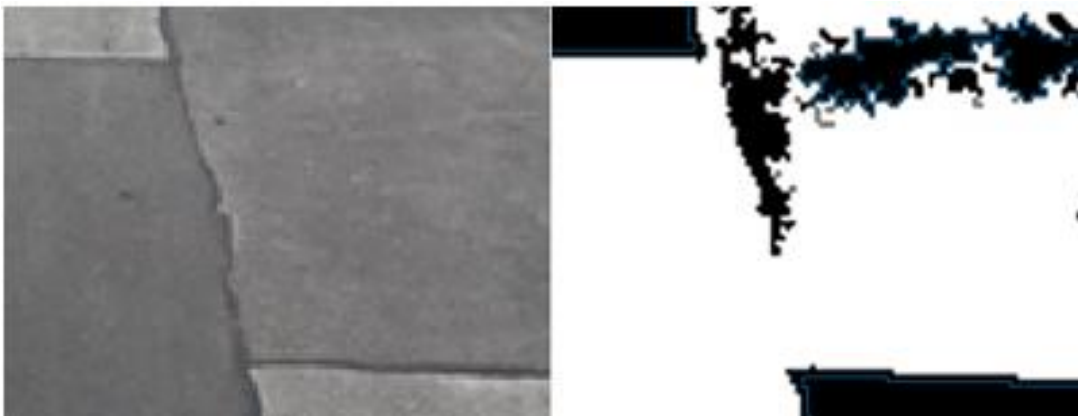


Figure 84. An image window including two connected patches (left) and the segmentation result containing the patch and non-patch regions within the second patch (right)

### 6.2.2. Patch detection using texture measures (gradient magnitude and local STD)

Patches on the pavement images have different characteristics. Some are connected to the image border due to the lack of image coverage, some are small and in the middle of the image, some others are old and the colour differentiation between the intact asphalt surface and the patch is difficult. Some pavement images contain more than one patch and sometimes (depending on the age of the pavement) the scene contains several small patches with different ages and textures. This condition makes the procedure of patch detection more crucial. To cope with these patch detection difficulties, two texture measures which are gradient magnitude and local STD are considered. The simplest condition is to have only one patch in the scene or if more, the patches should have the same age (same intensity in the image). Figure 85 shows the patch detection using image gradient magnitude.



Figure 85. Patch detection using image gradient variation

The detailed analysis of the patch detection is represented in Figure 86.

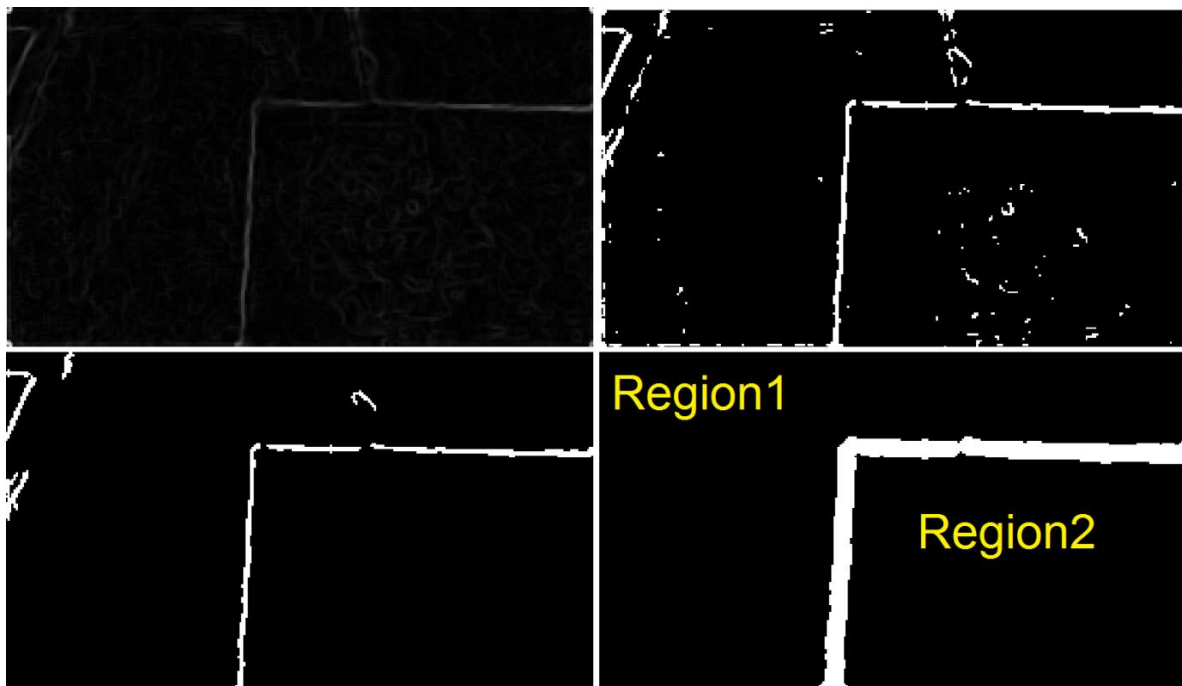


Figure 86. Image gradient (top left), thresholded image gradient (top right), filtering small objects (bottom left), filtering round objects and dilating the remaining segments (bottom right)



In the first subfigure, (top left), the result of the image gradient (which has unsigned integer 8 bit value) is represented. The minimum of the gradient value is 0 and the maximum amounts to 255. Due to the importance of the gradient with higher magnitude (extreme gradient changes) and also small amount of such magnitude, the left part of the histogram of the image gradient is filtered out (see Figure 31 in section 4.6.2). Due to the existing of several noises on the binary result, the small and round objects are filtered out. The dilated filtered binary result which separates the asphalt and patch region (Region 1 and Region 2) is depicted in the subfigure (bottom right). The mean grey values of Region 1 and Region 2 are 123 and 92, respectively. Therefore, Region2 is selected as the patch area.

As explained in 4.6, patches in the pavement image are not always as easy as presented in Figure 85. Figure 87 illustrates the result of multi patch detection using STD of the image.

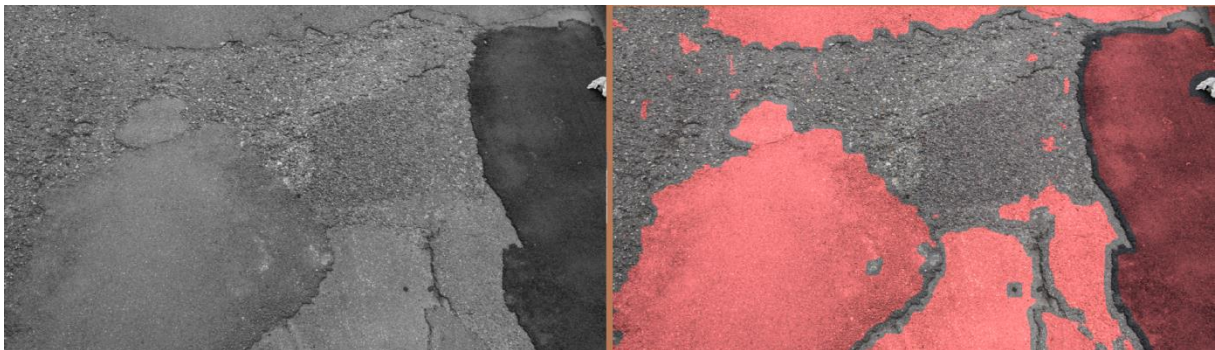


Figure 87. Grey value image (left), result of multi patch detection using STD of the image.

As presented in Figure 36 in section 4.6.2, 7 regions different with different patches are in this pavement image. As shown in the figure, the detection is based on the homogeneity of the regions and somehow independent from the intensity value. This attribute helps to detect the patches which are older than the other patches.

## 7. Spectrometry data processing, results and discussion

The following sections describe spectral feature analysis, pavement class definition, separability analysis and pavement surface classification.

### 7.1. Spectral feature analysis

The spectral signatures produced by ASD spectrometer are considered for spectral feature analysis. Whereas the wavelength domain of these spectral signatures is from 350 nm to 2500 nm, a certain amount of reflectivity values must be filtered out. Such filtering is because of the water absorption bands in the spectral data and the boundary between the detectors of the spectrometer. The existence of water absorption spectra is due to the atmospheric path between the sensor head and the asphalt pavement surface. The filtering is applied on the following wavelength ranges: 1220 nm to 1490 nm, 1770 nm to 1970 nm and 2400 nm to 2500 nm. Figure 88 illustrates a spectral signature produced by ASD. The reflectivity values within the water absorption range and the boundary between the detectors shown in black colour are distorted. Therefore, these reflectivity values are employed neither for the spectral feature analysis nor for the classification purposes.

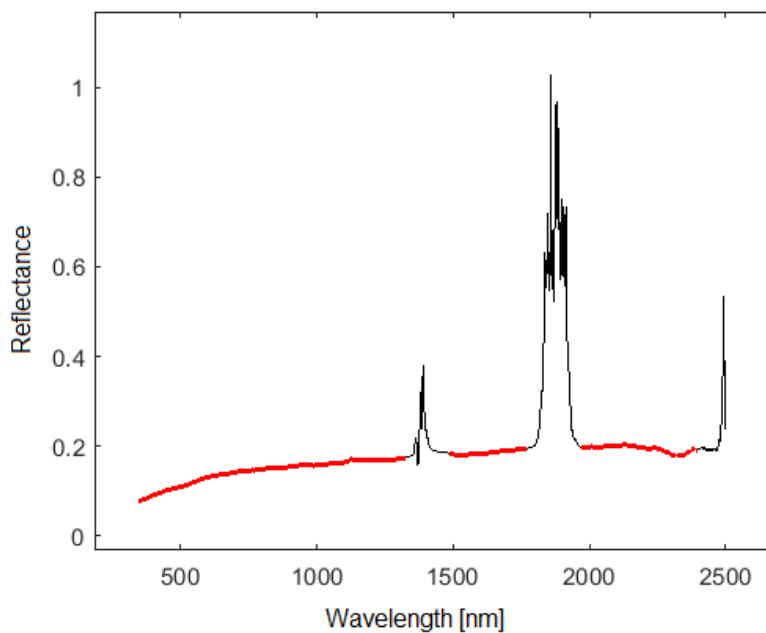


Figure 88. A spectral signature produced by ASD, the overall wavelength range of the spectral signature is from 350 nm to 2500 nm. The reflectivity values shown with red colour are considered for spectral feature analysis

As discussed in 4.7.1, in this study, line slope is utilized for spectral feature analysis. 10 training spectral signatures are used for spectral feature analysis and illustrated in Figure 89. Five training samples shown with red colour belong to class 'Bad' and the rest illustrated with blue colour refer to the class 'Good'. The first observation at the figure declares the dissimilarity of the overall reflectivity between two classes. It is due to the colour difference between fresh and old asphalt pavement surface so that the surface of newly paved (Good) road has darker colour than the old (Bad) pavement surface. While the newly paved asphalt road contains more bitumen than the aged one, it has lower overall

reflectivity values than the deteriorated pavement surface. It should be mentioned that the in Figure 89, the reflectance difference between the training sets ‘Bad’ and ‘Good’ are fairly visible. Although, the figure implies that it should be sufficient to use the mean as a criterion, in most of the training sets, there are several overlaps between the spectral signatures of different classes (see Figure 95) and using mean as a feature for separability analysis will not be appropriate.

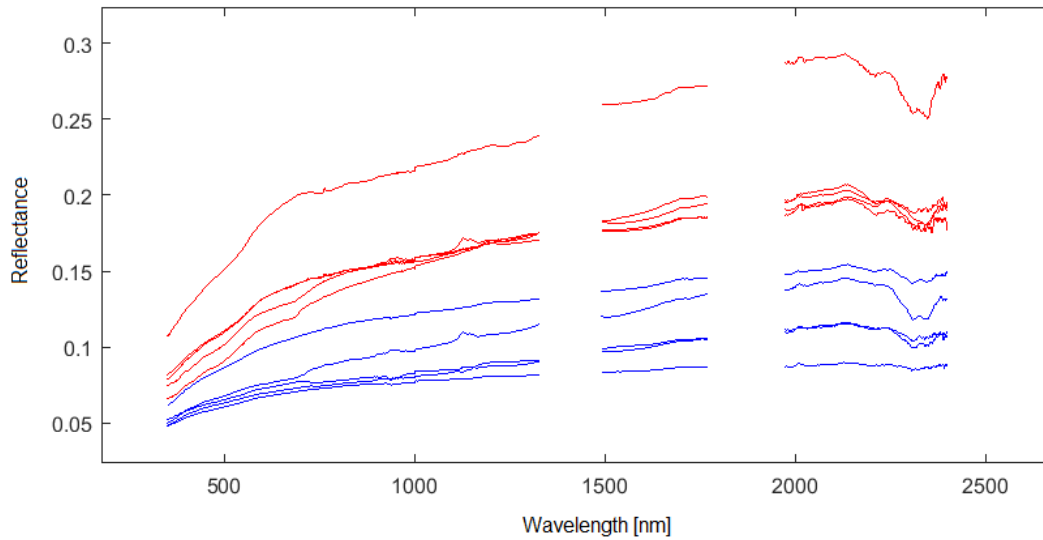


Figure 89. The filtered spectral signatures of 10 training samples captured by ASD spectrometer

Two wavelength ranges are selected to calculate the line slopes: 354 nm to 705 nm and 2145nm to 2199 nm. Figure 90 and Figure 91 show the spectral signatures of the training data within these wavelength ranges (left subfigures). For better representation of the slope difference between the ‘‘Good’’ and ‘‘Bad’’ training sets, each spectral signature is subtracted from its mean (right subfigures). In the right subfigure of Figure 90, whereas the overall slopes of the spectral signatures belonging to both training sets are positive, the slopes of class ‘‘Bad’’ bigger compared to the class ‘‘Good’’. Contrarily, in Figure 91, the slopes of class ‘‘Bad’’ are lower.

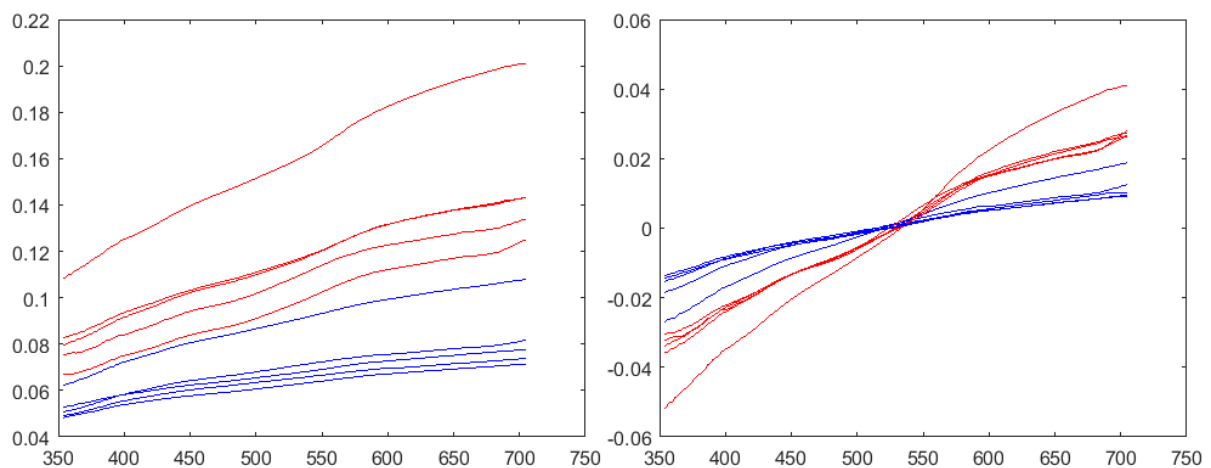


Figure 90. The spectral signatures of the training data corresponding to the wavelength domain of 354 nm to 705 nm (left), subtracted spectral signatures from their mean (right)

## 7. Spectrometry data processing, results and discussion

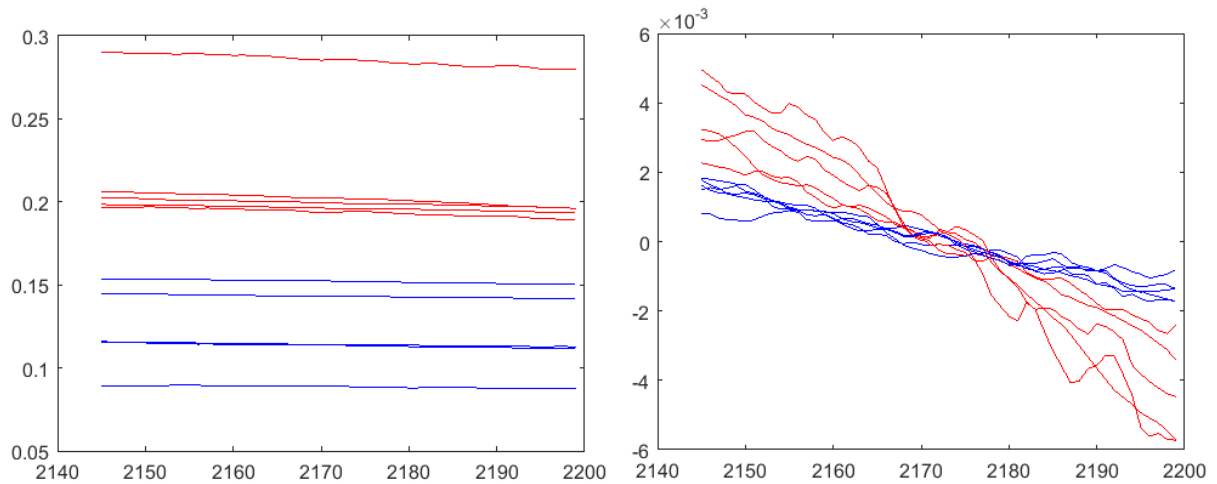


Figure 91. The spectral signatures of the training data corresponding to the wavelength domain of 2145nm to 2199 nm (left), subtracted spectral signatures from their mean (right)

Figure 92 illustrates the results of line fitting by regression for line slope calculation. As represented in the figure, the calculated slopes for these 10 training sets in both wavelength ranges separate distinctly “Bad” and “Good” classes. As expected, the slope values of the left and right subfigures are positive and negative, respectively.

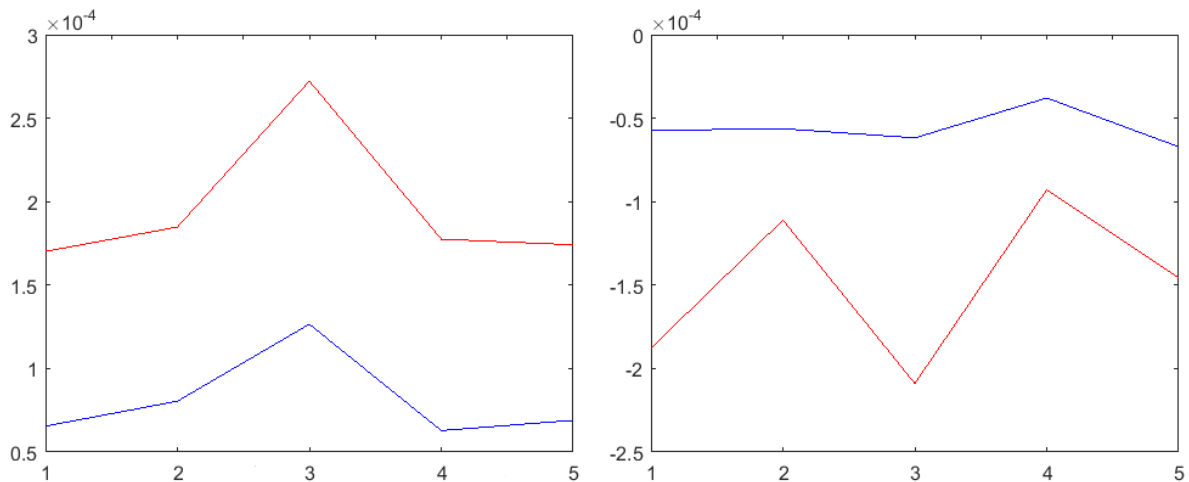


Figure 92. Line slope calculation corresponding to the wavelength domains of 354 nm to 705 nm (left) 2145nm to 2199 nm (right), X-axis is the sample number, Y-axis corresponds to the slope

### 7.2. LDA results for separability analysis

The aim of this section is to analyse the separability between different types of asphalts using spectral signatures. Two training datasets of “Good” and “Bad” are collected from several asphalt pavement sections with Polytec and Spectral Evolution spectrometers. The visual inspection is the first step of training data collection. Good (new) asphalts are normally darker and more homogeneous than bad (old) asphalts. On a homogeneous asphalt surface, the aggregates are hardly visible and the uppermost

level of asphalt surface is full of bitumen. Bad asphalts contain several cracks and have more aggregates on their uppermost level and less bitumen than the good asphalt. As in most cases, the deteriorated pavement surface contains cracks, the training data of class “Bad” are recorded from non-crack area of the deteriorated asphalt to avoid the risk of hydrocarbon feature representation. Figure 93 shows two samples (good and bad) of asphalt areas.

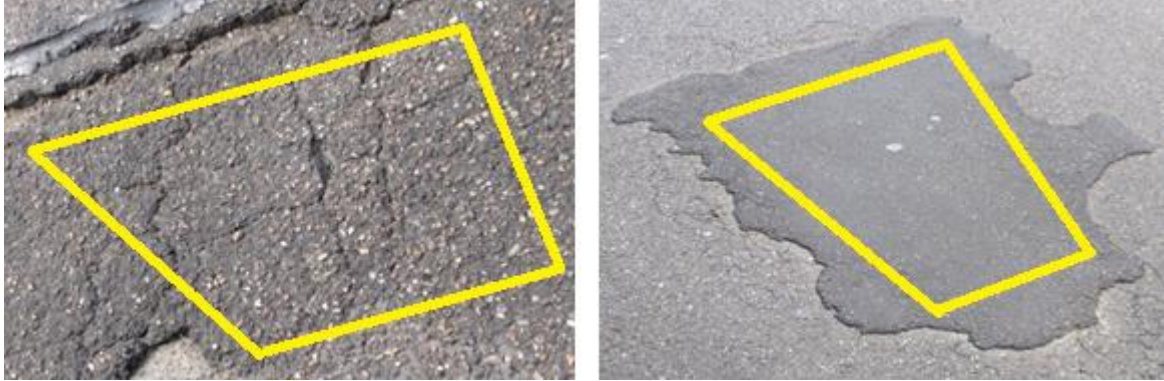


Figure 93. Two samples of training data; Bad (left) asphalt and Good (right) asphalt

The left subfigure represents a portion of a deteriorated asphalt section which contains several cracks with evident aggregates. The right subfigure shows a newly repaired asphalt area that has a homogeneous and dark surface with nearly no aggregate visible.

There have been several researches about urban material classification using hyperspectral remote sensing. In all these studies, there is mostly a specific dissimilarity between the selected training classes such as sand, gravel, cement, plastic, stone pavement, asphalt pavement, etc. (Le Brisa, et al., 2016). However, quality classification of any of those mentioned materials requires great effort. Bad (old) asphalts have been washed out and deteriorated during a long time period and the fraction of their bitumen that consists of the hydrocarbon material is much less than of good (new) asphalts. The colours of good (new) and bad (old) asphalt may not always be different and therefore, the changes in the amount of bitumen and aggregates on the asphalt surface can raise the chance of separability analysis.

### 7.2.1. LDA result of hand-held spectrometer

In Figure 94, training data collection of two samples of “Bad” (top left) and “Good” (bottom left) asphalt using “Spectral Evolution” spectrometer are shown. As spectrometry for each training sample takes few seconds, the spectrometry data contains several spectral signatures. Therefore, the average of reflectivity values is considered as one spectral signature for each individual training sample. Right subfigures represent the corresponding spectral signatures of these two training samples.

## 7. Spectrometry data processing, results and discussion

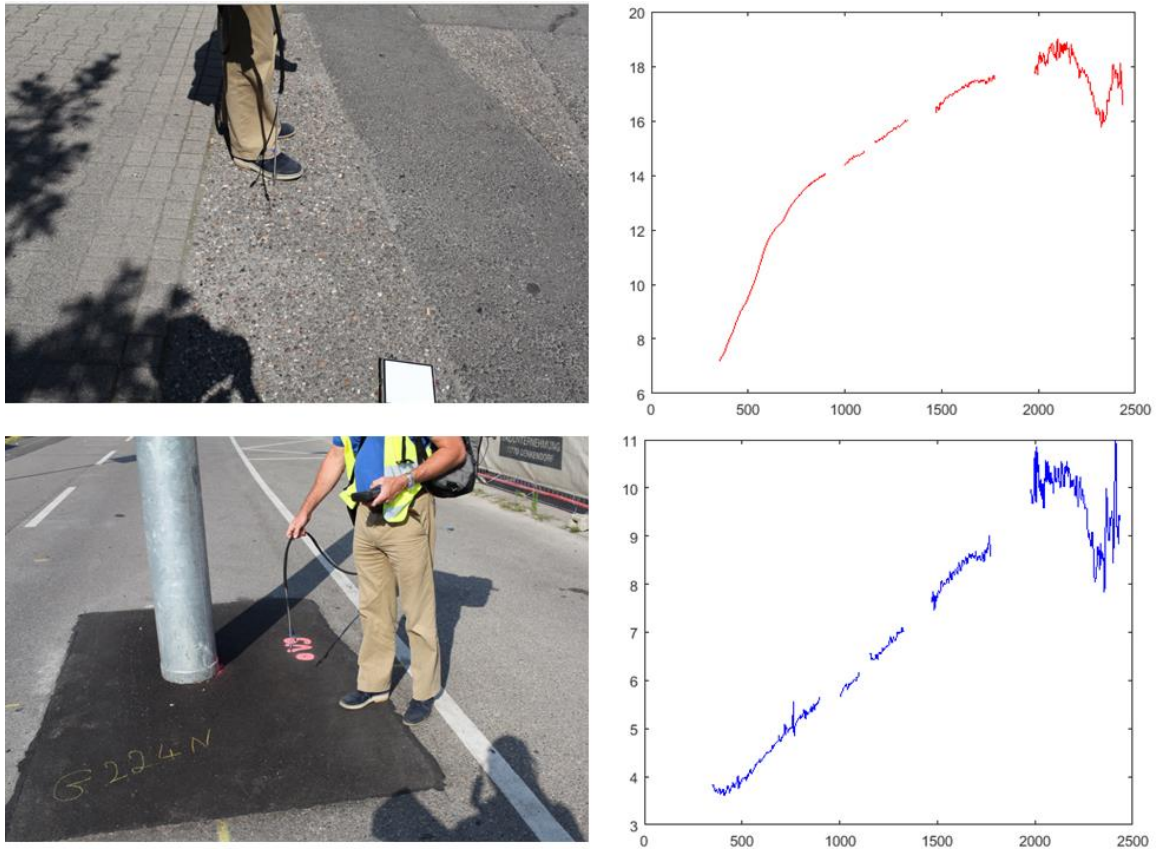


Figure 94. Spectrometry of two samples of training data; Bad (top left) and Good (bottom left), X-axis is the wavelength [nm], Y-axis corresponds to the percentage of reflectance

As shown in Figure 94, there are some gaps in the spectral signatures. These gaps placed in water absorption domains and boundary of the detectors of the PSR+3500 (Spectral Evolution) spectrometer are in the following wavelength ranges: 897 nm to 1000 nm, 1101 nm to 1155 nm, 1329 to 1469 nm, 1773 nm to 1979 nm and 2436 nm to 2500 nm.

### Separability analysis using LDA with training set and evaluation set

For separability analysis, in total, 34 “Bad” and 28 “Good” training samples are measured. Figure 95 represents mean spectral signatures of these training samples. Distorted reflectivity values at the water absorption bands and at the boundaries between the sensors of the spectrometer are filtered. As depicted in the figure, there is a large overlap between the spectral signatures of the classes. Existence of this overlap indicates that there is not a distinct difference between the absolute reflectance of ‘Bad’ and ‘Good’ classes.



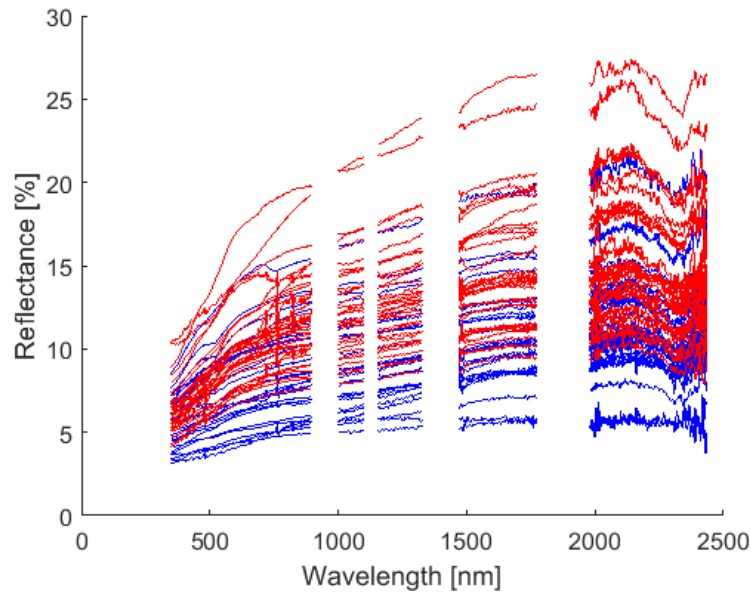


Figure 95. Spectral signatures of Good (blue) and Bad (red) asphalt regions, average of reflectivity values shown as one spectral signature

For the separability analysis, nearly 60 % percent of the training samples of each class is considered as training set and the rest as evaluation set. LDA tries to separate training sets “Good” and “Bad” as much as possible by looking for the features which can differentiate the classes. Figure 96 shows the feature vector  $\mathbf{w}$  generated by LDA. As shown in this figure, in visible and partially NIR wavelength range (351 nm to 896 nm), there is an obvious undulation. The greatest absolute value of the feature vector starts from 1980 nm and continues until 2400 nm. Projection of spectral signatures to the feature vector  $\mathbf{w}$  (Figure 97) separates training sets “Bad” and “Good”. As represented in Figure 97, the training sets have not overlap in the projection results.

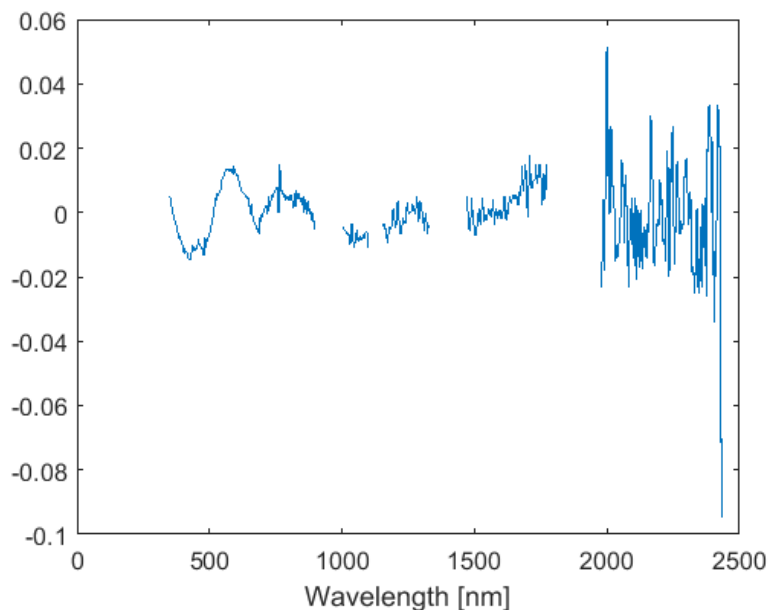


Figure 96. Feature vector  $\mathbf{w}$  generated by LDA, coefficients with high absolute values contribute most to the separation of classes

## 7. Spectrometry data processing, results and discussion

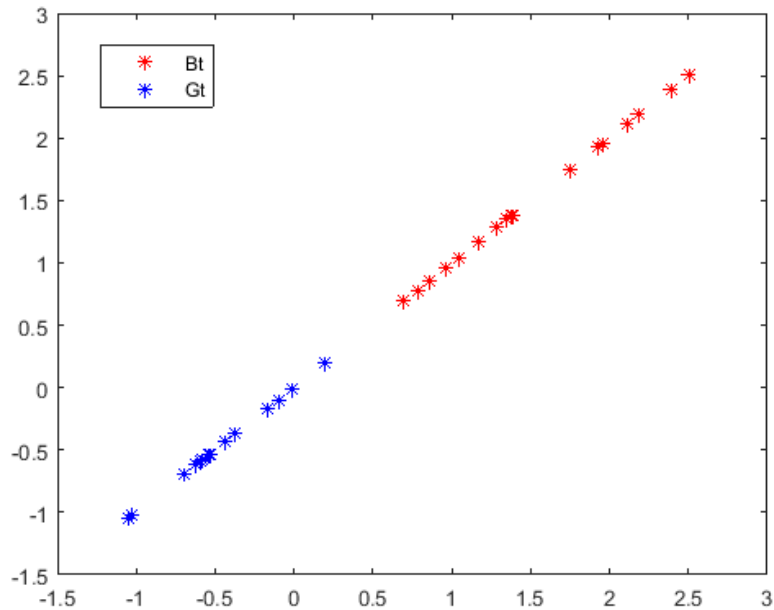


Figure 97. Projections of the training signatures to the feature vector  $\mathbf{w}$ , results are visualized in 2D for better representation; “Bt” and “Gt” stand for training set “Bad” and training set “Good”, respectively

Projections of training and evaluation sets are shown in Figure 98. Contrary to the projections of the training sets (blue and red points), the projections of evaluation sets (cyan and magenta points) show a less distinct separation between “Bad” and “Good” classes. Apart from false locations of two projections (shown in the black circles), the projections of two evaluation sets have an overlap (shown inside the black rectangle) which makes the separation more difficult. To identify a decision boundary, the middle of the space between two training sets (shown in Figure 97) is considered as the sharp threshold.

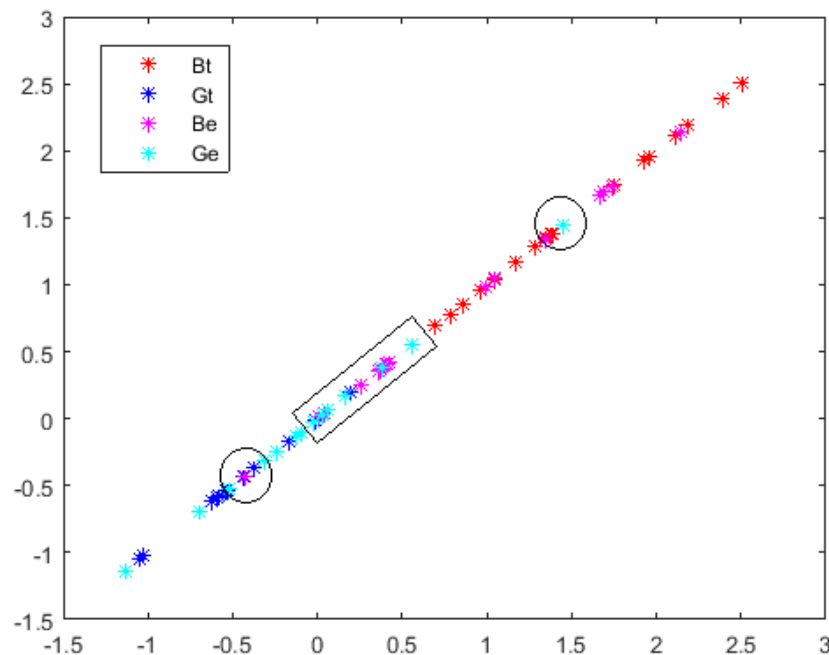


Figure 98. Projections of the training and evaluation signatures to the feature vector  $\mathbf{w}$ , results are visualized in 2D for better representation; “Bt”, “Gt”, “Be” and “Ge” stand for training set “Bad”, training set “Good”, evaluation set “Bad” and evaluation set “Good”, respectively



The overall percentage of correctly classified evaluation signatures amounts to 65%. The low percentage of the accuracy is mainly due to the small number of training data.

An improvement of the separability analysis is acquired by cross-validation (leave one out) (Bishop, 2006).

### LDA cross-validation (Leave one out) for evaluation of spectral signatures

In this method, due to the small number of training samples ( $N = 34 + 28$ ),  $N - 1$  training samples are used as training set. The training sample which is left out is considered as evaluation signature. In total,  $N$  training sets and feature vectors will be generated to evaluate the spectral signatures. The projections of training sets “Good” and “Bad” might have sometimes an overlap where is also the location of projection of the evaluation signature. Here, the middle of the overlap is considered as the decision boundary. Figure 99 illustrates an exemplary result of LDA cross-validation.

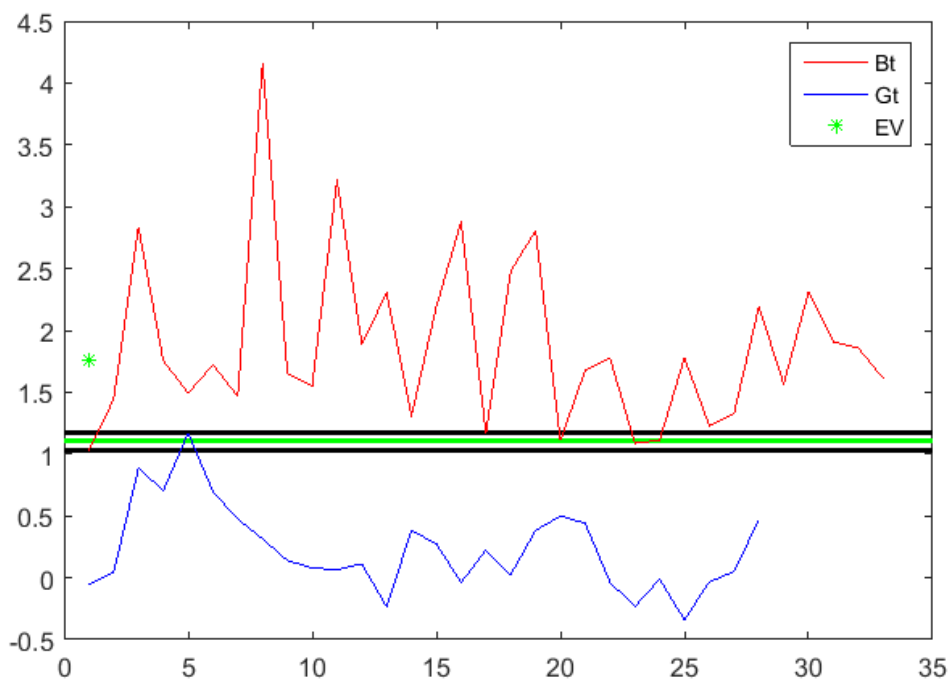


Figure 99. Projection of training sets “Bt” and “Gt” and an evaluation signature “EV” to the feature vector  $w_n$ . “EV” belongs to class “Bad” because the its projection value is between the decision boundary and the maximum projection value of the training set “Bt”

In Figure 99, the horizontal black lines show the boundaries of the overlap and the green line is the decision boundary. Result of LDA cross-validation is listed in

Table 11. The overall percentage of correctly classified evaluation signatures amounts to 79 %.

Class	Training data	Correctly classified evaluation signatures
Good	28	24
Bad	34	25

Table 11. Correctly classified signatures using LDA cross-validation

### 7.2.2. LDA result of mobile active spectrometer (Polytec)

Due to the heavy weight of the spectrometer head of Polytec, training data collection was carried out using a trolley (Figure 100).



Figure 100. An example of training data collection from a new asphalt section by Polytec spectrometer

Table 12 lists the results of LDA cross-validation of Polytec training data using first 240 and 250 bands containing wavelength ranges from 1253 nm to 2198 nm and from 1253 nm to 2236, respectively. It is not recommended to use the last 6 reflectivity values due to the data noise (see Figure 101).

Class	Number of training samples	Correctly classified evaluation signatures using	
		240 bands	250 bands
Good	28	22	22
Bad	20	12	14
Overall accuracy		71 %	75 %

Table 12. Correctly classified signatures using LDA cross-validation

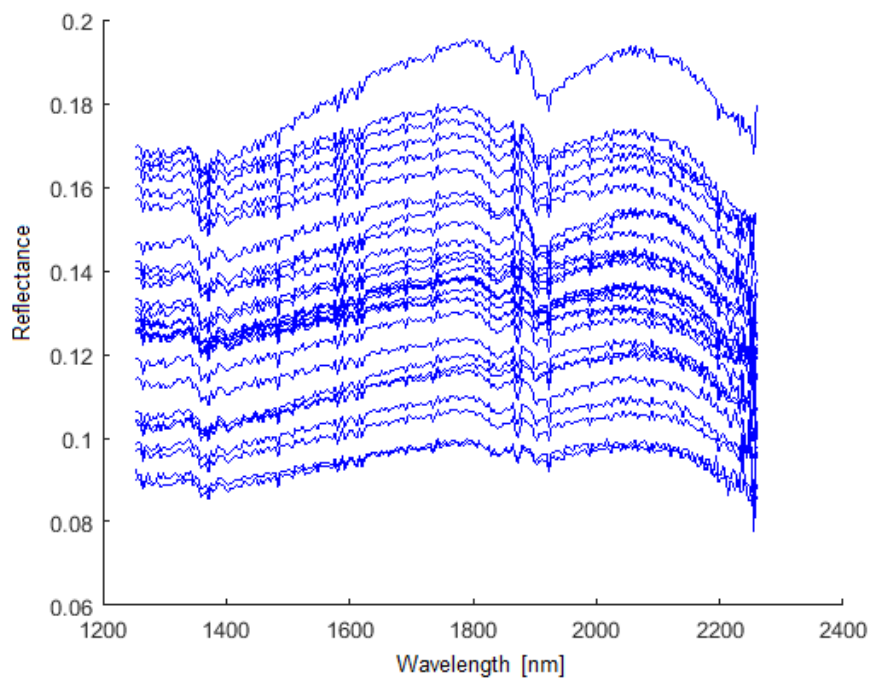


Figure 101. Spectral signatures of 28 training samples of Good class

The improvement of overall accuracy of the classification indicates the importance of the reflection values beyond 2200 nm.

### 7.3. Asphalt pavement classification using spectral signatures

For the classification of the pavement sections, ca. 14300 spectral signatures are recorded using mobile spectrometry with Polytec spectrometer. The spectrometry spots have an average distance interval of ca. 0.04 cm on the road due to the short exposure time of 0.033 sec. This short distance interval makes the classification result inhomogeneous. The majority filter is considered as a reasonable solution to cope with inhomogeneity. Initially the complete study area is divided into small sections of 4 m length. In each section, if more than 50% of the signatures belong to a specific class, e.g. class “Bad”, the whole evaluation results within the section will be considered as that specific class. Figure 102 shows the result of majority filtering. The green spots represent the evaluation result of mobile spectrometry using LDA. Blue and red lines show the points which are classified after majority filtering as class “Good” and “Bad”, respectively. The Black horizontal line is the decision class boundary. A subset of this result containing 100 LDA projections is shown in Figure 103.

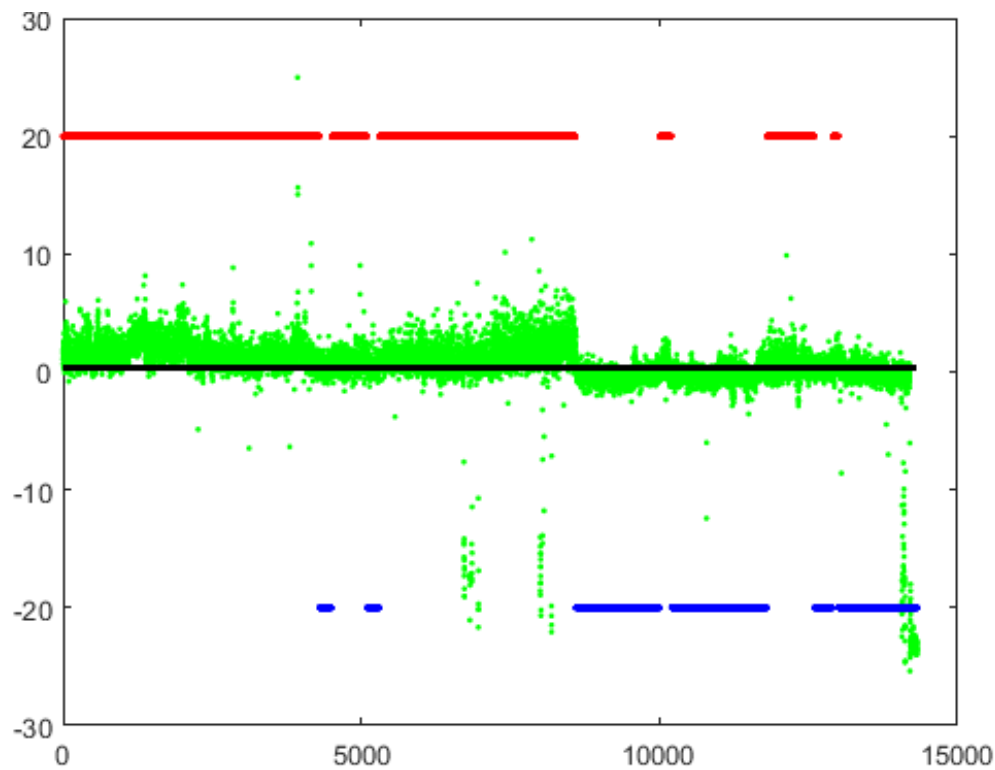


Figure 102. Result of majority filtering is illustrated by blue and red line, X- and Y-axis correspond to the number of evaluation signatures and the value of LDA projection, respectively, Note: The majority filter result is a binary quantity, i.e. the ordinates of the red and blue lines do not indicate the values of LDA projection.

## 7. Spectrometry data processing, results and discussion

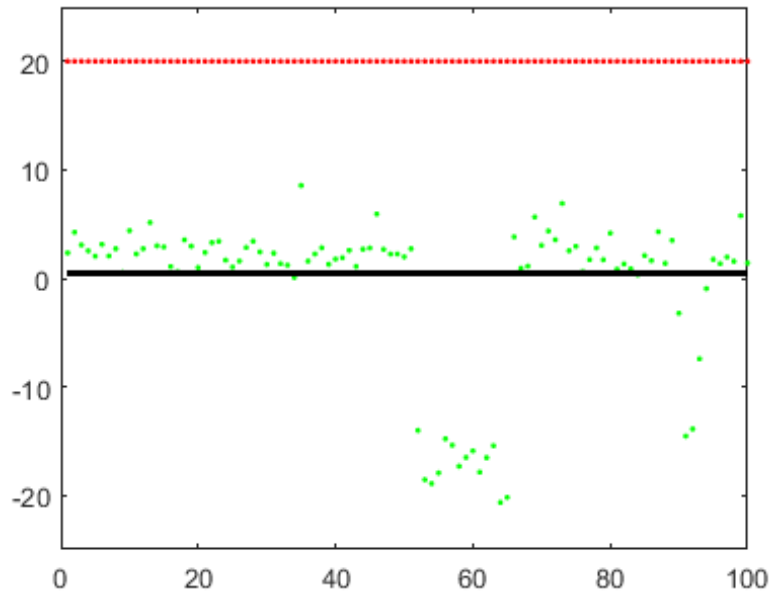


Figure 103. Result of majority filtering related to signature numbers: 7951 to 8050

As represented in Figure 103, the majority of the points are evaluated as “Bad” and the whole evaluation set is therefore classified into the class “Bad” by the majority filter. Figure 104 represents the class affiliation of the spectrometry spots after classification and majority filtering. The result of classification looks homogeneous. Validation of the classification result is performed by ground truthing. The total length of the measured path is  $T_{path} = 541.7$  m. In the figure, class “Bad” class “Good” are represented with red and blue lines, respectively.

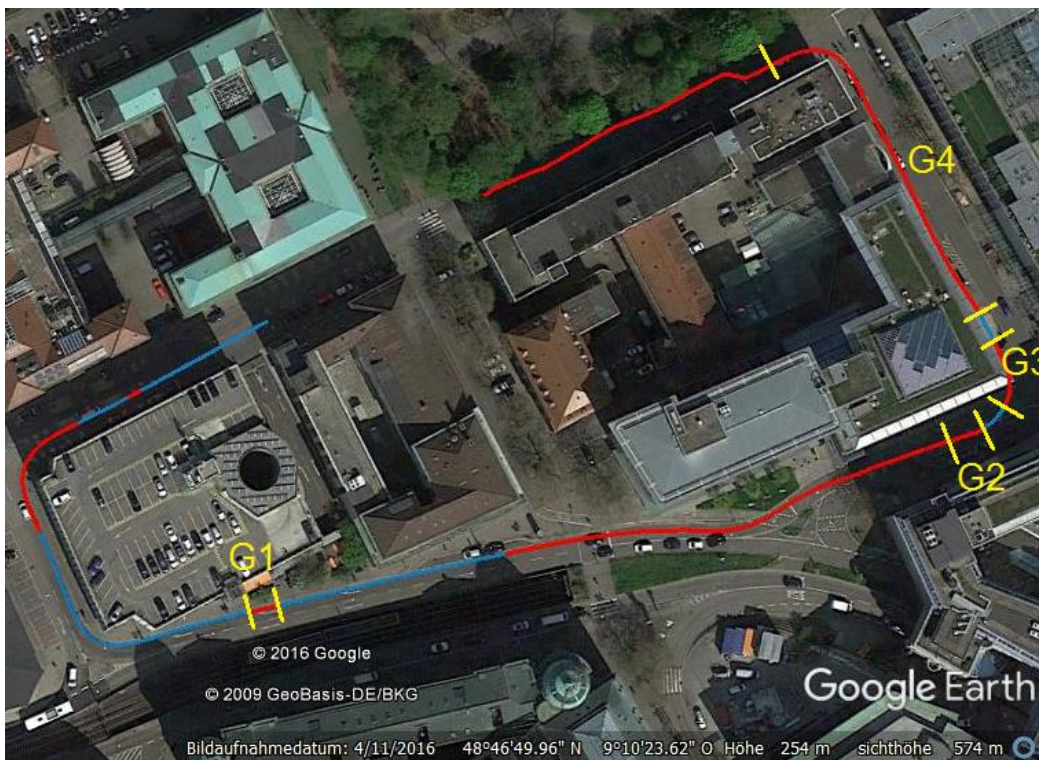


Figure 104. Result of classification of the road track based on LDA and majority filtering, G1, G2, G3 and G4 are four segments which are wrongly classified as class “Bad” and are represented between the yellow lines

### 7.3. Asphalt pavement classification using spectral signatures

The ground truth clarifies that the total segments of “Good” and “Bad” classes have the lengths of  $T_{path\_G} = 308.4$  m and  $T_{path\_B} = 233.3$  m., respectively. Four regions are wrongly classified as class “Bad” ( $FP_b$ ) and there is no FP of the class “Good”. Recall of class “Bad” amounts to 100% and the precision of class “Good” is 100 %. Table 13 lists the parameters of accuracy assessment of the classification results.

Class Good	[m]	Class Bad	[m]
$TP_g$	187	$TP_b$	233.3
$TN_g$	233.3	$TN_b$	187
$FP_g$	0	$FP_b$	121.4
$FN_g$	121.4	$FN_b$	0

Table 13. Parameters of the accuracy assessment of the classification results

It is clear that due to the existence of only two classes,  $TP_g = TN_b$ ,  $TP_b = TN_g$ ,  $FP_g = FN_b$  and  $FP_b = FN_g$ . Table 14 lists the result of accuracy assessment of the classification containing recall, precision and accuracy values of class “Good” ( $Recall_g$ ,  $Precision_g$ ) and class “Bad” ( $Recall_b$ ,  $Precision_b$ ).

<i>Recall<sub>g</sub></i>	61 %
<i>Precision<sub>g</sub></i>	100 %
<i>Recall<sub>b</sub></i>	100 %
<i>Precision<sub>b</sub></i>	66 %
Accuracy	77.6 %

Table 14. Result of accuracy assessment of the classification

The overall accuracy of 77.6 % shown in Table 14 is quite similar to the overall accuracy of correctly classified evaluation signatures shown in Table 12 (75 %). In both of these accuracy assessments, the first 250 spectral bands are employed for LDA.

## **8. Integration of road distresses and spectrometry classification outcomes**

In this chapter, the detected distresses are integrated into a road distress map together with the spectrometry classification outcomes. The visualization of distresses on the road map provides all required information for pavement condition evaluators. All detected road distresses are geo-referenced and visualized on a high-resolution ortho-mosaic of the mobile RGB-images. Figure 105 and Figure 106 illustrate two samples of road sections containing detected pavement distresses and the outcomes of spectrometry classification. The distresses shown in the legend are i) crack and ii) rut and depression. In addition, the outcome of spectrometry classification is depicted as material property “Good” and “Bad”. Whereas the background ortho-image covers the pedestrian area and some parts of the neighbouring buildings with a coarse resolution (20 cm grid increment), the ortho-mosaic of the mobile RGB-images has 1 mm ground resolution.

In this section, for crack detection, LF is utilized as the most promising method due to its highest mean completeness compared to HPF and MLBP methods (Miraliakbari, et al., 2016) and its better performance. As this method is applied on different resolution levels, it results in detection and visualization of cracks with various widths. Due to the insensitivity of the method against the shadow border, the boundaries between the shadow and sun areas are fortunately not detected as crack. However, the shadow of powerlines or the footprints of the frames of windows which reflect sunlight are partially classified into crack segments. Validation approves that boundaries between the intact pavement surface and removed road marks are cracking regions. In contrast to the gully removal approach which was successful (see Figure 77), it is not possible to avoid detection of manhole heads by the LF method. The solution is to remove these detected segments using the positions of the manhole heads which are provided by the cadastral administration.

1D polynomial fitting on the laser scanning profiles is used for rut detection. This method yields a substantial further advantage because it detects depressions additionally (round blue regions presented in Figure 105 and Figure 106).

The last two attributes of the legends in Figure 105 and Figure 106 are related to asphalt material classification provided by spectral signatures of Polytec spectrometer using the LDA method. The track illustrated with the cyan and pink colour shows class “Good” and class “Bad”, respectively.



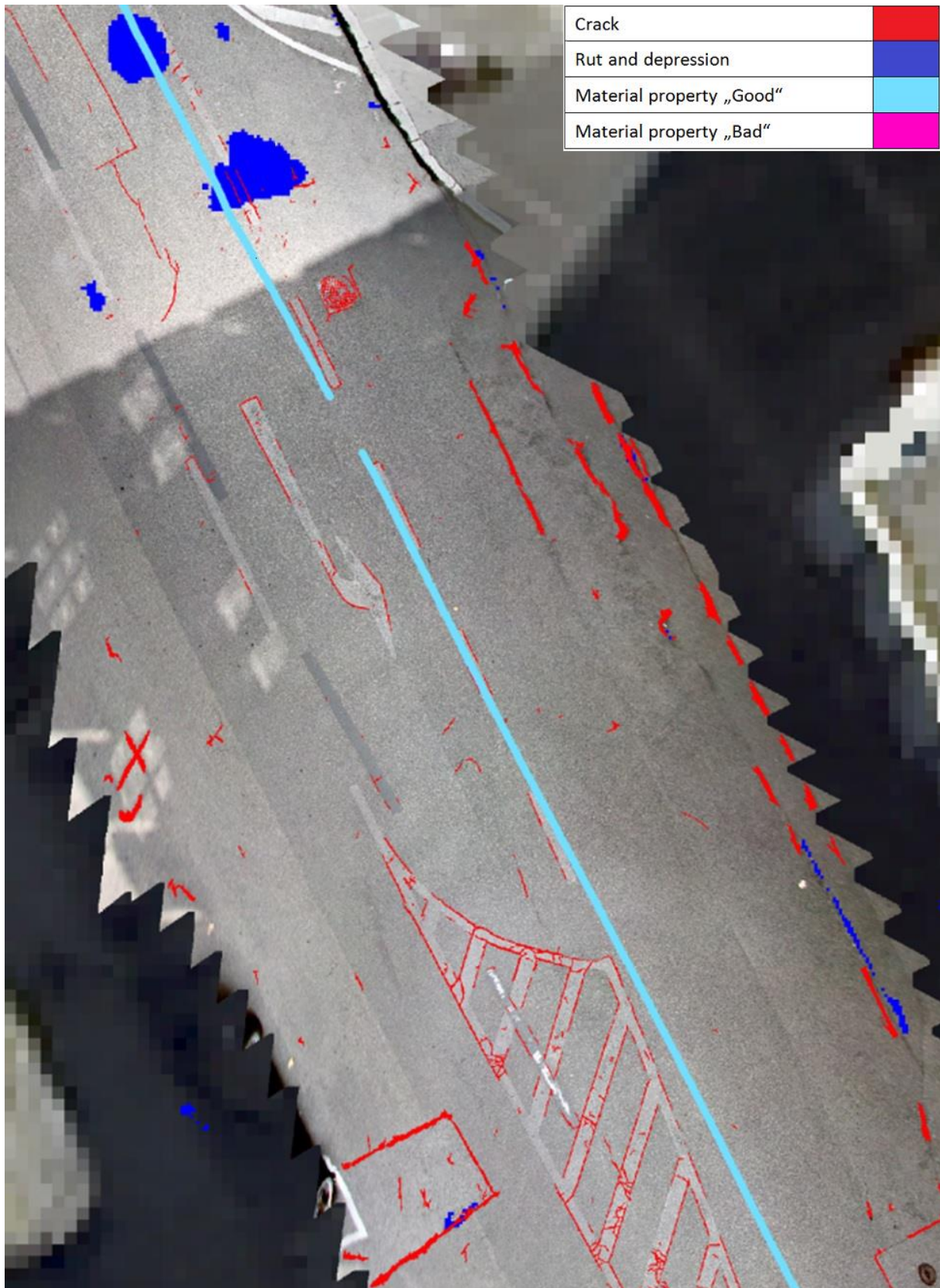


Figure 105. First sample of road section containing integrated pavement distresses and the result of asphalt quality classification

8. Integration of road distresses and spectrometry classification outcomes



Figure 106. Second sample of road section containing integrated pavement distresses and the result of asphalt quality classification



## 9. Conclusions and recommendations

### 9.1. Study conclusions

This dissertation is dedicated to the development of algorithms for the detection and localization of pavement distress and the investigation of pavement quality. For many years, pavement distresses have been captured either by on-site inspection or by digitizing mobile mapping data. In this study, the experimental investigations show that the developed methods are quite successful for automatic pavement distress detection and pavement quality classification.

In detail, this dissertation shows the following:

As a preparatory step for rut and pothole detection, the road surface is automatically separated from its neighbourhood in the laser scanning point cloud. The local point distribution with respect to the height is analysed and used to stop the region growing. The percentages of correctness and completeness of the extracted road surface amount to 94.9 % and 93.8 %, respectively.

Ruts as one of the severest road pavement distresses are successfully detected using iterative 1D polynomial fitting onto the scanline. The 1D polynomial fitting method is developed as alternative to the traditional rut depth measurement. For streets with the width of 6 m to 10 m, a 6<sup>th</sup> order polynomial is found to be most suitable. The iterative method detects so-called rut support segments in the scanline and does not feature concave or convex depressions or bulges between the rut support segments. However, a minor overshoot at the margins of scanlines may appear and is a consequence of the high polynomial order. Experimentally ruts are detected with an overall accuracy of 90.8 %. In addition to ruts also pavement depressions like shoving can be revealed. By cross-correlation with a 1D model of the rut, the centre of the rut is localized. In combination with the 1D polynomial the depth value of the rut can be identified. The normalized correlation coefficient is independent from the depth of a depression. Such sensitivity regarding small depressions is advantageous for the identification of “potential rut” of a shallow arc-shaped depression along the scanlines. The investigation into an alternative rut detection method using local curvature estimation shows a high sensitivity to the shape and width of a rut and is less successful.

The extraction of potholes is less demanding but offers a special challenge. As potholes are normally fixed quicker than other distresses and appear relatively rare in the road networks of a city, the few road segments which are affected by potholes are selected interactively. For further processing, two methods are explored, one utilizing bi-variate polynomial fitting, the other one geodesic morphological reconstruction to detect the pothole regions and separate them from the intact pavement surface. Experimental investigations show that similar to the 1D polynomial, a 5<sup>th</sup> order bi-variate polynomial is found to be most suitable because it fits to the boundary of the potholes as support region. However, as in the 1D case, it encounters problems with overshoot at the boundary of the road segments. The detection is very successful using geodesic morphological reconstruction. Fictitious water depth as an additional pavement distress value can be detected using the methods applied for pothole detection.

## 9. Conclusions and recommendations

For pavement crack detection, three methods using rotation invariant kernels are investigated: Line Filter (LF), High-pass Filter (HPF) and Modified Local Binary Pattern (MLBP). A conceptual aim of the procedure is to extract the cracks with a high degree of completeness. A comparative evaluation of the detection results using these three filters shows that LF method achieves the highest degree completeness of 81.2 %. MLBP is the most time consuming method due its complex computation of binary patterns. HPF method is computationally inexpensive due to the rotation invariance of the single utilized kernel. The LF outperforms the other two methods (Miraliakbari, et al., 2016). For example, a shadow boundary does not appear in the potential LF results (Miraliakbari, et al., 2016) but may be detected by other two methods. Fusion of detection results is applied to increase the percentage of completeness and reduce remaining artefacts of each detection approach. Experimental investigations show that, in most cases, the artefacts (wrongly detected cracks) disappear after fusion. Fusion of LF and HPF results increases the completeness to 86.7 %.

The main focus of patch detection is on homogeneity of the patched region and the gradient magnitude at the border between patch and intact pavement surface. As patches may not always have a dark border with the intact pavement surface, a method using the local standard deviation is more suitable for detecting the patches than an edge detection procedure. If the colour of material and the amount of aggregates of a patch and its neighbouring intact surface coincide and the border of the patch has no black tar, the patch detection is very challenging and has not been satisfactorily resolved.

By applying spectrometer recording of the pavement surface, another sensor is taken into account for road surface condition mapping. A promising approach is to restrict the mapping of material properties to two states: “Good” and “Bad”. With training samples of “Good” and “Bad” classes mainly quality and age of the asphalt is taken into account. Classification of asphalt pavement quality is performed with the help of linear discriminant analysis. Road pavement sections of ca. 4 m length are classified into “Good” and “Bad” classes with the overall accuracy of 77.6 %. The spectral classification of pavement sections contributes to road condition mapping as it gives hints on aging of the pavement. As this classification offers a new access and strategy to road condition mapping, it can help FGSV and ASTM standards to define new parameters for road condition assessment based on pavement quality.

Integration of the detected distresses into a road distress map is carried out together with the spectrometry classification outcomes. The visualization of distresses on the road map provides all required information for pavement condition evaluators and mostly discharges them from investigations of the primary imagery and laser scanning data.

### 9.2. Recommendations

Following further developments and studies are recommended to increase performance of automatic road condition mapping.

For the test drives in this dissertation, a mobile mapping system has been specifically developed by integrating an RGB camera, a laser scanner, a GNSS-aided inertial navigation system and a spectrometer. This semi-professional solution has advantages like the integration of a spectrometer into the mapping platform, but has also limitations. An extension to the existing work follows from the possibility of stereo-camera setups (Cavegn, et al., 2015) with three or more cameras observing the road surface in front of or behind the mobile mapping van. The generation of dense point clouds from

those images makes the use of a laser scanner questionable. The chosen concept of this study, i.e. the detection of rut and potholes based on laser point clouds and the detection of cracks and patches from imagery does not become obsolete as the laser point cloud can be replaced by the point cloud derived from RGB images. The expected more homogeneous distribution of a dense point cloud generated by RGB images can be exploited by extending the laser scanline processing e.g. of rut detection from 1D analysis to a 2D concept. Another sensor change is possible, in which the spectrometer is replaced by a hyper-spectral camera. Even if existing hyper-spectral cameras currently do not meet the requirements of a mobile mapping environment, the areal analysis of a hyper-spectral image of the road surface would extend the informative value of the classification of the hitherto recorded spectrometer profile. Whether it is also possible to expand the asphalt characterization into more than “Good” and “Bad” classes is another open issue for further studies.

In this dissertation, the automatic pavement distress detection was concentrated on ruts, potholes, cracks and patches, however, some other distresses may appear on the pavement surfaces. Distresses like bleeding, bump, sag, corrugation, etc. which may appear on roads not as often as ruts, cracks and patches are further of interest in road condition mapping. Whether or not and to which extend these distresses can be extracted from laser scanning data and RGB images remain a topic of further research.

So far no investigations are carried out to evaluate the road distress map and derive road condition parameters automatically. It will be very valuable to develop an automatic road pavement evaluation system using detected pavement distresses as input and FGSV and/ or ASTM evaluation standards as reference.



## References and bibliography

Agisoft PhotoScan, 2016. *Agisoft PhotoScan*. [Online]

Available at: <http://www.agisoft.com/>

[Accessed 17 05 2016].

Ai, X., Gao, Y., Rarity, J. G. & Dahnoun, N., 2013. Obstacle detection using U-disparity on quadratic road surfaces. *Intelligent Transportation Systems-(ITSC) 16th International IEEE Conference on*, pp. 1352-1357.

Applanix, 2015. *Applanix*. [Online]

Available at: [http://www.applanix.com/pdf/specs/POSLV\\_Specifications\\_dec\\_2015.pdf](http://www.applanix.com/pdf/specs/POSLV_Specifications_dec_2015.pdf)

[Accessed 01 01 2017].

Arefi, H., 2009. *From LIDAR Point Clouds to 3D Building Models*. Munich: Universität der Bundeswehr München, Institut für Angewandte Informatik, PhD Dissertation.

Asdi, 2017. *Asdi*. [Online]

Available at: <https://www.asdi.com/products-and-services/fieldspec-spectroradiometers/fieldspec-4-standard-res>

[Accessed 06 06 2017].

Asphalt Institute, 1989. *The Asphalt Handbook*. No. 4 of Manual Series ed. College Park: The Asphalt Institute (1989).

ASTM-D6433, 2008. *Standard Practice for Roads and Parking Lots Pavement Condition Index Surveys*, ASTM International.

Barnea, D. I. & Silverman, H. F., 1972. A Class of Algorithms for Fast Digital Image Registration. *IEEE Transactions on Computers*, Vol. C-21, No. 2, pp. 179-186.

Bishop, C., 2006. *Pattern Recognition and Machine Learning*. New York: Springer Science+Business Media.

Blades, C. & Kearney, E., 2004. *Cornell*. [Online]

Available at: <https://cornell.app.box.com/v/clrp-ws-app>

[Accessed 06 06 2017].

Casas, A., Pinto, V. & Rivero, L., 2000. Fundamentals of ground penetration RADAR in environmental and engineering applications. *Annals of Geophysics*.

Cavegn, S., Haala, N., Nebiker, S., Rothermel, M. & Zwölfer, T., 2015. Evaluation of Matching Strategies for Image-Based Mobile Mapping. *ISPRS Annals of the Photogrammetry, Remote Sensing and Spatial Information Sciences*, pp. 361- 368.

Chan, C. K., Gao, Y., Zhang, Z. & Dahnoun, N., 2014. Implementation and evaluation of a pothole detection system on TI C6678 digital signal processor. *Proceedings of the 6th European Embedded Design in Education and Research*, pp. 297-301.

Chang, C. & Lin, C., 2016. *LIBSVM, A Library for Support Vector Machines*. [Online]

Available at: <http://www.csie.ntu.edu.tw/~cjlin/libsvm>

Cloutis, A. E., 1989. Spectral Reflectance Properties of Hydrocarbons: Remote - Sensing Implications. *Science*, pp. 165-168.

Curran, P., 1994. *Imaging spectrometry- Its present and future role in environmental research, Imaging spectrometry- a tool for environmental observation*. Brussels and Luxemburg: Springer Netherlands.

Douglas, D. & Peucker, T., 1973. Algorithms for the reduction of the number of points required to represent a digitized line or its caricature. *The International Journal for Geographic Information and Geovisualization*, p. 112–122.

dpreview, 2016. *dpreview*. [Online]

Available at: <https://www.dpreview.com/reviews/canoneos5dmarkii/2>  
[Accessed 05 09 2016].

El-Halawany, S., Moussa, A., Lichti, D. D. & El-Sheimy, N., 2011. Detection of Road Curb from Mobile Terrestrial Laser Scanner Point Cloud. *The International Archives of Photogrammetry, Remote Sensing and Spatial Information Sciences*, pp. 109-114.

Engels, J., Hahn, M., Chisense, C. & Gülch, E., 2015. MiniMax Discriminant Analysis in Hyperspectral Imagery and the Retrieval of Spectral Features. *Unpublished*.

ERF, 2015. ERF, European Union Road Federation, Towards Safer Work Zones.

Eriksson, J., Girod, L., Hull, B., Newton, R., Madden, S. & Balakrishnan, H., 2008. The pothole patrol: using a mobile sensor network for road surface monitoring. *Proc. of the 6th Int. Conf. on Mobile Systems, Applications, And Services (MobiSys)*, pp. 29–39.

Faro, 2013. *Reproproducts*. [Online]

Available at: <https://reproproducts.com/pdfs/brochures/faro/x330.pdf>  
[Accessed 07 06 2017].

Faro, 2016. *Faro*. [Online]

Available at: <http://www.faro.com/products/3d-surveying/laser-scanner-faro-focus-3d/features>  
[Accessed 07 06 2017].

FGSV, 2001. *Arbeitspapiere zur Zustandserfassung und -bewertung der Fahrbahnoberflächen von Straßen Nr. 9. Forschungsgesellschaft für Straßen- und Verkehrswesen*. Köln: fgsv-verlag.

Fisher, R., 1936. The use of Multiple Measurement in Taxonomic Problems. *Annals of Eugenics*, pp. 179-188.

Fitzgibbon, A., Pilu, M. & Fischer, R., 1999. Direct least-squares fitting of ellipses. *IEEE Trans. Pattern Anal. Mach. Intel.* 22 (5) , pp. 476-480.

FLIR, 2016. *FLIR, FLIR thermal imaging cameras help determine road conditions in Finland*. [Online]

Available at:

[http://www.flir.com/uploadedFiles/CS\\_EMEA/Application\\_Stories/Media/Downloads/Roadscanner\\_EN.pdf](http://www.flir.com/uploadedFiles/CS_EMEA/Application_Stories/Media/Downloads/Roadscanner_EN.pdf)

[Accessed 26 08 2016].

Gallo, O., Manduchi, R. & Rafii, A., 2008. Robust curb and ramp detection for safe parking using the canesta ToF camera. *Computer Vision and Pattern Recognition Workshops, CVPRW'08. Computer Society Conference. IEEE.*

Gavilán, M., Balcones, D., Marcos, O., Llorca, D.F., Sotelo, M.A., Parra, I., Ocaña, M., Aliseda, P., Yarza, P. & Amírola, A., 2011. Adaptive road crack detection system by pavement classification. *Sensors*, pp. 9628-9657.

Golub, G. H. & Von Matt, U., 1991. Quadratically constrained least squares and quadratic problems. *Numerische Mathematik*, 59(1), pp. 561-580.

Hadjidemetriou, G. M., Christodoulou, S. E. & Vela, P. A., 2016. Automated detection of pavement patches utilizing support vector machine classification. *18th Mediterranean Electrotechnical Conference (MELECON)*, 18-20 April, pp. 1-5.

Heiden, U., Segl, K., Roessner, S. & Kaufmann, H., 2007. Determination of Robust Spectral Features for Identification of Urban Surface Materials. *Remote Sensing of Environment* 111(4), pp. 537-552.

Herold, M., Gardner, M., Noronha, V. & Roberts, D., 2003. Spectrometry and hyper-spectral remote sensing of urban road infrastructure. *Online Journal of Space Communications*, 3.

Herold, M. & Roberts, D., 2005b. Spectral characteristics of asphalt road aging and deterioration: implications for remote-sensing applications. *Applied Optics*, 44(20), pp. 4327-4334.

Herold, M. & Roberts, D. A., 2005a. Mapping asphalt road conditions with hyperspectral remote sensing. *In 5th International Symposium Remote Sensing of Urban Areas (URS 2005).*

Herold, M., Roberts, D. A., Gardner, M. E. & Dennison, P. E., 2004. Spectrometry for urban area remote sensing—Development and analysis of a spectral library from 350 to 2400 nm. *Remote Sensing of Environment*, 91(3), pp. 304-319.

Huang, Y., Hempel, P. & Copenhaver, T., 2009. *A Rut Measurement System Based on Continuous Transverse Profiles From a 3-D System*, Texas : Research and Development Project Report, Materials and Pavements Section Construction Division Texas Department of Transportation.

Hu, Y. & Zhao, C., 2010. A Local Binary Pattern Based Methods for Pavement Crack Detection. *Journal of Pattern Recognition Research* 5.1, pp. 140-147.

IFI, 2014. *IFI Consult GmbH*. [Online]  
Available at: <http://ific.dyndns.org/pdf/erhaltung.pdf>  
[Accessed 25 09 2014].

Joubert, D., Tyatyantsi, A., Mphahlehle, J. & Manchidi, V., 2011. Pothole tagging system. *In Proceedings of the 4th Robotics and Mechatronics Conference of South Africa.*

Kass, M., Witkin, A. & Terzopoulos, D., 1988. Snakes: Active contour models. *Int. J. Computer Vision*, pp. 321-331.

Kertész, I., Lovas, T. & Barsi, A., 2008. Photogrammetric Pavement Detection System. *The International Archives of the Photogrammetry, Remote Sensing and Spatial Information Sciences*, p. 897–902.



- Kim, T. & Ryu, S. K., 2014. Review and analysis of pothole detection methods. *Journal of Emerging Trends in Computing and Information Sciences*, pp. 603-608.
- Koch, C. & Brilakis, I., 2011. Pothole detection in asphalt pavement images. *Advanced Engineering Informatics*, pp. 507-515.
- Lafferty, J., McCallum, A. & Pereira, F., 2001. Conditional random fields: Probabilistic models for segmenting and labeling sequence data. In *Proceedings of the eighteenth international conference on machine learning, ICML, Vol. 1*, pp. 282-289.
- Lambot, S., Slob, E. C., van den Bosch, I., Stockbroeckx, B. & Vanclooster, M., 2004. Modeling of ground-penetrating radar for accurate characterization of subsurface electric properties. *IEEE Transactions on Geoscience and Remote Sensing 42(11)*, pp. 2555-2568.
- Laurent, J. & Hébert, J., 2002. High Performance 3D Sensors for the characterization of Road Surface Defects. *MVA2002 IAPR Workshop on Machine Vision Applications, Nara- ken New Public Hall, Nara, Japan*, pp. 388-391.
- Laurent, J., Hébert, J. F., Lefebvre, D. & Savard, Y., 2012. Using 3D laser profiling sensors for the automated measurement of road surface conditions. In *7th RILEM International Conference on Cracking in Pavements, Springer Netherlands*, pp. 157-167.
- Laurent, J., Hébert, J., Lefebvre, D. & Savard, Y., 2013. 3D laser road profiling for the automated measurement of road surface conditions and geometry. *semanticscholar*.
- Laurent, J., Talbot, M. & Doucet, M., 1997. Road surface inspection using laser scanners adapted for the high precision 3D measurements of large flat surfaces.. *Proceedings. International Conference on Recent Advances in 3-D Digital Imaging and Modeling*, pp. 303-310.
- Lay, M., 1992. *Ways of the world a history of the world's roads and of the vehicles that used them*. New Brunswick: N.J Rutgers University Press 1992.
- Le Brisa, A., Chehatab, N., Briottet, X. & Papparoditisa, N., 2016. Spectral Band Selection for Urban Material Classification Using Hyperspectral Libraries. *ISPRS Annals of Photogrammetry, Remote Sensing and Spatial Information Sciences*, pp. 33-40.
- Lee, B., Kim, J., Kim, Y. & Yi, S., 2007. A technique based on image processing for measuring cracks in the surface of concrete structures. *The 19th International Conference on Structural Mechanics in Reactor Technology (SMiRT-19)*.
- Leese, J., Novak, C. S. & Clark, B. B., 1971. An Automated Technique for Obtaining Cloud Motion from Geosynchronous Satellite Data Using Cross Correlation. *Journal of Applied Meteorology, Vol. 10, No.1*, pp. 118-132.
- LEHMANN and PARTNER GmbH, 2016. *vectragermany*. [Online] Available at: <http://vectragermany.com/home?L=6> [Accessed 16 08 2016].
- Li, S., Yuan, C., Liu, D. & Cai, H., 2016. Integrated Processing of Image and GPR Data for Automated Pothole Detection. *Journal of Computing in Civil Engineering, 30(6)*.
- Maas, H.-G., 2012. Digitale Nahbereichsphotogrammetrie im bautechnischen Versuchswesen. *Bautechnik Nr. 89 (11)*, pp. 786-793.

- Maerschalk, G. & Oertelt, S., 2014. *Anforderungen an die Erhaltung von Radwegen*. München, Dießen a. Ammersee: BASt-Bericht S 84.
- Mahmoudzadeh, M. R., Got, J. B., Lambot, S. & Grégoire, C., 2013. Road inspection using full-wave inversion of far-field ground-penetrating radar data. *In Advanced Ground Penetrating Radar (IWAGPR), IEEE*, pp. 1-6.
- Mancini, A., Malinverni, E., Frontoni, E. & Zingaretti, P., 2013. Road Pavement Crack Automatic Detection by MMS Images. *21st Mediterranean Conference on Control & Automation (MED)*, pp. 1589-1596.
- Marques, A., 2012. *Automatic road pavement crack detection using SVM, Dissertation to obtain a Master Degree in Electrical and Computer Engineering*. Lisbon: Instituto Superior Técnico, Universidade Técnica de Lisboa.
- Mednis, A., Strazdins, G., Zviedris, R., Kanonirs, G. & Selavo, L., 2001. Real time pothole detection using Android smartphones with accelerometers. *Proceedings of the International Conference on Distributed Computing in Sensor Systems and Workshops*, pp. 1-6.
- Miraliakbari, A. & Hahn, M., 2014. Road Crack Detection in Images Recorded by a Mobile Mapping System. *In: Proc. of Applied Geoinformatics for Society and Environment 2014*.
- Miraliakbari, A., Hahn, M. & Maas, H., 2014. Development of a Multi-Sensor System for Road Condition Mapping. *The International Archives of Photogrammetry, Remote Sensing and Spatial Information Sciences*.
- Miraliakbari, A., Hahn, M. & Sok, S., 2015. Automatic Extraction of Road Surface and Curbstone Edges from Mobile Laser Scanning Data. *International Archives of the Photogrammetry, Remote Sensing and Spatial Information Sciences*.
- Miraliakbari, A., Sok, S., Ouma, Y. O. & Hahn, M., 2016. Comparative evaluation of pavement crack detection using kernel-based techniques in asphalt road surfaces. *Int. Arch. Photogramm. Remote Sens. Spatial Inf. Sci.*, pp. 689-694.
- Moazzam, I., Kamal, K., Mathavan, S., Usman, S. & Rahman, M., 2013. Metrology and visualization of potholes using the Microsoft Kinect Sensor. *Proceedings of the 16th International IEEE Annual Conference on Intelligent Transportation Systems (ITSC)*, pp. 1284-1291.
- Negussie, K., 2015. *Pothole Detection Using Dense Laser Range Data and Colour Images*. Stuttgart: Hochschule für Technik Stuttgart, Master Thesis.
- Ojala, T., Pietikainen, M. & Maenpää, T., 2002. Multiresolution gray-scale and rotation invariant texture classification with local binary patterns. *IEEE Transactions on Pattern Analysis and Machine Intelligence*, 24(7), pp. 971-987.
- Oliveira, H. & Correia, P. L., 2014. CrackIT – An image processing toolbox for crack detection and characterization. *Proc IEEE International Conf. on Image Processing (ICIP)*, pp. 798-802.
- Oliveira, H. J. M., 2013. *Crack Detection and Characterization in Flexible Road Pavements using Digital Image Processing*. Lisbon: UNIVERSIDADE TÉCNICA DE LISBOA, INSTITUTO SUPERIOR TÉCNICO, PhD Dissertation.

- Orbitgt, 2016. *Orbitgt*. [Online]  
Available at: <https://orbitgt.com/mobile-mapping/>  
[Accessed 17 06 2016].
- Orr, D. P., 2006. *Pavement Maintenance*. New York: Cornell local Roads Program New York LTAP Center.
- Otsu, N., 1979. A threshold selection method from gray-level histograms. *IEEE Transactions on Systems, Man, and Cybernetics*, pp. 62-66.
- Paris, S., Kornprobst, P., Tumblin, J. & Durand, F., 2009. *Bilateral Filtering: Theory and Applications*. s.l.:Essemce of knowledge.
- Pavemetrics, 2017. *Pavemetrics*. [Online]  
Available at: <http://www.pavemetrics.com/>  
[Accessed 08 06 2017].
- Polytec, 2011a. *Polytec Spectrometer System, user manual, PSS- XXXI, 41368-Man-PSSxxxI-0311-03en*. Waldbronn: Polytec.
- Polytec, 2011b. *Conveyor Belt Sensor Head, PSS-H-A03*. Waldbronn: Polytec.
- Polytec, 2013a. *PSS Spectrometers*, Waldbronn: Polytec GmbH.
- Polytec, 2013b. *polytec, Process control using NIR Spectrometry*. [Online]  
Available at:  
[http://www.polytec.com/fileadmin/user\\_uploads/Products/Spektrometer/Analytik/Documents/Process%20Control%20Using%20NIR%20Spectroscopy.pdf](http://www.polytec.com/fileadmin/user_uploads/Products/Spektrometer/Analytik/Documents/Process%20Control%20Using%20NIR%20Spectroscopy.pdf)  
[Accessed 11 10 2013].
- Polytec, 2013c. *Distance Sensor Head*. [Online]  
Available at: <http://www.polytec.com/us/products/spectrometers/nir-spectrometer-systems/sensor-heads/distance-sensor-head/>  
[Accessed 08 11 2013].
- Radopoulou, S. C. & Brilakis, I., 2015. Patch detection for pavement assessment. *Automation in Construction*, 53, pp. 95-104.
- Ramer, U., 1972. An iterative procedure for the polygonal approximation of plane curves. *Computer Graphics and Image Processing 1 (3)*, pp. 244-256.
- Rial, F.I., Pereira, M., Lorenzo, H., Arias, P. & Novo, A., 2006. Use of ground penetrating radar and global positioning systems for road inspection. *International Archives of the Photogrammetry, Remote Sensing and Spatial Information Sciences*.
- Robl, T. L., Milburn, D., Thomas, G., Groppo, J., O'Hara, K. & Haak, A., 1991. The SHRP materials reference library aggregates: chemical, mineralogical, and sorption analyses. *Strategic Highway Research Program (SHRP) Publ. SHRP-A/UIR-91-509*.
- Rode, S., 2007. *A Pothole Detection System*. Bombay: Department of Computer Science and Engineering, Indian Institute of Technology, Master Thesis.
- Serra, J., 1982. *Image Analysis and Mathematical Morphology*. Academic Press, London.

Serra, J., 1988. *Image Analysis and Mathematical Morphology. Volume 2: Theoretical Advances*, Academic Press, London.

Shahin, M. Y., 2005. *Pavement Management for Airports Roads and Parking Lots*. New York: Springer.

Siegemund, J., Pfeiffer, D., Franke, U. & Förstner, W., 2010. Curb reconstruction using Conditional Random Fields. *IEEE Intelligent Vehicles Symposium (IV)*, pp. 203-210.

Silva, G.D.D., Zoysa, K.D., Perera, R.S., Laxaman, N.M., Keppitiyagama, C. & Thilakarathna, K.M., 2008. Automated Pothole Detection Using Wireless Sensor Motes. *International IT Conference (IITC 08)*.

Spectral Evolution PSR+ 3500, 2012. *Spectral Evolution*. [Online]  
Available at: [http://www.spectralevolution.com/spectroradiometer\\_PSR\\_plus.html](http://www.spectralevolution.com/spectroradiometer_PSR_plus.html)  
[Accessed 13 05 2016].

Spectral Evolution, 2012. *Spectral Evolution*. [Online]  
Available at: [http://www.spectralevolution.com/portable\\_spectroradiometer.html](http://www.spectralevolution.com/portable_spectroradiometer.html)  
[Accessed 09 05 2016].

Subirats, P., Dumoulin, J., Legeay, V. & Barba, D., 2006. Automation of pavement surface crack detection using the continuous wavelet transform. *Image Processing, 2006 IEEE International Conference*, pp. 3037-3040.

Subirats, P., Fabre, O., Dumoulin, J., Legeay, V. & Barba, D., 2004. A combined wavelet-based image processing method for emergent crack detection on pavement surface images. *In Signal Processing Conference, 2004 12th European, IEEE*, pp. 257-260.

Sun, C. & Vallotton, P., 2006. Fast linear feature detection using multiple directional non-maximum. *In Proceedings of the 18th IEEE International Conference on Pattern Recognition (ICPR06)*.

The Mara Nord Project, 2012. The Use of GPR in Road Rehabilitation Projects, Mara Nord Project..

Timbercon, 2013. *Timbercon*. [Online]  
Available at: <http://www.timbercon.com/SMA-Connector.html>  
[Accessed 07 11 2013].

TÜV Rheinland Schniering GMBH, 2017. *TÜV Rheinland Schniering*. [Online]  
Available at: <http://www.schniering.com/>  
[Accessed 2017 06 07].

Vincent, 1993. Morphological grayscale reconstruction in image analysis: applications and efficient algorithms. *IEEE transactions on image processing 2.2*, pp. 176-201.

Vosselman, G. & Liang, Z., 2009. Detection of curbstones in airborne laser scanning data. *The International Archives of the Photogrammetry, Remote Sensing and Spatial Information Sciences 38*, pp. 111-116.

Webopedia, 2013. *webopedia*. [Online]  
Available at: [http://www.webopedia.com/TERM/F/fiber\\_optics.html](http://www.webopedia.com/TERM/F/fiber_optics.html)  
[Accessed 11 10 2013].

Wikipedia, 2017. *Curb*. [Online]

Available at: [http://en.wikipedia.org/wiki/Curb#cite\\_note-6](http://en.wikipedia.org/wiki/Curb#cite_note-6)

[Accessed 2017 06 07].

Xu, C. & Prince, J. L., 1997. Gradient Vector Flow: A New External Force for Snakes. *IEEE Computer Vision and Pattern Recognition (CVPR 97)*, pp. 66-71.

Yamaguchi, T. & Hashimoto, S., 2006. Automated crack detection for concrete surface image using percolation model and edge information. *In Proceedings of the 32nd Annual Conference of the IEEE Industrial Electronics Society (IECON2006)*, pp. 3355-3360.

Yu, S., 2005. *Digitizing and 3D Modeling of road surface using an integrated multisensory approach*. Tennessee: University of Tennessee, Report of the project in lieu of Masters Thesis.

Yu, S-J., Sukumar, S.R., Koschan, A.F., Page, D.L. & Abidi, M.A., 2007. 3D reconstruction of road surfaces using an integrated multi-sensory approach. *Optics and Lasers in Engineering 45*, pp. 808-818.

Yu, X. & Salari, E., 2011. Pavement pothole detection and severity measurement using laser imaging. *Electro/Information Technology (EIT), 2011 IEEE International Conference*, pp. 1-5.

Zhang, Z., Ai, X., Chan, C. & Dahnoun, N., 2014. An efficient algorithm for pothole detection using stereo vision. *IEEE International Conference on Acoustic, Speech and Signal Processing (ICASSP)*, pp. 564-568.

Zhu, Z. & Brilakis, I., 2010. Machine vision based concrete surface quality assessment. *Journal of Construction Engineering and Management 136 (2)* , p. 210–218.